EXPLORING TIME-DEPENDENT APPROACHES TOWARDS CALCULATION OF DYNAMICS AND SPECTROSCOPIC SIGNALS: A MIXED QUANTUM/ SEMICLASSICAL WAVE PACKET METHOD AND THE THEORY OF TRANSIENT ABSORPTION AND FEMTOSECOND STIMULATED RAMAN SCATTERING

by

PHILIP A. KOVAC

A DISSERTATION

Presented to the Department of Chemistry and Biochemistry
and the Graduate School of the University of Oregon
in partial fulfillment of the requirements
for the degree of
Doctor of Philosophy

September 2017

DISSERTATION APPROVAL PAGE

Student: Philip A. Kovac

Title: Exploring Time-Dependent Approaches Towards Calculation of Dynamics and Spectroscopic Signals: A Mixed Quantum/Semiclassical Wave Packet Method and the Theory of Transient Absorption and Femtosecond Stimulated Raman Scattering

This dissertation has been accepted and approved in partial fulfillment of the requirements for the Doctor of Philosophy degree in the Department of Chemistry and Biochemistry by:

George Nazin	Chair
Jeffrey A. Cina	Advisor
Michael Kellman	Core Member
Andy Marcus	Core Member
Hailin Wang	Institutional Representative

and

Sara D. Hodges	Interim Vice Provost and Dean of the Graduate School

Original approval signatures are on file with the University of Oregon Graduate School.

Degree awarded September 2017

DISSERTATION ABSTRACT

Philip A. Kovac

Doctor of Philosophy

Department of Chemistry and Biochemistry

September 2017

Title: Exploring Time-Dependent Approaches Towards Calculation of Dynamics and Spectroscopic Signals: A Mixed Quantum/Semiclassical Wave Packet Method and the Theory of Transient Absorption and Femtosecond Stimulated Raman Scattering

We present a time-dependent mixed quantum/semiclassical approach to calculating linear absorption spectra. Applying Variational Fixed Vibrational Basis/Gaussian Bath theory (FVB/GB) to the treatment of small molecules isolated in an extended cryogenic medium, an assumed time-scale separation between the few rapid, largely intramolecular modes of the guest and the several slower extended modes of the medium is utilized to partition a system from the surrounding bath. The system dynamics are handled with basis set methods, while the bath degrees of freedom are subject to a semiclasscial thawed Gaussian ansatz. The linear absorption spectrum for a realistic model system is calculated using FVB/GB results and then compared with a numerically exact calculation. Also contained in this dissertation are previously published theoretical works on Transient Absorption and Femtosecond Stimulated Raman Spectroscopy. Both encompass a rebuilding of the theory and elucidate the information content of the respective spectroscopic signals.

This dissertation includes previously published and unpublished co-authored material.

CURRICULUM VITAE

NAME OF AUTHOR: Philip A. Kovac

GRADUATE AND UNDERGRADUATE SCHOOLS ATTENDED:

University of Oregon, Eugene, OR
Ball State University, Muncie, IN
Flagler College, St. Augustine, FL

DEGREES AWARDED:

Doctor of Philosophy, Theoretical Physical Chemistry, 2017, University of Oregon
Bachelor of Science, Chemistry and Psychology, 2009, Ball State University

AREAS OF SPECIAL INTEREST:

Quantum Dynamics
Femtosecond Spectroscopy
Chaos Theory

PROFESSIONAL EXPERIENCE:

Graduate Research Fellow, University of Oregon, 2010-2017

Graduate Teaching Fellow, University of Oregon, 2009-2017

PUBLICATIONS:

P. A. Kovac and J. A. Cina, Testing a wave packet dynamical approach: An application of a mixed quantum/semiclassial method in the calculation of linear absorption, *manuscript in preparation.*

C. C. Jumper, P. C. Arpin, D. B. Turner, S. D. McClure, S. Rafiq, J. C. Dean, J. A. Cina, P. A. Kovac, T. Mirkovic and G. D. Scholes, Broad-Band PumpProbe Spectroscopy Quantifies Ultrafast Solvation Dynamics of Proteins and Molecules, Journal of Physical Chemistry Letters **7**, 4722 (2016).

J. A. Cina, P. A. Kovac, C. C. Jumper, J. C. Dean and G. D. Scholes, Ultrafast transient absorption revisited: Phase-flips, spectral fingers, and other dynamical features, Journal Chemical Physics **144**, 175102 (2016).

Cina J. A. and Kovac P. A. How Fissors Works: Observing Vibrationally Adiabatic Conformational Change through Femtosecond Stimulated Raman Spectroscopy, J. Phys. Chem. A. **117** (29), 60846095 (2013).

ACKNOWLEDGEMENTS

I gratefully acknowledge my thesis advisor Jeff Cina who has taught me how to enjoy working, learning and thinking like a theoretical physical chemist.

For my wife Laura and son Edward, without the both of you this work would not have been possible, I'm sure of it.

TABLE OF CONTENTS

LIST OF FIGURES

Figure Page

LIST OF TABLES

Table Page

CHAPTER I

INTRODUCTION

The physical world is inherently time-dependent. Even apparently static conditions, often times, are under everlasting change. In the study of molecular spectroscopy, there are two complementary approaches in the interpretation of spectra: casting the spectra in the frequency domain or the corresponding time domain. The unifying theme of this dissertation is the calculation and interpretation of the building blocks of molecular spectroscopic signals with time as the foundation. The appeal of working in this frame is one is left thinking about dynamical wave packets and overlaps which lend themselves to different levels of treatment ranging from classical to fully quantum mechanical. Furthermore, classical intuition can easily be applied in a classical or semiclassical time-dependent picture maintaining a direct line of comparison between the macroscopic and molecular worlds.

There are three separate, but foundationally unified works in this dissertation. All involve a wave packet approach to dynamics and calculation of spectroscopic signals. Chapter II is a joint work between Jeff Cina and Phil Kovac being made ready for publication which discusses the use of a mixed quantum/semiclassical method in the simulation of dynamics and linear absorption for the realistic model system I_2Kr_6. The approach entitled Fixed Vibrational Basis/ Gaussian Bath theory (FVB/GB) has been developed to meet the challenges in the simulation of large-scale condensed phase systems. The study of energy transfer and decoherence phenomena between halogen molecules and a surrounding cryogenic noble gas host matrix is an area of strong focus where FVB/GB is particularly well suited. There

are several experimental studies on these unique molecular systems that emphasize the importance of quantum processes in the interaction between the simple guest chromophore and the highly ordered surrounding medium that could benefit from careful theoretical simulations and interpretation.[2, 3, 4, 5, 6]

As a mixed quantum/semiclassical approach FVB/GB theory at once offers rigorous treatment of local highly anharmonic vibrations together with an intuitive Gaussian wave packet picture of extended low amplitude phonon modes. Chapter II develops the theory of FVB/GB, provides a demonstration of its utility through the calcualtion of dynamics for I_2Kr_6, and includes an application of the theory in the calculation of a linear absorption spectrum for the model. The absorption spectrum is calculated with Heller's absorption expression[7] and compared with numerically exact results calculated with traditional basis set methods. Interpretation of the exact spectrum is facilitated through analysis of wave packet motion of the electronically excited model coupled with examination of the time-dependent absorption kernel to which the motion gives rise.

Introduced in chapter III is a rebuilding of the theory of transient-absorption spectroscopy. This technique allows for detection of prepared vibrational wave packets in the ground or excited electronic states of a molecular system.[8, 9, 10, 11, 12, 13] Of particular interest in this work is the source and meaning of the anti-phased oscillations about the Stokes-shifting node located at the wavelength of maximum fluorescence in a recent study of the photosynthetic light harvesting complex PC577.[1]

Expressions for the contributions to the time-dependent transient-absorption dipole moment are derived in terms of overlaps between wave packets that have interacted with the pump and probe fields and the transient absorption signal is

expressed as the pump induced change in the transmitted probe field. A transient-absorption spectrum is calculated for a model based on PC577 and the source of the anti-phased oscillations and the time-resolution of the technique are discussed. As an alternative strategy in processing these types of spectra, we propose analysis of the sign of the second derivative of an experimental data set to reveal the presence of vibrational quantum beats. This data processing is explained and attempted on simulated and experimental data sets without the use of background subtraction to reveal the vibrational features of interest in a transient absorption spectrum.

Chapter III was previously published in the Journal of Chemical Physics in 2016. It was initiated by Jeffrey Cina, Jeff Cina derived the expressions in the paper and performed all theoretical calculations. Philip Kovac checked the analytic results and performed the sign of second derivative calculations on the data sets for PC577 and methylene Blue provided graciously by Chanelle Jumper, Jacob Dean and Greg Scholes.

Chapter IV is motivated by the development and wide use of femtosecond stimulated Raman spectroscopy (FSRS) or fissors. The technique was first developed by Yoshizawa and Kurosawa[14] and has largely been improved upon by Mathies and coworkers to measure the effect of slow conformational motion on high frequency molecular vibrations.[15] Fissors measures the Raman gain in the power spectrum of a transmitted nonresonant probe pulse due to the presence of a pump pulse. Of special interest and largely the impetus for this work is a thorough explanation of the variation of the Raman gain close to vibrational peaks associated with high frequency modes due to their coupling with slower impulsively-driven conformational motion.

A two dimensional model system is developed consisting of a high-frequency mode coupled to a low frequency oscillation. Central to this work is the assumption of vibrationally adiabatic conformational motion which honors the typical large time-scale separation between vibrational and conformational motion. The fissors dipole is expressed as an overlap between conformational wave packets associated with the ground and first excited vibrational state. The dipole is found to turn on with the probe pulse and slowly fall-off with the trailing edge of the pump pulse together with vibrational dephasing evidenced by loss of overlap between conformational wave packets.

An analytic expression for the fissors signal composed of an integral over time of the time-dependent dipole times a window function is developed, and fissors signals are presented for two different cases of conformational mass. The resolution and information content of the signals in each case are discussed in terms of the time dependent fissors dipole. Further comments and explanation in terms of the dynamics of the model system are offered.

Chapter IV was previously published in the Journal of Physical Chemistry A in April 2013. Jeffrey Cina began this work. Jeffrey Cina and Philip Kovac derived all analytic expression and performed the calculations separately. Jeffrey A. Cina was the principle investigator during this work.

This dissertation is arranged as follows: Chapter II presents recent work of the application of FVB/GB theory in the calculation of linear absorption. Chapter III presents previously published work on transient absorption spectroscopy where the source of the anti-phased side-bands about the Stokes shifting node is explained. Chapter IV provides a theoretical work on femtosecond stimulated Raman scattering where the information content within experimental signals

is elucidated. Lastly, Chapter V is a discussion about all three works and provides suggestions for future work on these projects. Appendix A details the construction of several model systems for use with FVB/GB theory and discusses a multidimensional Gaussian wave packet approach for I_2Kr_6. Appendix B provides in depth formulas of the time-dependent transient absorption dipole expressions and clarifies the transformation of signal expressions from an integral over all space to an integral over time.

CHAPTER II

TESTING A WAVE PACKET DYNAMICAL APPROACH: AN APPLICATION OF A MIXED QUANTUM/SEMICLASSIAL METHOD IN THE CALCULATION OF LINEAR ABSORPTION

This work is currently unpublished with a manuscript in preparation. It was initiated jointly by Philip Kovac and Jeffrey Cina. Philip Kovac derived all expressions, performed all calculations in the manuscript and wrote the manuscript all with helpful guidance and correction from Jeffrey Cina. Jeffrey A. Cina was the principle investigator for this work.

Introduction

Over the past few decades, there has been much interest in understanding the coupled dynamics between a choromore and its surroundings.[2, 3, 16, 5, 6, 17, 18, 19, 20, 21] The complexity of the experimental observables measured to clarify these intricate processes is largely dependent upon the phase state of the molecular system under scurtiny. A particular class of test subjects studied primarily in the Apkarian group at UC Irvine and Nikolaus Schwentner's group at Freie Universitt Berlin consists of halogen molecules isolated in cryogenic noble gas matricies.[6, 2, 3, 20, 21, 22, 23, 24, 25, 26, 27, 28] The nearly zero Kelvin temperature of the samples provides an environment where interesting quantum effects can dominate, and the highly ordered structure of the lattice yields information about system-bath coupling unavailable in liquid or gas phase samples.

The isotropic surroundings and the lack of rotational degrees of freedom in these molecular crystals give rise to experimental results with features suggesting

rather complicated interactions between the guest and its host lattice. For example, a time-resolved coherent anti-Stokes Raman scattering study on iodine isolated in kyrpton revealed the presence of a local cage mode surrounding the iodine chromophore with a vibrational lifetime suggesting a decoupling of this mode from the bulk lattice.[2] A complementary pump-probe study providing additional evidence of a isolated zone around the chromophore saw the generation of coherent zone boundary phonons with coherence lifetimes of more then 10 ps.[24] The presence of these phenomena are common as revealed in studies of small molecules isolated in cold substances as common as water.[16, 17, 18, 19, 20, 21]

Further interpretation of these experimental results could be bolstered by a time-domain theoretical treatment of the dynamics and spectra these molecular systems. The challenge faced in developing this treatment is accurately representing all degrees of freedom while also maintaining a level of description that is computationally feasible. To this end, we have developed a mixed quantum/semiclassical treatment entitled Fixed Vibrational Basis/Gaussian Bath theory (FVB/GB) that combines rigorous quantum mechanical methods and an intuitive wave packet picture for the simulation of dynamics and spectroscopic signals from large scale condensed phase systems. Of significant importance in the use of mixed dynamical techniques is the computational improvement of the method over conventional basis set calculations. The exponential scaling of basis sets with the number of degrees of freedom is the main challenge in performing dynamics calculations for large molecular systems, and sidestepping this barrier is of central interest in our use of FVB/GB.

We present here the first application of FVB/GB in the calculation spectroscopic signals. Through the use of Heller's absorption kernel[7], the linear

absorption spectrum of I_2Kr_6—a realistic model cluster reminiscent of iodine isolated in an extended medium—is calculated and compared with the exact result found through basis set methods. As a wave function based theory, the structure of FVB/GB allows interpretation of time-dependent wave packet overlaps that give rise to spectroscopic signals facilitating an intuitive picture of otherwise complicated experimental information. Based on a system-bath decomposition, the dynamics mostly associated with the intramolecular motion of the guest chromophore are handled quantum mechanically with conventional basis set techniques. Separately, the degrees of freedom comprised mainly of the extended medium are subject to a thawed Gaussian form. The total time-dependent state is written as a sum of tensor products of system eigenstates times bath wave packets. Under this approach, the dynamics of the localized system coordinates contribute to the phase factors of the bath wave packets— the time-dependent state of a large molecular system is therefore tractable through the dynamics of a set of multi-dimensional Gaussian wave packets. The ansatz appeals to an intuitive classical picture of dynamics and supplies the additional information of the phase and width of the bath wave packets approaching a realistic depiction of quantum behavior. Similar in form to our approach is the Gaussian variant of the successful multiconfigurational time-dependent Hartree method (MCTDH) which combines variationally optimized single particle functions with a moving basis of Gaussian functions to solve the time-dependent Schrödinger equation.[29, 30]

The form of the ansatz is well chosen for the molecular systems of interest as the interactions between the guest chromophore and host lattice are governed by weak van der Waals forces. The initial state for the molecular complex is a tensor product of the ground system eigenstate times a bath wave packet whose width is

chosen such that the state honors the ground eigenstate of the total Hamiltonian. Further, in application to femtosecond spectroscopy, the form of the initial wave packet transferred to an excited state by an ultrashort pulse is also preserved under FVB/GB as a sum of tensor products of excited system eigenstates times bath wave packets with the same initial width but differing amplitude determined by Franck-Condon overlaps.

Gaussian approximations to time-dependent wave packets have been thoroughly implemented beginning with the works of Heller and coworkers.[31, 32] Futher development towards multiple Gaussian fits of wave packets and application of a variational principle to minimize the error in propagation soon followed.[33, 34] These early works were concerned with the simulation of spectra where the first few femtoseconds of wave packet motion were all that were required. These methods were therefore developed to be accurate for short times where most of the motion involved spreading and exit along a dissociation channel. Building upon these ideas, Rohrdanz and Cina[35] provided a demonstration of intermolecular communication between I_2 molecule and a Calcium atom separated in a ring of Argon atoms. This work utilized a multidimensional Gaussian wave packet description for all degrees of freedom and serves as the beginning steps towards FVB/GB theory. Shortly after, Chapman and Cina[36] proposed two alternative strategies towards a mixed quantum/semiclassical approach to spectroscopy. Numerical implementation of the fixed vibrational basis/Gaussian bath method was met with success in the calculation of dynamics and electronic absorption from an interesting test model system.[37] The theory was bought one step further with the implementation of the Dirac-Frenkel-McLachlan (DFM)[38, 39] variational principle into the FVB/GB algorythm improving upon norm and energy conservation difficulties met in use

of the locally quadratic approximation for potential surfaces.[31] This work also constitutes the first application of FVB/GB to a realistic model system of iodine in a two dimensional krypton lattice.

Continuing on the work of Cheng and Cina, we implement the DFM variational principle to variationally solve for the optimal time-derivative of the state. Instead of solving for the parameter equations of motion analytically, we numerically propagate the FVB/GB equations of motion through numerical integration. As will be discussed in the body of this chapter, we make simplifying approximations for the model system I_2Kr_6 to make this test round of calculations more feasible.

Theory

DFM Variational Principle

As a starting point within FVB/GB theory, we assume knowledge of the initial state of a multimode system. This assumption is well founded for halogen molecules in cryogenic noble gas matrices due to their few-Kelvin temperature. Given the initial state $|\Psi\rangle$ of a system at time zero the optimal $|\dot{\Psi}\rangle$ can be found by minimizing the Dirac-Frenkel-McLachlan (DFM)[38, 39, 32] functional:

$$F[|\dot{\Psi}\rangle] = \Big(i\langle\dot{\Psi}| + \langle\Psi|H\Big)\Big(H|\Psi\rangle - i|\dot{\Psi}\rangle\Big). \tag{2.1}$$

Here and for the rest of this work $\hbar = 1$. From Eq. (2.1), if it were possible to specify $|\dot{\Psi}\rangle$ exactly via the time-dependent Schroedinger equation, the DFM functional would of course vanish. Any variation $|\delta\dot{\Psi}\rangle$ away from the minimizing

$|\dot{\Psi}\rangle$ will produce no first order change in F, whence

$$0 = i\langle\delta\dot{\Psi}|H|\Psi\rangle - i\langle\Psi|H|\delta\dot{\Psi}\rangle + \langle\delta\dot{\Psi}|\dot{\Psi}\rangle + \langle\dot{\Psi}|\delta\dot{\Psi}\rangle,$$

or

$$0 = \mathrm{Re}\langle\delta\dot{\Psi}|\Big(|\dot{\Psi}\rangle + iH|\Psi\rangle\Big); \tag{2.2}$$

this is the Dirac-Frenkel-McLachlan minimization condition. Note that in general the Hamiltonian in Eq. (2.2) may be time-dependent.

In order to simplify notation, but without loss of generality, we parametrize the state $|\Psi\rangle$ with a finite number of time-dependent real parameters. Making use of the chain rule,

$|\dot{\Psi}\rangle = \sum_m |\frac{\partial\Psi}{\partial\lambda_m}\rangle\dot{\lambda}_m = \sum_m |\Psi_m\rangle\dot{\lambda}_m$, and similarly $|\delta\dot{\Psi}\rangle = \sum_m |\frac{\partial\Psi}{\partial\lambda_m}\rangle\delta\dot{\lambda}_m = \sum_m |\Psi_m\rangle\delta\dot{\lambda}_m$, with the definition $|\frac{\partial\Psi}{\partial\lambda_m}\rangle \equiv |\Psi_m\rangle$. From the above equalities, the minimizing condition becomes

$$0 = \sum_m \delta\dot{\lambda}_m \,\mathrm{Re}\langle\Psi_m|\Big(\sum_n |\Psi_n\rangle\dot{\lambda}_n + iH|\Psi\rangle\Big). \tag{2.3}$$

The variations in the parameter time-derivatives $\delta\dot{\lambda}_m$ are arbitrary and independent, so

$$0 = \mathrm{Re}\langle\Psi_m|\Big(\sum_n |\Psi_n\rangle\dot{\lambda}_n + iH|\Psi\rangle\Big), \tag{2.4}$$

or

$$\sum_n \mathrm{Re}\langle\Psi_m|\Psi_n\rangle\dot{\lambda}_n = \mathrm{Im}\langle\Psi_m|H|\Psi\rangle. \tag{2.5}$$

Defining $M_{mn} = \mathrm{Re}\langle\Psi_m|\Psi_n\rangle$ and $\chi_m = \mathrm{Im}\langle\Psi_m|H|\Psi\rangle$, we arrive at an expression for the m^{th} row of a system of linear differential equations:

$$M_m \cdot \dot{\lambda} = \chi_m. \tag{2.6}$$

Hence

$$\dot{\lambda} = (M)^{-1} \cdot \chi, \tag{2.7}$$

where λ is a vector containing the parameters, and M is a real-symmetric matrix. Equation (2.7) is our means of propagating the initial state $|\Psi\rangle$ through time.

The present notation enables a simple verification of norm and energy conservation under DFM dynamics.[34, 40] Beginning with Eq. (2.2), we consider a variation of the form $|\delta\dot{\Psi}\rangle = \delta\dot{b}|\Psi\rangle$. That this form is possible under within FVB/GB, it is sufficient that parameters appear in the state such that $|\dot{\Psi}\rangle = \sum_n |\Psi_n\rangle\dot{\lambda}_n$ which implies $|\delta\dot{\Psi}\rangle = \sum_n |\Psi_n\rangle\delta\dot{\lambda}_n$, which will be shown to be true under the FVB/GB ansatz. Considering a variation of this form yields

$$0 = \delta\dot{b}\,\mathrm{Re}\langle\Psi|\Big(|\dot{\Psi}\rangle + iH|\Psi\rangle\Big), \tag{2.8}$$

whence

$$0 = 2\,\mathrm{Re}\langle\Psi|\Big(|\dot{\Psi}\rangle + iH|\Psi\rangle\Big) = \langle\Psi|\dot{\Psi}\rangle + \langle\dot{\Psi}|\Psi\rangle = \frac{d}{dt}\langle\Psi|\Psi\rangle. \tag{2.9}$$

Similarly, energy conservation may be shown by assuming a variation of the form $|\delta\dot{\Psi}\rangle = i|\dot{\Psi}\rangle\delta b$. Equation (2.2) now becomes

$$0 = \delta b\,\mathrm{Re}\Big[-i\langle\dot{\Psi}|\Big(|\dot{\Psi}\rangle + iH|\Psi\rangle\Big)\Big] = \delta b\,\mathrm{Im}\langle\dot{\Psi}|\Big(|\dot{\Psi}\rangle + iH|\Psi\rangle\Big). \tag{2.10}$$

The variation δb is arbitrary, which yields $0 = \mathrm{Im}\langle\dot{\Psi}|\Big(|\dot{\Psi}\rangle + iH|\Psi\rangle\Big)$, or upon simplification and multiplication by $-i$

$$0 = \frac{d}{dt}\langle\Psi|H|\Psi\rangle, \tag{2.11}$$

for a time-independent Hamiltonian.

We can show that for such a variation to be among those possible, it is sufficient that for all even indices n, real parameters λ_n and λ_{n+1} enter the trial state $|\Psi\rangle$ in the form $\lambda_n + i\lambda_{n+1}$. In this case, $|\dot{\Psi}\rangle = \sum_{n\ \mathrm{even}} |\Psi_n\rangle(\dot{\lambda}_n + i\dot{\lambda}_{n+1})$ and $|\delta\dot{\Psi}\rangle = \sum_{n\ \mathrm{even}} |\Psi_n\rangle(\delta\dot{\lambda}_n + i\delta\dot{\lambda}_{n+1})$. Here $i\delta b|\dot{\Psi}\rangle = \sum_{n\ \mathrm{even}} |\Psi_n\rangle(-\delta b\dot{\lambda}_{n+1} + i\delta b\dot{\lambda}_n)$, hence the existence of variations with $\delta\dot{\lambda}_n = -\delta b\dot{\lambda}_{n+1}$ and $\delta\dot{\lambda}_{n+1} = \delta b\dot{\lambda}_n$, which will be shown to be present in the FVB/GB ansatz, are enough to ensure energy conservation.

Variational FVB/GB Theory

System-Bath Decomposition and Model Hamiltonian

There is a significant time scale separation in a molecular iodine doped krypton lattice: the I_2 vibration (≈ 200 cm^{-1}) is about four times the Debye frequency of a pure krypton lattice (≈ 50 cm^{-1}).[2, 3, 41] Due to this property, and the weak van der Waals interactions between the iodine and krypton atoms, a transformation from Cartesian to mass-weighted normal coordinates yields a set of normal modes whose frequencies can be used to distinguish a system coordinate (localized on the I_2) and a set of bath modes (comprising mostly atomic Kr displacements) for a model system. Following the detailed approach of Chapman

and Cina,[36] we clarify the steps used to define the system and bath coordinates in the ground electronic state of the I_2 chromophore embedded in a krypton lattice.

The time-independent bare molecular Hamiltonian of the N-body model is defined as $H = |g\rangle H_g \langle g| + |e\rangle H_e \langle e|$, with the total nuclear Hamiltonian in the ground electronic state of the I_2 molecule having the form,

$$H_g = \frac{1}{2} p \cdot \mathbf{M} \cdot p + V_g(r). \tag{2.12}$$

In Eq. (2.12), p is the N-dimensional momentum vector, $\mathbf{M}$ is an $N \times N$ matrix with elements $\mathbf{M}_{ij} = (1/m_i)\delta_{ij}$ specifying the inverse mass appropriate to each degree of freedom, and the total potential energy function $V_g(r)$ has as its argument the N dimensional Cartesian coordinate vector r.

To rewrite the Cartesian coordinates and momenta in terms normal coordinates and their conjugate momenta, we first transform the ground state nuclear Hamiltonian into a function of mass-weighted displacement coordinates and momenta. Defining $\Pi = D \cdot p$ and $R = D^{-1} \cdot (r - r^{(0)})$, where $D = \sqrt{\mathbf{M}}$ and $r^{(0)}$ specifies a minimum energy configuration of the structure (found, for example, through a molecular dynamics cooling simulation), the Hamiltonian of Eq. (2.12) becomes

$$H_g = \frac{1}{2} \Pi \cdot \Pi + V_g(D \cdot R + r^{(0)}). \tag{2.13}$$

For the purpose of identifying the force constant matrix we *temporarily* expand the ground state total potential energy function through second order as,

$$V_g(D \cdot R + r^{(0)}) \approx V_g(r^{(0)}) + \frac{1}{2} R \cdot \Big(\big(\nabla_R \nabla_R V_g(D \cdot R + r^{(0)}) \big) \big|_{R=0} \Big) \cdot R. \tag{2.14}$$

Note that the derivative in the first order term of this expansion, $\nabla_R V_g(D \cdot R + r^{(0)}))|_{R=0}$ is assumed to be zero as the argument of the potential is the minimum energy configuration $r^{(0)}$.

The force constant matrix, whose elements are $\frac{1}{\sqrt{m_i m_j}}\left(\frac{\partial^2 V_g(r)}{\partial r_i \partial r_j}\right)\Big|_{r=r^{(0)}}$, can be diagonalized by an orthogonal transformation,

$$(\nabla_R \nabla_R V_g) \cdot \Lambda = \Lambda \cdot \zeta. \tag{2.15}$$

The columns of Λ, are the eigenvectors of the force constant matrix whose eigenvalues are arranged in order of decreasing size along the diagonal of ζ. Utilizing the transformation matrix, we define the normal coordinates of the complex as $\xi = \Lambda^\top \cdot R$, and the normal momenta are taken to be $\pi = \Lambda^\top \cdot \Pi$. In terms of these normal coordinates and momenta, the nuclear Hamiltonian for the model system in the ground electronic state of the I_2 chromophore is

$$H_g = \frac{1}{2}\pi \cdot \pi + V_g(D \cdot \Lambda \cdot \xi + r^{(0)}). \tag{2.16}$$

It is important to note that, in expressing the argument of the ground state potential in terms of normal coordinates, we are *not* truncating the total potential energy function at second order. All anharmonic interactions within the potential are retained; the normal coordinates are used strictly to define the vibrational modes of the system, and will be useful in specifying the vibrational ground state as the quantum mechanical initial condition of the cluster.

Making use of the normal coordinates and momenta, we can effect a system-bath decomposition. The model system is a three-dimensional non-colinear structure, hence we obtain $3N - 6$ normal coordinates of nonzero

frequency. The frequencies of the six coordinates associated with rotation and translation of the center of mass of the cluster are assigned zero values, and therefore the cluster is fixed in space and cannot rotate. We make our system bath decomposition by defining the highest-frequency coordinate—whose predominant Cartesian component is the I_2 stretching vibration— as the system coordinate q. The corresponding system momentum is defined as p.[1] The remaining normal coordinates are assigned to the bath coordinate, denoted by the vector Q with corresponding normal momentum P.

Our approach to partitioning the system from the bath is flexible in that it is straight forward to include more then one mode in the system. This allows for the incorporation of certain bath modes that may be found to be strongly coupled to the system despite initially having a vibrational period comparable to the extended krypton lattice.

With the well defined separation between the system and bath, the nuclear Hamiltonian in the ground electronic state of I_2 may be written as a sum of system, bath, and interaction terms

$$H_g = h_g(q) + k_g(Q) + v_g(q, Q). \tag{2.17}$$

The system Hamiltonian is

$$h(q) = \frac{p^2}{2} + u(q), \tag{2.18}$$

and the bath Hamiltonian has the form

$$k(Q) = \frac{1}{2} P \cdot P + U(Q). \tag{2.19}$$

[1]Not to be confused with the N-component atomic momentum vector for which the same symbol was used in Eq. (2.12).

In the above notation, $p = \pi_1$ and $q = \xi_1$. Similarly, $P = (\pi_2, \pi_3, ..., \pi_{3N-7}, \pi_{3N-6}, 0, 0, 0, 0, 0, 0)$ and $Q = (\xi_2, \xi_3, ..., \xi_{3N-7}, \xi_{3N-6}, 0, 0, 0, 0, 0, 0)$. The system and bath potentials are defined as

$$\begin{aligned} u(q) &= V(q, 0) \\ &= V(D \cdot \Lambda \cdot (\xi_1, 0, 0, ..., 0, 0) + r^{(0)}), \end{aligned} \tag{2.20}$$

$$\begin{aligned} U(Q) &= V(0, Q) - V(0, 0) \\ &= V(D \cdot \Lambda \cdot (0, \xi_2, \xi_3, ..., \xi_{3N-7}, \xi_{3N-6}, 0, 0, 0, 0, 0, 0) + r^{(0)}) \\ &\quad - V(D \cdot \Lambda \cdot (0, 0, 0, ..., 0, 0) + r^{(0)}). \end{aligned} \tag{2.21}$$

Note that the bath potential energy is defined to be zero at $Q = 0$. Finally, the system-bath interaction potential is defined as

$$\begin{aligned} v(q, Q) &= V(q, Q) - u(q) - U(Q) \\ &= V(D \cdot \Lambda \cdot \xi + r^{(0)}) - u(q) - U(Q). \end{aligned} \tag{2.22}$$

Since we've made a system-bath decomposition based on the normal coordinates in the ground electronic state of the I_2 molecule, the ground state interaction potential has no bi-linear terms; the lowest order terms in $v_g(q, Q)$ are qQ^2 and q^2Q. The excited state interaction potential may have bi-linear terms as both the system and bath potential surfaces change upon electronic excitation of the system coordinate.

The definitions of the normal coordinates remain the same under electronic excitation of the system coordinate. The nuclear Hamiltonian in the excited

electronic state has the form

$$H_e = h_e(q) + k_e(Q) + v_e(q, Q) + \epsilon \tag{2.23}$$

with ϵ being the bare electronic transition energy. In practice the numerical value of ϵ is arbitrary, and will be subtracted off all spectra in this work. The definitions of the system and bath Hamiltonians and the interaction potential as shown in Eqs. (2.18)-(2.22) remain the same in the electronic excited state, with the exception that the total potential V changes under electronic excitation.

Referring back to Eq. (2.2), the state $|\Psi\rangle$ is defined by utilizing the system-bath decomposition. The system dynamics are handled with conventional basis set methods where the eigenstates of the ground- and excited-state system Hamiltonians, obeying

$$h_j|\nu_j\rangle = \epsilon_{\nu_j}|\nu_j\rangle, \tag{2.24}$$

are used as bases. With these basis sets, an arbitrary state can be written as a sum of a sum of tensor products

$$|\Psi\rangle = |g\rangle \sum_{\nu_g} |\nu_g\rangle|\psi_{\nu_g}\rangle + |e\rangle \sum_{\nu_e} |\nu_e\rangle|\psi_{\nu_e}\rangle, \tag{2.25}$$

where $\langle\nu_j|\langle j|\Psi\rangle = |\psi_{\nu_j}\rangle$. In general, there is a unique bath state $|\psi_{\nu_j}\rangle$ for each system state in Eq. (2.25). Working in the position representation, we make a Gaussian ansatz for the form of the bath wave packet accompanying a given system state:

$$\langle Q|\psi_{\nu_j}\rangle = a_{\nu_j} \exp\{\alpha_{\nu_j} Q^2 + \beta_{\nu_j} Q + i\gamma_{\nu_j}\}, \tag{2.26}$$

where a_{ν_j} and γ_{ν_j} are real parameters, $\alpha_{\nu_j} = \alpha'_{\nu_j} + i\alpha''_{\nu_j}$ and $\beta_{\nu_j} = \beta'_{\nu_j} + i\beta''_{\nu_j}$. In Eq. (2.26), α_{ν_j} must be negative given the form of the bath wave functions.

Making use of the ansatz, the initial state is assumed to have the form

$$|\Psi(t=0)\rangle \equiv |\Psi_0\rangle = |g\rangle|0_g\rangle|\psi_{0_g}\rangle. \tag{2.27}$$

We've written $|\Psi_0\rangle$ as a system-bath tensor product by making use of the fact that $v_g(q,Q)$ has no bi-linear terms, and neglecting any higher order system-bath coupling terms in the lowest energy state of the composite system. We make the further assumption that cubic and higher order terms do not significantly affect the ground state of the bath so that the bath wave packet at $t = 0$ conforms to our Gaussian ansatz. With these assumptions, the initial bath wave packet takes the form

$$\langle Q|\psi_{0_g}\rangle = \left(\frac{\omega_b}{\pi}\right)^{1/4} \exp\left\{-\frac{\omega_b}{2}Q^2\right\}, \tag{2.28}$$

with $\omega_b = (d^2U_g(Q)/dQ^2)^{1/2}\Big|_{Q=0}$.

Evaluation of terms in FVB/GB Equations of Motion

Our development of FVB/GB theory so far has been general with no specification of the model under study or the size of the system and bath degrees of freedom. We have developed several model clusters ranging in size from 8 - 184 atoms which more realistically depict I_2 in an extended krypton lattice as the number of krypton atoms increases. For the purposes of this work, where the aim is to apply FVB/GB to the calculation of a linear absorption spectrum, we focus on a seemingly simple model complex, I_2Kr_6. Further, given that electronic excitation of the system coordinate results in a symmetric displacement of the I_2 molecule, we

suppress motion in all non totally symmetric bath coordinates as these coordinates are not Franck-Condon active. The resulting model is a two-dimensional complex comprising one system and one bath coordinate. In the following derivation of the terms M and χ in the FVB/GB equations, the coordinate Q and the bath wave packet parameters α_ν and β_ν are scalars denoting the one-dimensional bath of I_2Kr_6.

Evaluation of M

Propagation of the bath wave packet parameters requires evaluation of the terms M and χ in Eq. (2.7). Beginning with the mn^{th} element of M, $M_{mn} = \text{Re}\langle\Psi_m|\Psi_n\rangle$ it is easily seen that any overlap between bath wave packets corresponding to different vibronic states vanishes:

$$\begin{aligned}\langle\Psi_m|\Psi_n\rangle &= \Big(\sum_{\nu_g}\langle\psi_{\nu_g m}|\langle\nu_g|\langle g| + \sum_{\nu_e}\langle\psi_{\nu_e m}|\langle\nu_e|\langle e|\Big)\Big(|g\rangle\sum_{\bar{\nu}_g}|\bar{\nu}_g\rangle|\psi_{\bar{\nu}_g n}\rangle + |e\rangle\sum_{\bar{\nu}_e}|\bar{\nu}_e\rangle|\psi_{\bar{\nu}_e n}\rangle\Big)\\ &= \sum_{\nu_g}\langle\psi_{\nu_g m}|\psi_{\nu_g n}\rangle + \sum_{\nu_e}\langle\psi_{\nu_e m}|\psi_{\nu_e n}\rangle, \qquad (2.29)\end{aligned}$$

here we have extended the parameter-subscript notation to denote differentiation of bath wave packets with respect to specific parameters. For the purposes of calculating a linear absorption spectrum, the ground state contribution to $\langle\Psi_m|\Psi_n\rangle$ is unnecessary, and

$$\langle\Psi_m|\Psi_n\rangle = \sum_{\nu_e}\langle\psi_{\nu_e m}|\psi_{\nu_e n}\rangle. \qquad (2.30)$$

The only nonvanishing contribution to the above overlap is when both m and n assume parameter values that belong to the same ν_e bath wave packet.

Analytic expressions for the surviving bath wave packet overlaps $\langle\psi_{\nu_e m}|\psi_{\nu_e n}\rangle$ are found by representing the ν_e^{th} bath wave packet in the position representation

and evaluating the six unique derivatives with respect to the parameters specifying the ν_e^{th} bath wave packet:

$$\langle Q|\psi_{\nu a_\nu}\rangle = \frac{1}{a_\nu}\langle Q|\psi_\nu\rangle, \tag{2.31}$$

$$\langle Q|\psi_{\nu\gamma_\nu}\rangle = i\langle Q|\psi_\nu\rangle, \tag{2.32}$$

$$\langle Q|\psi_{\nu\beta'_\nu}\rangle = Q\langle Q|\psi_\nu\rangle, \tag{2.33}$$

$$\langle Q|\psi_{\nu\beta''_\nu}\rangle = iQ\langle Q|\psi_\nu\rangle, \tag{2.34}$$

$$\langle Q|\psi_{\nu\alpha'_\nu}\rangle = Q^2\langle Q|\psi_\nu\rangle, \tag{2.35}$$

$$\langle Q|\psi_{\nu\alpha''_\nu}\rangle = iQ^2\langle Q|\psi_\nu\rangle. \tag{2.36}$$

In Eqs.(2.31)-(2.36) and in remainder of section 2.2 we drop the electronic subscript on the bath wave packets for brevity of presentation. Combining Eqs. (2.30)-(2.36), and using the fact that $\langle\psi_{\nu m}|\psi_{\nu n}\rangle$ must be real to yield a nonvanishing contribution to M, under our FVB/GB ansatz this matrix is block diagonal, with one 6×6 block for each system eigenstate. For a given system state ν:

$$M_\nu = \begin{bmatrix}
\frac{1}{a_\nu^2}\langle\psi_\nu|\psi_\nu\rangle & 0 & \frac{1}{a_\nu}\langle\psi_\nu|Q|\psi_\nu\rangle & 0 & \frac{1}{a_\nu}\langle\psi_\nu|Q^2|\psi_\nu\rangle & 0 \\
0 & \langle\psi_\nu|\psi_\nu\rangle & 0 & \langle\psi_\nu|Q|\psi_\nu\rangle & 0 & \langle\psi_\nu|Q^2|\psi_\nu\rangle \\
\frac{1}{a_\nu}\langle\psi_\nu|Q|\psi_\nu\rangle & 0 & \langle\psi_\nu|Q^2|\psi_\nu\rangle & 0 & \langle\psi_\nu|Q^3|\psi_\nu\rangle & 0 \\
0 & \langle\psi_\nu|Q|\psi_\nu\rangle & 0 & \langle\psi_\nu|Q^2|\psi_\nu\rangle & 0 & \langle\psi_\nu|Q^3|\psi_\nu\rangle \\
\frac{1}{a_\nu}\langle\psi_\nu|Q^2|\psi_\nu\rangle & 0 & \langle\psi_\nu|Q^3|\psi_\nu\rangle & 0 & \langle\psi_\nu|Q^4|\psi_\nu\rangle & 0 \\
0 & \langle\psi_\nu|Q^2|\psi_\nu\rangle & 0 & \langle\psi_\nu|Q^3|\psi_\nu\rangle & 0 & \langle\psi_\nu|Q^4|\psi_\nu\rangle
\end{bmatrix}. \tag{2.37}$$

The complete evaluation of M_ν and the subsequent evaluation of χ in the next section requires the following Gaussian integrals:

$$I_{0_\nu} = \langle\psi_\nu|\psi_\nu\rangle \equiv n_\nu = \int dQ\langle\psi_\nu|Q\rangle\langle Q|\psi_\nu\rangle \tag{2.38}$$

$$= a_\nu^2 \,\mathrm{Exp}\Big\{ -\frac{{\beta'_\nu}^2}{2\alpha'_\nu}\Big\}\sqrt{\frac{\pi}{-2\alpha'_\nu}},$$

$$I_{1_\nu} = \langle\psi_\nu|Q|\psi_\nu\rangle = \frac{1}{2}\frac{\partial}{\partial\beta'_\nu}n_\nu = -\frac{\beta'_\nu}{2\alpha'_\nu}n_\nu, \tag{2.39}$$

$$I_{2_\nu} = \langle\psi_\nu|Q^2|\psi_\nu\rangle = \frac{1}{2}\frac{\partial}{\partial\beta'_\nu}I_{1_\nu} = -\frac{1}{4\alpha'_\nu}\left(1 - \frac{{\beta'_\nu}^2}{\alpha'_\nu}\right)n_\nu, \tag{2.40}$$

$$I_{3_\nu} = \langle\psi_\nu|Q^3|\psi_\nu\rangle = \frac{1}{2}\frac{\partial}{\partial\beta'_\nu}I_{2_\nu} = \frac{\beta'_\nu}{8{\alpha'_\nu}^2}\left(3 - \frac{{\beta'_\nu}^2}{\alpha'_\nu}\right)n_\nu, \tag{2.41}$$

$$I_{4_\nu} = \langle\psi_\nu|Q^4|\psi_\nu\rangle = \frac{1}{2}\frac{\partial}{\partial\beta'_\nu}I_{3_\nu} \tag{2.42}$$

$$= \frac{1}{16{\alpha'_\nu}^2}\left(3 - 6\frac{{\beta'_\nu}^2}{\alpha'_\nu} + \frac{{\beta'_\nu}^4}{{\alpha'_\nu}^2}\right)n_\nu,$$

$$I_{5_\nu} = \langle\psi_\nu|Q^5|\psi_\nu\rangle = \frac{1}{2}\frac{\partial}{\partial\beta'_\nu}I_{4_\nu} \tag{2.43}$$

$$= -\frac{\beta'_\nu}{32{\alpha'_\nu}^3}\left(15 - 10\frac{{\beta'_\nu}^2}{\alpha'_\nu} + \frac{{\beta'_\nu}^4}{{\alpha'_\nu}^2}\right)n_\nu,$$

$$I_{6_\nu} = \langle\psi_\nu|Q^6|\psi_\nu\rangle = \frac{1}{2}\frac{\partial}{\partial\beta'_\nu}I_{5_\nu} \tag{2.44}$$

$$= -\frac{1}{64{\alpha'_\nu}^3}\left(15 - 45\frac{{\beta'_\nu}^2}{\alpha'_\nu} + 15\frac{{\beta'_\nu}^4}{{\alpha'_\nu}^2} - \frac{{\beta'_\nu}^6}{{\alpha'_\nu}^3}\right)n_\nu.$$

Note the presence of a_ν^2 in the term n_ν which appears in all of the above integral expressions. This factor cancels the denominator a_ν appearing in some of the elements in the matrix expression for M_ν, and forestalls numerical problems for sparsely populated system states.

Evaluation of χ

An element of the vector χ in Eq. (2.7), has the form $\chi_m = \mathrm{Im}\langle\Psi_m|H|\Psi\rangle$. The molecular Hamiltonian H does not include an electric field to couple the ground and excited electronic states; nonvanishing contributions to χ_m are matrix elements of system eigenstates times bath wave packets belonging to the same electronic state. Again, the nuclear dynamics that must be tracked in calculating absorption takes place on the excited electronic state, and we need only consider these contributions to χ. For the present purposes then, then m^{th} element of this vector has the form

$$\chi_m = \sum_{\nu_e,\bar{\nu}_e} \mathrm{Im}\langle\psi_{\nu_e m}|\langle\nu_e|H_e|\bar{\nu}_e\rangle|\psi_{\bar{\nu}_e}\rangle, \tag{2.45}$$

and the summand may only be nonvanishing for the ν -value whose bath wave packet $\langle\psi_\nu|$ depends on the particular λ_m. Considering the matrix element $\langle\psi_{\nu_e m}|\langle\nu_e|H_e|\bar{\nu}_e\rangle|\psi_{\bar{\nu}_e}\rangle$, this quantity is nonvanishing when m takes on a parameter value that belongs to the ν_e bath wave packet.

From the definition of H_e we find

$$\chi_m = \sum_{\nu,\bar{\nu}} \mathrm{Im}\langle\psi_{\nu\, m}|\langle\nu|\Big(h(q) + k(Q) + v(q,Q) + \epsilon\Big)|\bar{\nu}\rangle|\psi_{\bar{\nu}}\rangle, \tag{2.46}$$

where we have again suppressed the electronic subscripts for clarity. This equation simplifies to

$$\chi_m = \sum_{\nu,\bar{\nu}} \mathrm{Im}\langle\psi_{\nu\, m}|\Bigg\{\Big(\epsilon_\nu + \frac{P^2}{2} + U(Q) + \epsilon\Big)\delta_{\nu,\bar{\nu}} + v_{\nu,\bar{\nu}}(Q)\Bigg\}|\psi_{\bar{\nu}}\rangle, \tag{2.47}$$

where $\langle\nu|v(q,Q)|\bar{\nu}\rangle = v_{\nu\bar{\nu}}(Q)$ by making use of the definitions of the system and bath Hamiltonians. In the position representation, the bath kinetic energy operator

is expressed as

$$\frac{1}{2}\langle Q|P^2|\psi_\nu\rangle = -\frac{1}{2}\frac{\partial^2}{\partial Q^2}\langle Q|\psi_\nu\rangle = -\Big(\alpha_\nu + \frac{\beta_\nu^2}{2} + 2\alpha_\nu\beta_\nu Q + 2\alpha_\nu^2 Q^2\Big)\langle Q|\psi_\nu\rangle, \quad (2.48)$$

and upon substitution into Eq. (2.47)

$$\chi_m = \sum_{\nu,\bar{\nu}} \mathrm{Im}\langle\psi_{\nu\,m}|\Bigg\{\Bigg(\epsilon_\nu - \alpha_\nu - \frac{\beta_\nu^2}{2} - 2\alpha_\nu\beta_\nu Q - 2\alpha_\nu^2 Q^2 + U(Q) + \epsilon\Bigg)\delta_{\nu,\bar{\nu}} + v_{\nu,\bar{\nu}}(Q)\Bigg\}|\psi_{\bar{\nu}}\rangle. \quad (2.49)$$

When the index m is assigned to one of the six unique parameter values specifying the ν^{th} bath wave packet in the electronic excited state, Eq. (2.49) may be further simplified. For $m = a_\nu$

$$\chi_{a_\nu} = \frac{1}{a_\nu}\,\mathrm{Im}\Bigg\{\Big(\epsilon_\nu - \alpha_\nu - \frac{\beta_\nu^2}{2} + \epsilon\Big)n_\nu - 2\alpha_\nu\beta_\nu I_{1_\nu} - 2\alpha_\nu^2 I_{2_\nu} + \langle\psi_\nu|U(Q)|\psi_\nu\rangle + \sum_{\bar{\nu}}\langle\psi_\nu|v_{\nu\bar{\nu}}(Q)|\psi_{\bar{\nu}}\rangle\Bigg\}, \quad (2.50)$$

or implementing the definitions for n_ν, I_{1_ν} and I_{2_ν} and taking the imaginary part

$$\chi_{a_\nu} = \frac{1}{a_\nu}\sum_{\bar{\nu}}\mathrm{Im}\langle\psi_\nu|v_{\nu\bar{\nu}}(Q)|\psi_{\bar{\nu}}\rangle. \quad (2.51)$$

For the case $\lambda_m = \gamma_\nu$, we have $\langle\psi_{\nu\gamma_\nu}| = -ia_\nu\langle\psi_{\nu a_\nu}|$ whence

$$\chi_{\gamma_\nu} = -\,\mathrm{Re}\Bigg\{\Big(\epsilon_\nu - \alpha_\nu - \frac{\beta_\nu^2}{2} + \epsilon\Big)n_\nu - 2\alpha_\nu\beta_\nu I_{1_\nu} - 2\alpha_\nu^2 I_{2_\nu} + \langle\psi_\nu|U(Q)|\psi_\nu\rangle + \sum_{\bar{\nu}}\langle\psi_\nu|v_{\nu\bar{\nu}}(Q)|\psi_{\bar{\nu}}\rangle\Bigg\}. \quad (2.52)$$

Substituting in the expressions for n_ν, I_{1_ν} and I_{2_ν} and taking the real part we find

$$\chi_{\gamma_\nu} = -\Bigg\{\left(\epsilon_\nu + \frac{\alpha_\nu''^{\,2}\beta_\nu'^{\,2}}{2\alpha_\nu'^{\,2}} - \frac{\alpha_\nu''^{\,2}}{2\alpha_\nu'} - \frac{\alpha_\nu''\beta_\nu'\beta_\nu''}{\alpha_\nu'} - \frac{\alpha_\nu'}{2} + \frac{\beta_\nu''^{\,2}}{2} + \epsilon\right) n_\nu \\ + \langle\psi_\nu|U(Q)|\psi_\nu\rangle + \sum_{\bar\nu} \mathrm{Re}\langle\psi_\nu|v_{\nu\bar\nu}(Q)|\psi_{\bar\nu}\rangle\Bigg\}. \quad (2.53)$$

For $m = \beta_\nu'$, the expression for χ_m becomes

$$\chi_{\beta_\nu'} = \mathrm{Im}\Bigg\{\Big(\epsilon_\nu - \alpha_\nu - \frac{\beta_\nu^2}{2} + \epsilon\Big) I_{1_\nu} - 2\alpha_\nu\beta_\nu I_{2_\nu} - 2\alpha_\nu^2 I_{3_\nu} \\ + \langle\psi_\nu|QU(Q)|\psi_\nu\rangle + \sum_{\bar\nu}\langle\psi_\nu|Qv_{\nu\bar\nu}(Q)|\psi_{\bar\nu}\rangle\Bigg\}, \quad (2.54)$$

which leads to

$$\chi_{\beta_\nu'} = \left\{\left(\frac{\beta_\nu''}{2} - \frac{\alpha_\nu''\beta_\nu'}{2\alpha_\nu'}\right) n_\nu + \sum_{\bar\nu}\mathrm{Im}\langle\psi_\nu|Qv_{\nu\bar\nu}(Q)|\psi_{\bar\nu}\rangle\right\}, \quad (2.55)$$

using the definitions of I_{1_ν}, I_{2_ν} and I_{3_ν} and taking the imaginary part.

Because $\langle\psi_{\nu\beta_\nu''}| = -i\langle\psi_{\nu\beta_\nu'}|$, when $\lambda_m = \beta_\nu''$ we have

$$\chi_{\beta_\nu''} = -\,\mathrm{Re}\Bigg\{\Big(\epsilon_\nu - \alpha_\nu - \frac{\beta_\nu^2}{2} + \epsilon\Big) I_{1_\nu} - 2\alpha_\nu\beta_\nu I_{2_\nu} - 2\alpha_\nu^2 I_{3_\nu} \\ + \langle\psi_\nu|QU(Q)|\psi_\nu\rangle + \sum_{\bar\nu}\langle\psi_\nu|Qv_{\nu\bar\nu}(Q)|\psi_{\bar\nu}\rangle\Bigg\}, \quad (2.56)$$

or after simplifying

$$\chi_{\beta''_\nu} = -\Bigg\{\Bigg(-\frac{\alpha''^{\,2}_\nu \beta'^{\,3}_\nu}{4\alpha'^{\,3}_\nu} + \frac{3\alpha''^{\,2}_\nu \beta'_\nu}{4\alpha'^{\,2}_\nu} + \frac{\alpha''_\nu \beta'^{\,2}_\nu \beta''_\nu}{2\alpha'^{\,2}_\nu} - \frac{\alpha''_\nu \beta''_\nu}{2\alpha'_\nu} - \frac{\beta'_\nu \beta''^{\,2}_\nu}{4\alpha'_\nu} - \frac{\beta'_\nu \epsilon_\nu}{2\alpha'_\nu} + \frac{\beta'_\nu}{4} - \epsilon\frac{\beta'_\nu}{2\alpha'_\nu}\Bigg) n_\nu$$
$$+ \langle\psi_\nu|QU(Q)|\psi_\nu\rangle + \sum_{\bar\nu} \mathrm{Re}\langle\psi_\nu|Q v_{\nu\bar\nu}(Q)|\psi_{\bar\nu}\rangle\Bigg\}. \quad (2.57)$$

For $m = \alpha'_\nu$ we have

$$\chi_{\alpha'_\nu} = \mathrm{Im}\Bigg\{\Big(\epsilon_\nu - \alpha_\nu - \frac{\beta_\nu^2}{2} + \epsilon\Big) I_{2_\nu} - 2\alpha_\nu\beta_\nu I_{3_\nu} - 2\alpha_\nu^2 I_{4_\nu}$$
$$+ \langle\psi_\nu|Q^2U(Q)|\psi_\nu\rangle + \sum_{\bar\nu}\langle\psi_\nu|Q^2 v_{\nu\bar\nu}(Q)|\psi_{\bar\nu}\rangle\Bigg\}, \quad (2.58)$$

which simplifies to

$$\chi_{\alpha'_\nu} = \Bigg\{\Bigg(\frac{\alpha''_\nu \beta'^{\,2}_\nu}{2\alpha'^{\,2}_\nu} - \frac{\alpha''_\nu}{2\alpha'_\nu} - \frac{\beta'_\nu\beta''_\nu}{2\alpha'_\nu}\Bigg) n_\nu$$
$$+ \langle\psi_\nu|Q^2U(Q)|\psi_\nu\rangle + \sum_{\bar\nu}\mathrm{Im}\langle\psi_\nu|Q^2 v_{\nu\bar\nu}(Q)|\psi_{\bar\nu}\rangle\Bigg\}. \quad (2.59)$$

Finally, invoking $\langle\psi_{\nu\alpha''_\nu}| = -i\langle\psi_{\nu\alpha'_\nu}|$

$$\chi_{\alpha''_\nu} = -\,\mathrm{Re}\Bigg\{\Big(\epsilon_\nu - \alpha_\nu - \frac{\beta_\nu^2}{2} + \epsilon\Big) I_{2_\nu} - 2\alpha_\nu\beta_\nu I_{3_\nu} - 2\alpha_\nu^2 I_{4_\nu}$$
$$+ \langle\psi_\nu|Q^2U(Q)|\psi_\nu\rangle + \sum_{\bar\nu}\langle\psi_\nu|Q^2 v_{\nu\bar\nu}(Q)|\psi_{\bar\nu}\rangle\Bigg\}, \quad (2.60)$$

or

$$\chi_{\alpha''_\nu} = -\Bigg\{\Bigg(\frac{\alpha''^{\,2}_\nu \beta'^{\,4}_\nu}{8\alpha'^{\,4}_\nu} - \frac{3\alpha''^{\,2}_\nu \beta'^{\,2}_\nu}{4\alpha'^{\,3}_\nu} - \frac{\alpha''_\nu \beta'^{\,3}_\nu \beta''_\nu}{4\alpha'^{\,3}_\nu} + \frac{3\alpha''^{\,2}_\nu}{8\alpha'^{\,2}_\nu} + \frac{3\alpha''_\nu \beta'_\nu \beta''_\nu}{4\alpha'^{\,2}_\nu} + \frac{\beta'^{\,2}_\nu \beta''^{\,2}_\nu}{8\alpha'^{\,2}_\nu} + \frac{\beta'^{\,2}_\nu \epsilon_\nu}{4\alpha'^{\,2}_\nu} - \frac{\beta'^{\,2}_\nu}{8\alpha'_\nu} - \frac{\beta''^{\,2}_\nu}{8\alpha'_\nu} - \frac{\epsilon_\nu}{4\alpha'_\nu} - \frac{1}{8} - \frac{\epsilon}{4\alpha'_\nu}\Big(1 - \frac{\beta'^{\,2}_\nu}{\alpha'_\nu}\Big)\Bigg) n_\nu + \langle\psi_\nu|Q^2 U(Q)|\psi_\nu\rangle + \sum_{\bar{\nu}} \mathrm{Re}\langle\psi_\nu|Q^2 v_{\nu\bar{\nu}}(Q)|\psi_{\bar{\nu}}\rangle\Bigg\}. \quad (2.61)$$

The above terms make up the six element vector χ_ν:

$$\chi_\nu = \begin{bmatrix} \chi_{a_\nu} \\ \chi_{\gamma_\nu} \\ \chi_{\beta'_\nu} \\ \chi_{\beta''_\nu} \\ \chi_{\alpha'_\nu} \\ \chi_{\alpha''_\nu} \end{bmatrix} \quad (2.62)$$

corresponding to the ν^{th} bath wave packet. The matrix elements involving the system-bath interaction potential $v_{\nu\bar{\nu}}(Q)$ that appear in the elements of χ_ν are responsible for coupling bath wave packets belonging to different system states.

Iodine in a Krypton Lattice

With the goal of simulating the dynamics of a small guest molecule in a cryogenic host medium, we've developed several model systems on which to test FVB/GB theory. All systems resemble a chunk of krypton atoms doped with a centrally located iodine molecule, but range in size from 8 to 184 atoms. All calculations in this paper have been performed on I_2Kr_6, the smallest of our

models. Inspired by the work of Buchholz and co-workers,[42] we've established I_2Kr_{17} which consists of a shell of 17 krypton atoms arranged in a double icosahedron geometry around an iodine molecule, as well as I_2Kr_{18} , I_2Kr_{72}, I_2Kr_{182} which consist of the iodine dimer surrounded by one, two and three solvation layers respectively of krypton atoms initially arranged in an fcc lattice geometry. All systems are treated as finite molecular clusters; we make no use of periodic boundary conditions in our simulations. A detailed description of the construction and potential interactions within the model systems may be found in the online supplement to this paper. The essential points needed to describe the potentials governing I_2Kr_6 are that the total potential energy in either electronic state is expressed as a sum of atom-atom interactions and all pair potential are fit to a sum of Gaussian functions [43] to facilitate analytic evaluation of matrix elements of the bath and interaction potentials. Under electronic excitation, only the I_2 potential changes in the total potential energy function and we implement a "harmonic net" governed by harmonic interactions between the outer layer nearest neighbor krypton atoms to prevent loss of these atoms from the cluster.

Minimum Energy Configuration

To find the normal coordinates in the ground electronic state of I_2Kr_6, we first equilibrate the model. The relevant pair potentials during equilibration are the Gaussian fits to the X-state I_2, Kr-Kr and Xe-Kr potentials discussed in the supplementary material. Construction begins by placing the mid-point between the iodine atoms at the origin with the centers 1.5 angstroms from the origin along the z-axis. The krypton atoms are placed in the xy-plane in a hexagon geometry centered around the origin. The coordinate vector for each krypton atom has a

magnitude of 4.2 Å from the origin. This starting geometry has a total of 4500 cm^{-1} of energy in the atom-atom bonds, 3021 cm^{-1} of which is in the I_2 bond.

To equilibrate the model, we make use of a classical velocity-Verlet algorythm.[44] The kinetic energy of all atoms is initially zero—we do not assign initial velocities based a Boltzmann distribution. This choice preserves the symmetry of the complex. Using a fixed time-step of 0.1 fs, cooling simulations we run where after each time-step the velocity is multiplied by 0.9999. By slowly removing kinetic energy from the system in this way atomic rearrangement is allowed but in the end a stable minimum-energy configuration ,$r^{(0)}$, is obtained. After one nanosecond of cooling, the complex contained 1212 cm^{-1} of energy. This corresponds to a loss of 3288 cm^{-1} of energy during equilibration, mostly coming I_2 itself.

Given that the initial geometry of I_2Kr_6 had D_{6h} symmetry, and with the choice to assign zero velocities for the atoms in the complex, the relaxation procedure preserves the symmetry of the model as any rearrangement of the structure honors the full symmetry of the Hamiltonian. This feature of the equilibration routine allows for the separation of symmetric and non-totally symmetric normal modes of the model. Electronic excitation of the totally symmetric system coordinate, at least initially, only produces motion in the totally symmetric Franck-Condon active bath modes. Preserving the symmetry of the structure facilitates handling the dynamics of the smaller set of symmetric bath modes thereby decreasing the computational effort of the FVB/GB calculations.

After equilibration, we implement the harmonic net. All the krypton atoms in I_2Kr_6 are outer layer atoms, therefore every nearest-neighbor krypton interaction is replaced by a harmonic interaction by expanding the full Kr-Kr pair potential for

each interaction and truncating at second order. With symmetry of the structure, the interaction between any two krypton atoms is the same, and hence there is a single harmonic potential governing the motion between all nearest-neighbor krypton atoms in I_2Kr_6. To facilitate integration over matrix elements of the system-bath interaction potential that appear in the FVB/GB equations, the Kr-Kr harmonic interaction is fit to a sum of five Gaussian functions. These details are further discussed in the online supplement.

With the minimum energy configuration $r^{(0)}$ the normal coordinates in the ground electronic state of the model are found through the recipe described in section 2.2. In Fig. 1. we plot bath mode frequency vs. mode number, for the normal coordinates I_2Kr_6, in units of the system frequency. The frequency of the totally symmetric bath mode is marked with a red bar. In this work, we treat the dynamics of the totally symmetric system and bath modes by zeroing out the normal coordinates ξ of the non-totally symmetric bath modes. The the system coordinate has a frequency of 218.104 cm^{-1}, and the totally symmetric bath mode frequency is 27.394 cm^{-1} in the ground electronic state. Pictures of the structure with the these coordinates stretched are shown in Figs. (2.) and (3.) respectively. Although the normal coordinates of the 2D model are defined in the ground electronic state, the electronic excited potential is the one that governs the dynamics in this work. The transfer of nuclear probability amplitude into the excited electronic state is discussed below. Figure 4. shows this potential with the system and bath coordinates reduced by the appropriate ground state RMS widths.

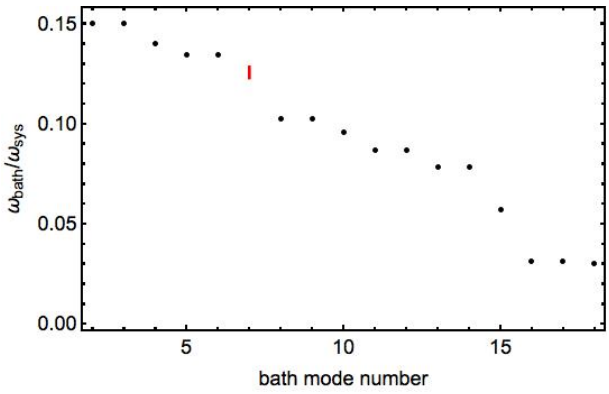

FIGURE 1. Plot of the bath mode frequencies in terms of the system frequency for I_2Kr_6. Bath mode seven, signified by the red bar is the only totally symmetric bath mode for this model.

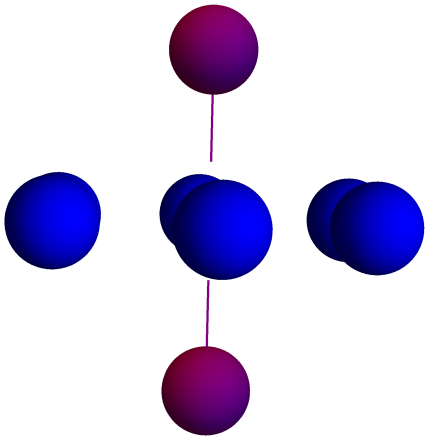

FIGURE 2. I_2Kr_6 with the system coordinate stretched and totally symmetric bath mode at its equilibrium position.

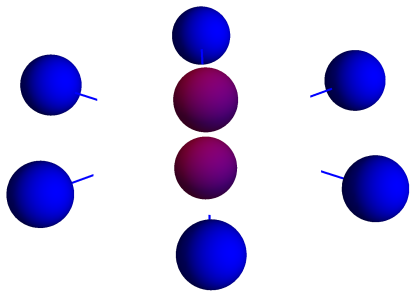

FIGURE 3. I_2Kr_6 with the totally symmetric bath coordinate stretched and the system coordinate at its equilibrium position.

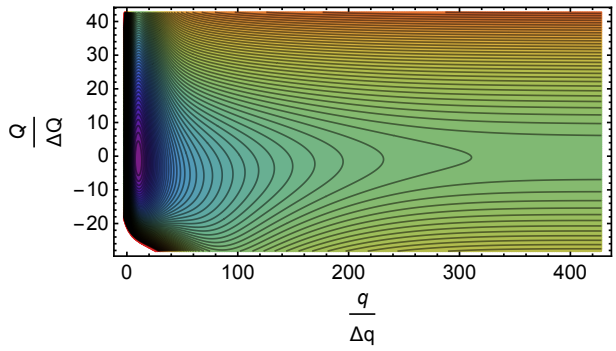

FIGURE 4. I_2Kr_6 excited electronic state potential that governs the dynamics of the FVB/GB parameter paths below. The system and bath coordinates have been reduced by the corresponding RMS width of the ground state wave packets to facilitate comparison with FVB/GB results.

Numerical Calculations

Interaction Picture

By diagonalizing the system Hamiltonian, the contribution of the ν^{th} system state to the FVB/GB equations is confined to the phase parameter γ_ν of the ν^{th} bath wave packet. To numerically stabilize the FVB/GB algorithm, we subtract off the ν^{th} system eigenenergy contribution to the time-derivative of the phase parameter for the ν^{th} bath wave packet. In order to effect this change in the FVB/GB equations, we re-parameterize each bath wave packet where the phase parameter γ_ν is replaced with $-\epsilon_\nu t+\delta\gamma_\nu$. The first term in the sum is a pure system contribution, and the latter is due to bath dynamics and system-bath interactions. Taking the time-derivative of the new expression for γ_ν, we find $\dot{\gamma}_\nu = -\epsilon_\nu + \delta\dot{\gamma}_\nu$.

From Eq. (2.7), the ν^{th} system state FVB/GB equations have the form $M_\nu \cdot \dot{\lambda}_\nu = \chi_\nu$, where

$$\dot{\lambda}_\nu = \begin{bmatrix} \dot{a}_\nu \\ \dot{\gamma}_\nu \\ \dot{\beta'}_\nu \\ \dot{\beta''}_\nu \\ \dot{\alpha''}_\nu \\ \dot{\alpha''}_\nu \end{bmatrix} = \begin{bmatrix} \dot{a}_\nu \\ -\epsilon_\nu + \delta\dot{\gamma}_\nu \\ \dot{\beta'}_\nu \\ \dot{\beta''}_\nu \\ \dot{\alpha''}_\nu \\ \dot{\alpha''}_\nu \end{bmatrix}, \tag{2.63}$$

given the definition of $\dot{\gamma}_\nu$ above. Making use of this equality, the FVB/GB equations for the ν^{th} system state become

$$M_\nu \cdot \begin{bmatrix} 0 \\ -\epsilon_\nu \\ 0 \\ 0 \\ 0 \\ 0 \end{bmatrix} + M_\nu \cdot \begin{bmatrix} \dot{a}_\nu \\ \delta\dot{\gamma}_\nu \\ \dot{\beta'}_\nu \\ \dot{\beta''}_\nu \\ \dot{\alpha''}_\nu \\ \dot{\alpha''}_\nu \end{bmatrix} = \chi_\nu, \tag{2.64}$$

or

$$M_\nu \cdot \begin{bmatrix} \dot{a}_\nu \\ \delta\dot{\gamma}_\nu \\ \dot{\beta'}_\nu \\ \dot{\beta''}_\nu \\ \dot{\alpha''}_\nu \\ \dot{\alpha''}_\nu \end{bmatrix} = \chi_\nu - M_\nu \cdot \begin{bmatrix} 0 \\ -\epsilon_\nu \\ 0 \\ 0 \\ 0 \\ 0 \end{bmatrix} \tag{2.65}$$

which results in cancellation of the system eigenenergy contributions to the terms χ_γ, $\chi_{\beta''}$ and $\chi_{\alpha''}$ in χ_ν. In effecting this transformation for each system state, the time-scale over which the bath parameters change is increased from $\approx$ 10 fs to $\approx$ 1.3 ps, by subtracting off system eigenenergies that give rise to frequency differences on the order of 3000 cm^{-1}.

Initial Conditions and Numerical Implementation

At time zero the state of the complex $|\Psi_0\rangle$ is defined in Eq. (2.27). Simulating short pulse absorption, we copy this state into the excited electronic

state of the model yielding

$$|\Psi_0\rangle = \hat{\mu}|g\rangle|0_g\rangle|\psi_{0_g}\rangle, \tag{2.66}$$

where $\hat{\mu} = |g\rangle\langle e| + |e\rangle\langle g|$. This is the initial condition of the complex at the beginning of the FVB/GB calculations. The probability amplitude or a_{ν_e} parameter for each bath wave packet is—aside from a normalization factor—specified by the Franck-Condon overlap. The real part of the width parameter α'_{ν_e} for every packet is assigned the value of the ground state bath wave packet shown in Eq. (2.28). All other bath wave packet parameters are set to zero initially.

To propagate the FVB/GB equations of motion shown in Eq. (2.7) we implement a fourth-order Runge-Kutta numerical integration routine.[45] The results presented in this paper were obtain using a 100 as time-step. To reduce the computational effort required, we propagate a smaller set of bath wave packet parameters by truncating the number of system states based on their initial population after copying the ground system wave function into the excited electronic state. In the excited electronic system potential defined in Section 2.2, there are 203 bound eigenstates. Keeping only 60 of these states ($\nu_e = 14 - 73$) results in an initial excited state wave packet with a population of 94.9% of the ground electronic state. This truncation reduces reduces the number of parameter time-derivatives in Eq. (2.7) by $\approx 70\%$. Implementation of this system eigenstate truncation manifests itself in the expectation value of the system coordinate q at time zero. Vertical excitation from the minimum of the X-state potential centered at $(0, 0)$ by definition to the Franck-Condon point in the B-state potential should lead to an excited state wave packet with the center ($q = 0, Q = 0$). Due to the system eigenstate truncation the initial conditions for the B-state wave packet are

$q/\Delta q = 0.396$ and $Q/\Delta Q = 0$, where Δq and ΔQ are the rms width of the system and bath wave packets respectively.

Further and easing the computational burden of these calculations, we truncate the interaction between bath wave packets corresponding with different system levels. This interaction overlap arises in χ as matrix elements of the interaction potential multiplied by various orders of the bath coordinate. The criterion for keeping the interaction between any two bath wave packets was set by evaluating the matrix elements of the interaction potential at a value of the bath coordinate yielding a large interaction energy. If the absolute value of any given matrix element expressed in terms of s^{-1} multiplied by 5 ps (a reasonable goal of propagation time for our calculation) had a value greater then or equal to one, then that matrix element was kept. Otherwise the matrix element is dropped and the interaction between the two contributing bath wave packets is ignored in the calculations. It is out of the scope of this paper, but a worthwhile check, to see whether or not this interaction truncation is reasonable by including more matrix elements of the interactions potential in the FVB/GB dynamics simulations.

In the past, the numerical instability of propagating parameterized states through the DFM variational principle has been well documented.[33] Heller and others have implemented the so called P-Z parameterization of the width parameter α in their Gaussian anstaz that significantly stabilizes the calculations.[46, 33, 29] As this round of FVB/GB calculations serves as the first test of the theory involving high amplitude motion in the largely anharmonic system coordinate with coupling to a thawed Gaussian bath, we maintain the form of the Gaussian ansatz shown in Eq. (2.26) and handle numerical instabilities as they arise. In particular, through out propagation certain 6×6 blocks along the diagonal of M became

nearly singular posing a problem for numerical inversion of the block as required by Eq. (2.7). To proceed with the propagation of the state we invoke a singular value decomposition[45] (SVD) routine that finds a pseudoinverse to the nearly singular 6×6 block. Under this routine the 60 6×6 blocks are diagonalized individually through an orthogonal transformation. If the ratios between the smaller and the largest eigenvalues for a given block are below a set threshold, then the inverse of the smaller eigenvalues are set to zero upon inverting the eigenvalue matrix for that block. This has the effect of freezing the eigenvectors of the singular value that was dropped for that time-step. If in the next time-step the ratio of eigenvalues was found to lie above the threshold, then the block is inverted as normal.

FVB/GB Results

Using a 100 as time-step, propagation of the FVB/GB parameter equations of motion was numerically stable for about 2.3 ps. As pointed out earlier in this chapter, the norm and energy of the initial state are strictly conserved under the DFM variational principle. During propagation, at approximately 700 fs, numerical error in the integration routine lead to norm non-conservation which in-turn produced energy non-conservation. After the onset of a change in the norm, the norm and energy values fluctuated for the remainder of the simulation. Because these two quantities are strictly conserved by the algorithm, the results indicate inaccurate integration of the equations of motion and improvement will require integration with a smaller time-step and possibly higher numerical precision in the calculations. The possibility exists that refinement of the integration will also facilitate inversion of the M matrix, and side step the need to implement a SVD routine when blocks of M become nearly singular.

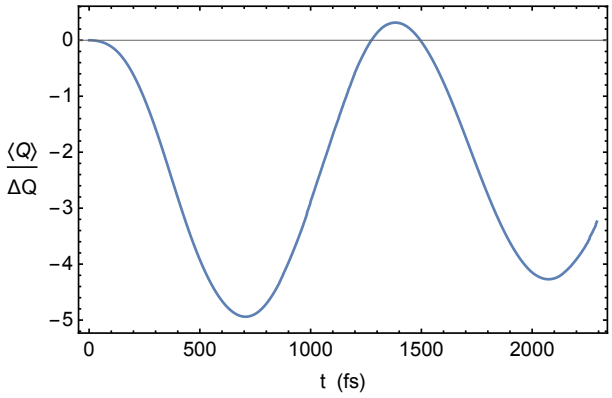

FIGURE 5. Expectation value of the bath coordinate over time. The bath coordinate value has been made dimensionless in this plot by division with the approximate RMS width of the ground state bath wave packet $\Delta Q = \sqrt{\frac{\hbar}{2\omega_b}}$.

Bath Wave Packet Parameter Trajectories and Observables

As shown in Fig. (5.), the average period of bath motion is approximately 1.4 picoseconds. A negative value of the bath coordinate corresponds to a compression of the krypton ring, and the ring begins slightly stretched upon transfer of the ground state wave packet to the excited state. All of the bath wave packets are assigned the same width and average positions initially, but as the system and bath interact the dynamics become markedly different depending on which system state a bath wave packet is assigned to. Figure (6.) shows the average position of bath wave packets $\nu_e = 14$ (red) - 47 (purple) over time clearly displaying the differing dynamics resulting from system and bath interaction. In particular, the expectation values for the bath wave packets associated with higher energy system states have a significantly larger range of motion underlining the stronger coupling between these packets and the system at these higher energies. Similar behavior is shown in the total and bath wave packet expectation values of the bath momentum operator.

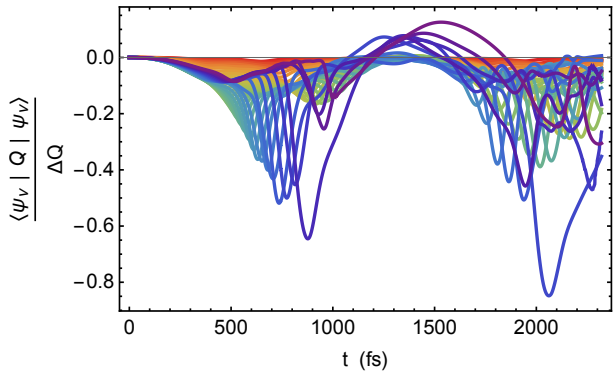

FIGURE 6. Expectation value of the coordinate for bath wave packets $\nu_e = 14$ (red) - 47 (purple) over time. The bath coordinate value has been made dimensionless in this plot by division with the approximate RMS width of the ground state bath wave packet $\Delta Q = \sqrt{\frac{\hbar}{2\omega_b}}$. The path of $\langle Q \rangle$ for each bath wave packet was calculated using Eq. (2.39).

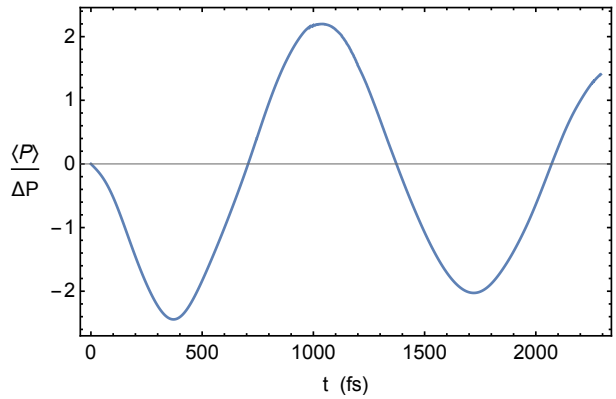

FIGURE 7. Plot of the expectation value of the bath momentum operator versus time. The bath momentum has been made dimensionless in this plot by division with the approximate RMS width of the ground state bath momentum wave packet $\Delta P = \sqrt{\frac{\hbar\omega_b}{2}}$.

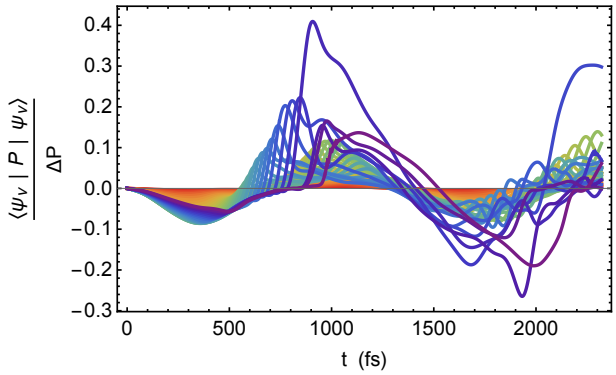

FIGURE 8. Expectation value of the momentum for bath wave packets $\nu_e = 14$ (red) - 47 (purple) over time. The bath momentum value for each packet has been made dimensionless in this plot by division with the approximate RMS width of the ground state bath momentum wave packet $\Delta P = \sqrt{\frac{\hbar\omega_b}{2}}$.

Entropy of the System

As a wave function based theory, FVB/GB can be used to calculate any quantity of interest. To gauge the effect of the system-bath interaction which, in general, mixes the initial tensor products of pure system and bath states, we calculate the reduced system entropy S_{sys}. The state of the universe is defined as a sum of tensor products of system times bath states in the electronic excited state. With the requirement that the nuclear state ket is normalized, the total state remains a pure state for all time. The system entropy is defined as,

$$S_{sys} = -\operatorname{Tr}_s(\sigma \ln \sigma) = -\sum_{\nu} \langle \nu | \sigma \ln \sigma | \nu \rangle, \tag{2.67}$$

where the reduced system density matrix σ is

$$\begin{aligned}\sigma &= \mathrm{Tr}_b(\rho) = \mathrm{Tr}_b(|\Psi\rangle\langle\Psi|) \\ &= \mathrm{Tr}_b\Big(\sum_{\nu,\bar{\nu}} |\nu\rangle|\psi_\nu\rangle\langle\psi_{\bar{\nu}}|\langle\bar{\nu}|\Big) \\ &= \sum_{\nu,\bar{\nu}} |\nu\rangle \int dQ \langle Q|\psi_\nu\rangle\langle\psi_{\bar{\nu}}|Q\rangle\langle\bar{\nu}| \\ &= \sum_{\nu,\bar{\nu}} |\nu\rangle\langle\psi_{\bar{\nu}}|\psi_\nu\rangle\langle\bar{\nu}|.\end{aligned} \tag{2.68}$$

To proceed, σ is diagonalized through an orthogonal transformation. Upon simplification, the resulting expression has the form

$$S_{sys} = -\sum_{i=1}^{L} \bar{\sigma}_i \ln \bar{\sigma}_i, \tag{2.69}$$

where $\bar{\sigma}_i$ are the elements of the eigenvalue matrix of σ and L is the total number system states in our calculations. The entropy of the system is zero for pure states and takes on larger positive values as mixing between the system and bath states occurs. The period of oscillation ($\approx$ 1.4 ps) in Fig. (9.) corresponds to the average period of bath motion; after one period of bath motion, S_{sys} decreases as both the system and bath visit the Franck-Condon region.

Absorption Spectra

FVB/GB

In developing FVB/GB theory, the main motivation lies in calculating spectroscopic signals from large molecular systems. As a first application of FVB/GB in this realm, we calculate the linear absorption spectrum of I_2Kr_6.

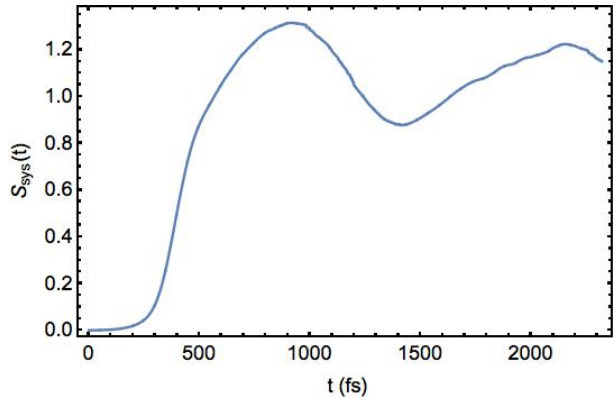

FIGURE 9. System entropy as defined in Eq. (2.67) for I_2Kr_6 over time calculated with FVB/GB.

Beginning with Heller's absorption expression [9]:

$$\Sigma(\omega) = \frac{1}{2\pi} \mathrm{Re} \int_0^\infty dt \exp\{i\omega t\} \langle \Psi_0 | \Psi(t) \rangle, \tag{2.70}$$

where $|\Psi_0\rangle = |0_g\rangle|\psi_{0_g}\rangle$ and $|\Psi(t)\rangle = \sum_{\nu_e} |\nu_e\rangle|\psi_{\nu_e}(t)\rangle$ under FVB/GB theory. Implementing these definitions yields

$$\Sigma(\omega) = \frac{1}{2\pi} \sum_{\nu_e} \langle 0_g | \nu_e \rangle \, \mathrm{Re} \int_0^\infty dt \exp\{i\omega t\} \langle \psi_{0_g} | \psi_{\nu_e}(t) \rangle. \tag{2.71}$$

The integral over time in the above expression, is in general limited by the propagation time of the FVB/GB calculations. In a large molecular cluster, with a multi-mode bath, contributions to the absorption kernel will be limited to short times as the overlap between the ground and excited state wave packets quickly falls off and likely never returns due to significant amplitude transfer to the bath degrees of freedom.[9] Given the one dimensional bath in I_2Kr_6 however, the excited state wave packet returns several times to the Franck-Condon region giving rise to long-time contributions to the absorption kernel. To ensure these contributions

vanish by the end of the FVB/GB propagation time, we introduce a cosine-squared window function with width parameter σ into the absorption expression. Further, to account for the zero point energy of the ground state in the transition frequency, we add to the laser frequency ω the zero point energy E_{0X} of the state $|\Psi_0\rangle$, and the final form of the absorption expression for use with FVB/GB results becomes

$$\Sigma(\omega) = \frac{1}{2\pi} \sum_{\nu_e} \langle 0_g | \nu_e \rangle \, \mathrm{Re} \int_0^{\sigma} dt \exp\Big\{ i(\omega + E_{0X})t \Big\} \cos^2\left(\frac{\pi t}{2\sigma}\right) \langle \psi_{0_g} | \psi_{\nu_e}(t) \rangle, \quad (2.72)$$

which is suitable for numerical integration. The resulting spectrum is shown in Fig. (10.). The sudden onset of the spectrum at ≈ 1400 cm^{-1} is due to the truncation of system eigenstates up to $\nu_e = 13$. Likewise, the abrupt step in the spectrum at 4800 cm^{-1} lies at the energy of $(\nu_e = 73) - E_{0_X}$, the difference between the last system state kept in our calculations and the zero point energy of the ground electronic state.

Given the propagation time (2320 fs) of the FVB/GB results, this spectrum has resolution down to ≈ 14.5 cm^{-1}. Clearly resolved are the initial fundamental peaks and two sets of sidebands spaced from the fundamental at the frequency of the bath of 26 cm^{-1} and 2$\times$ 26 cm^{-1} respectively. Distinguishing between fundamental and side band peaks becomes increasing difficult around 2500 cm $^{-1}$ as several resonances between the system and bath —beginning with a four to one resonance—begin to split the fundamental peak as the frequency spacing between system eigenstates decreases up the manifold.

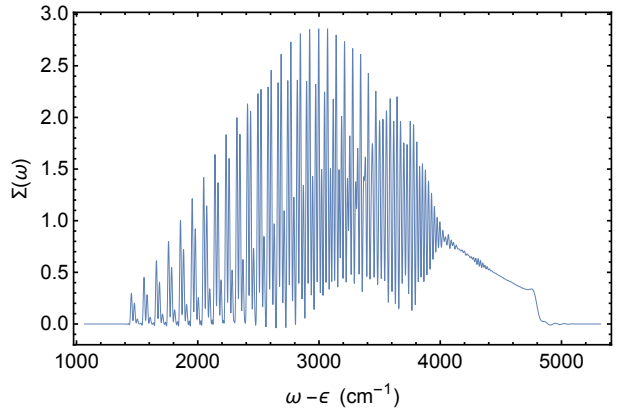

FIGURE 10. Absorption spectrum of I_2Kr_6 calculated using Eq. (2.72) and FVB/GB results.

Numerically Exact Calculation and Discussion

Having been reduced to two dimensions, calculating the numerically exact absorption spectrum of I_2Kr_6 using basis set methods is feasible. We begin by finding a rectangular area over which to represent the full two-dimensional potential by isolating the highest enclosed contour with an energy of 6287 cm^{-1}. This contour lies just below the dissociation channel present in the potential at a large positive q value and small negative Q value. The horizontal axis of this rectangle defines the range of system motion of interest; the vertical axis specifies the range of bath motion. The system and bath Hamiltonians are represented over the respective ranges in a uniformly-spaced discrete position grid using a spacing of $\approx$ 1% of the RMS width of the ground state bath wave packet in both directions. This spacing was chosen to accurately capture the minimum Debroglie wavelength in the region above the minimum of the potential of an eigenstate with an energy equal to the dissociation energy. Subsequent diagonalization of the two uncoupled Hamiltonians, yielded pure system and bath eigenenergies and their corresponding wave functions. The total Hamiltonian was represented in a the

tensor product basis, by first truncating the number of system and bath eigenstates by energy. Dropping all eigenstates whose energy is greater then 6600 cm^{-1} for both the system and the bath, we kept 355 system states and 238 bath states. Representation of the total Hamiltonian in a tensor product basis consisting of these states produced a dense matrix of dimensions 84490×84490 suitable for direct diagonalization.

To compare with the absorption spectrum calculated from FVB/GB results, we again begin with Eq. (2.70), but with exact eigenstates of the full Hamiltonian the absorption expression has the form

$$\Sigma(\omega) = \frac{1}{2\pi} \sum_{\theta} \langle \Phi_0 | \theta \rangle \langle \theta | \Phi_0 \rangle \, \mathrm{Re} \int_0^{\sigma} dt \exp \left\{ i(\omega - E_{\theta_B} + E_{0_X})t \right\} \cos^2 \left(\frac{\pi t}{2\sigma} \right), \quad (2.73)$$

where the basis set $|\theta\rangle$ obeys $H|\theta\rangle = E_\theta|\theta\rangle$, and E_{0_X} is the exact ground state zero point energy. For comparison purposes, we have introduced the same cosine-squared window function as in the FVB/GB spectrum, but in principle the exact absorption spectrum can be calculated with infinite resolution. The resulting integral can be evaluated analytically, yielding the simple result of Franck-Condon factors times a spectral peak centered at $\omega = E_{\theta_B}$:

$$\Sigma(\omega) = \frac{1}{4\pi} \sum_{\theta} \langle \Phi_0 | \theta \rangle \langle \theta | \Phi_0 \rangle \frac{\sin[(\omega - E_{\theta_B})\sigma]}{(\omega - E_{\theta_B})(1 - (\omega - E_{\theta_B})^2 (\frac{\sigma}{\pi})^2)}. \quad (2.74)$$

Figure (11.) shows the resulting exact absorption spectrum after summation over the eigenvectors $|\theta\rangle$. The agreement between the numerically exact spectrum and the spectrum calculated from FVB/GB is impressive. There are several thousand spectral lines in the absorption spectrum of I_2Kr_6, and with minimal effort FVB/GB captures many of them. For further emphasis of the agreement

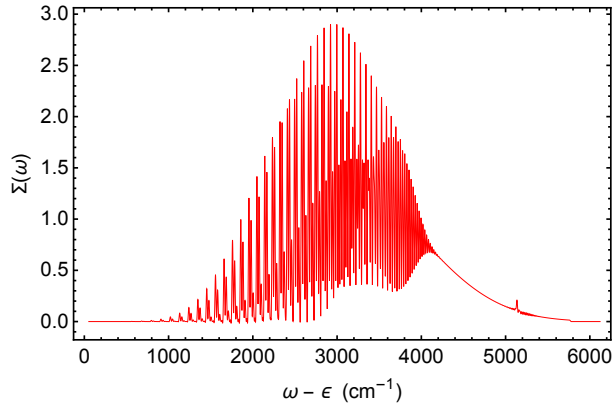

FIGURE 11. Absorption spectrum of I_2Kr_6 calculated using Eq. (2.74) and numerically exact Franck-Condon factors and eigenenergies.

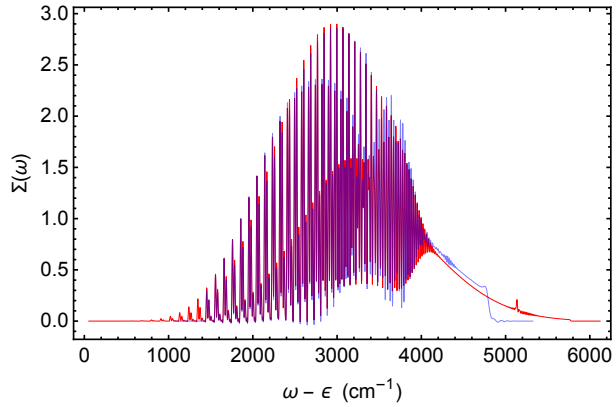

FIGURE 12. Overlay of absorption spectra for I_2Kr_6 calculated with Heller's absorption kernel using exact eigenstates (red) and FVB/GB results (blue). Agreement between the two spectra results in purple lines.

between the two spectra, Fig. (12.) shows the exact spectrum in red overlayed with the FVB/GB spectrum in light blue. Correspondence between the two results shows up as purple.

To understand the spectrum of I_2Kr_6, we focus on the numerically exact spectrum and make comparisons when needed to the FVB/GB result. In Fig. (11.) there are four clear vibrational progressions centered at 2800 cm^{-1} (FWHM = 1350 cm^{-1}), 2950 cm^{-1} (FWHM = 2000 cm^{-1}), 3100 cm^{-1} (FWHM = 800 cm^{-1} and 3600 cm^{-1} (FWHM = 650 cm^{-1}) respectively. The absorption spectrum itself has

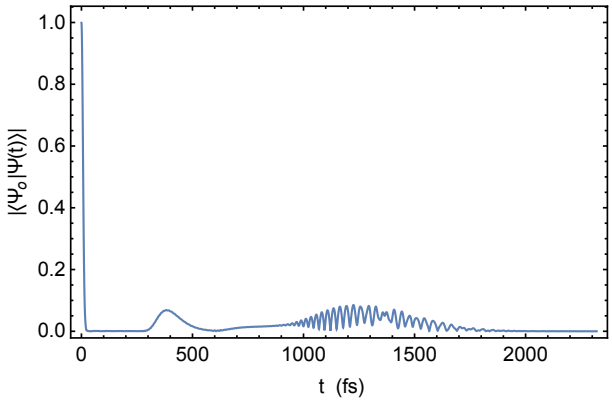

FIGURE 13. Absolute value of the exact autocorrelation function consisting of the time-dependent excited state wave packet overlapped with the stationary ground eigenstate.

a FWHM of 2100 cm^{-1}. All of these frequency bands and the spacing between the spectral peaks themselves correspond to a time scale that must be present in the time-dependent absorption kernel shown in Fig. (13.) that was used to calculate this spectrum.

Interpreting the absorption spectrum in a time-dependent manner, some of the initial dynamics that give rise to the features in the absorption spectrum are evident in the absorption kernel. The abrupt decrease in the autocorrelation function between 0 and 20 fs corresponds to the rapid loss of overlap between the ground and excited state wave packets. The HWHM of this peak is 8 fs, a FWHM of 16 fs corresponds to the width of the total absorption spectrum when converted to frequency units.

After the initial loss of overlap, the autocorrelation function has a zero value until part of the total wave packet returns to the Franck-Condon region. The first recurrence centered at 395 fs with FWHM = 122 fs corresponds to a component of the two-dimensional wave packet composed of primarily system eigenstates returning to the Frank-Condon point after an averaged system

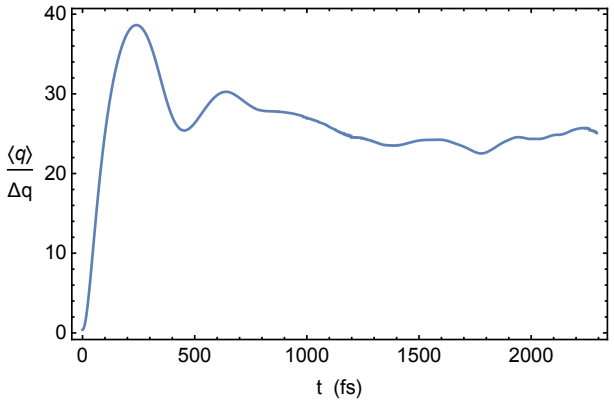

FIGURE 14. Expectation value of the system coordinate plotted in terms of the RMS width of the ground state wave function $\Delta q = \sqrt{\frac{\hbar}{2\omega_{sys_X}}}$.

vibrational period. As shown in Fig. (14.) however, most of the amplitude in the wave packet remains distant from the Franck-Condon point giving rise to a system coordinate expectation value much greater then zero, and a peak magnitude of the autocorrelation function of only 8% of the original overlap for this recurrence .

An analysis based on frequency differences between pure system eigenstates in the Franck-Condon region has shown that linear superpositions of system states $\nu_e + (\nu_e + 1)$, where ν_e ranges from 13 to 37 have vibrational periods within the FWHM of the first recurrence in the autocorrelation function. The peak of the recurrence at $\approx$ 395 fs likely corresponds to a wave packet composed of system states $\nu_e = 25 - 26$ with a vibrational period of 394 fs. It should be noted that the Franck-Condon point in the model lies close to $\nu_e = 34$, however the system eigenstate with the maximum Franck-Condon overlap is $\nu_e = 30$. This distribution of probability amplitude partially explains the peak position of the first recurrence.

Interpretation of the second broad recurrence in the absorption kernel ranging from 900 fs to 1900 fs demands analysis based on the dynamics of the full two

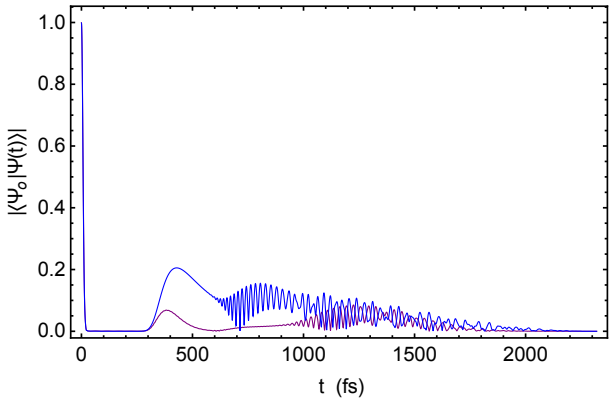

FIGURE 15. Comparison between absolute value of the exact absorption kernel calculated for the full model (purple) and system only (blue) in I_2Kr_6.

dimensional wave packet. This feature is striking compared with the first recurrence due to the presence of the red shifting oscillation that rides on top of the envelope in the recurrence. Also, the lack of a recurrence at two system periods (800 fs), combined with the observation that the second recurrence is peaked at three system periods (1.2 ps) suggests an interplay between the system and bath motion in the full two-dimensional wave packet. To determine how the presence of the bath effects the absorption kernel, we calculate the system only absorption kernel and overlay it with the kernel for the full model in Fig.(15.).

It is apparent from Fig. (15.) that the presence of the dynamical bath is responsible for the lack of a recurrence in the absorption kernel at 800 fs as the system only result has a peak at this time. In the two dimensional model, the wave packet undergoes its largest compression along the bath coordinate at 700 fs (see Fig. (5.)). This significant compression along the bath coordinate has the effect of pulling amplitude away from $q = Q = 0$ and killing any overlap between the ground and excited state wave packets at this time. Motion towards negative bath coordinate values prior to 700 fs also causes a decrease in the magnitude of the first recurrence peak when compared with the system only result. Conversely, after

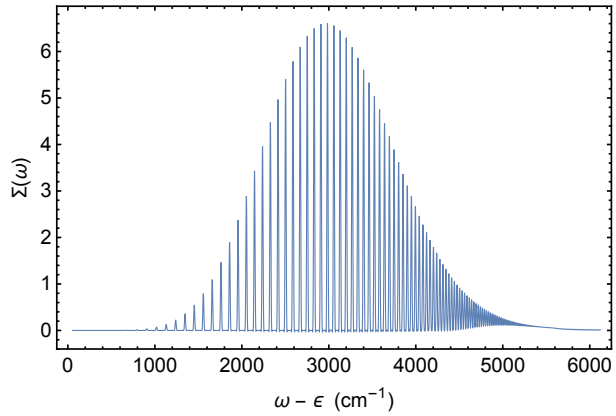

FIGURE 16. System only absorption spectrum for I_2Kr_6. In this calculation a window function of the form $\cos^4(\frac{\pi t}{2\sigma})$ was used with $\sigma = \frac{\pi\sigma_{FVB/GB}}{4\cos^{-1}(2^{(-\frac{1}{4})})}$. This change was implemented over the $\cos^2(\frac{\pi t}{2\sigma})$ window function used in the other spectra to account for the discontinuity in the second derivative of this function. Without the presence of the bath, the absorption spectrum is a smooth Franck-Condon progression with peaks at $\omega = \epsilon_{\nu_e}$.

700 fs, the wave packet turns around and heads towards positive Q values which accounts for the gradual increase in the magnitude of the second recurrence until its peak at 1.2 ps corresponding to three system periods which is also 200 fs short of one full bath period.

This explanation provides reasons for the form of the broad envelope which makes up the second recurrence, but the oscillation has yet to be interpreted. Since the oscillation is present in both the system only and total absorption kernel, the strong indication is that it is due to coherent superpositions of system eigenstates within the total wave packet. It is the presence of this oscillation in the system only absorption kernel along with the first recurrence that gives rise to the fringe structure in the system-only absorption spectrum shown in Fig. (16.). More quantitatively, the period of oscillation agrees between both kernel calculations despite the redshift from 15 fs to 29 fs by the end of the band. We attribute the redshift to the growing influence of system eigenstates with longer vibrational

periods reaching the Franck-Condon point during the lifetime of the band. This has been qualitatively confirmed by system wave packet movies. Interestingly, comparing the phase of the oscillation between the two kernels reveals that these features are precisely anti-phased. The source of this anti-phasing is due to the presence of the bath, but work towards a more thorough understanding for this feature remains to be done.

Concluding Remarks

This work presents the first application of our mixed quantum/semiclassical wave function based theory in the calculation of linear absorption of a small molecule isolated in a cryogenic medium. Building on previous works,[36, 40] a normal mode decomposition is utilized to separate a system from the surrounding bath; the system dynamics are handled with conventional basis set methods and the bath degrees of freedom are subject to a thawed Gaussian ansatz.[31] Isolation of the time-derivative of the parametrized state is accomplished through the use of a time-dependent variational method[32] in conjunction with a numerical integration routine.

The linear absorption spectrum for I_2Kr_6 is calculated both from FVB/GB results and rigorously using Heller's absorption expression.[7] Strong agreement between the spectra calculated at different levels of treatment was found down to 15 $cm^{-}1$ of resolution despite the presence of several thousand absorption lines displaying complicated features. A time-dependent explanation for some of the absorption features was offered through scrutiny of the time-dependent absorption kernel. Further interpretation of the absorption spectra will require an investigation

into the several Fermi-resonances between the system and bath in I_2Kr_6 that give rise to splitting about fundamental peaks and interesting peak-intensity ratios.

Future prospects for this work lie in several directions. We have developed the larger model systems I_2Kr_{17}, I_2Kr_{18}, I_2Kr_{72} and I_2Kr_{182} which, upon increasing size, more accurately represent iodine in an extended medium of krypton atoms. Much remains to be done with these model systems including initial FVB/GB dynamical simulations. As the size of the clusters increase, the effect of the boundary and energy dissipation into the bath leading possibly to permanet loss of overlap between ground and excited wave packets will be interesting areas to explore.

Bridge

The calculation of several ultrafast spectroscopic signals from condensed phased molecular systems is the ultimate goal in developing FVB/GB. Progress in this direction will require a perturbative formulation of FVB/GB where a separate sets of bath wave packet parameters parametrize each order-in-the-field portion in the perturbative expansion of the state. Aside from the requirement of propagating several new sets of parameters, this approach will allow the analytic isolation of the desired signal expression sidestepping the need to maintain all orders of the field in the state and subtracting off the many unwanted contributions in the numerical calculations.

There are several intriguing experimental studies where the application of perturbative FVB/GB can serve to further elucidate the information content of signals. Simulating four-wave mixing, time-resolved coherent anti-Stokes Raman scattering and short pulse absorption experiments is of particular interest.[2, 3, 17, 19]. In the following two chapters we develop the theory for

transient absorption and femtosecond stimulated Raman spectroscopy detailing the mechanisms of these measurements, and providing a clear path along which these theoretical works maybe be used in conjunction with FVB/GB to provide input on often information-rich experimental data.

CHAPTER III

ULTRAFAST TRANSIENT ABSORPTION REVISITED: PHASE-FLIPS, SPECTRAL FINGERS AND OTHER DYNAMICAL FEATURES.

This work was previously published in the Journal of Chemical Physics in 2016. It was initiated by Jeffrey Cina, Jeff Cina derived the expression in the paper and performed all theoretical calculations. Philip Kovac checked the analytic results and performed the sign of second derivative calculations on the data sets for PC577 and methylene Blue provided graciously by Chanelle Jumper, Jacob Dean and Greg Scholes. Jeffrey A. Cina was the principle investigator for this work.

Introduction

Broadband femtosecond transient-absorption spectroscopy provides a way to detect vibrational wave packets in the electronic ground and excited states of a molecule as a function of probed wavelength.[8, 9, 10, 11, 12, 13] These wave packets represent the sometimes complicated, multidimensional time evolution of superpositions of vibrational states launched in the Franck-Condon region of an excited state or near the global minimum of the electronic ground state by an impulsive pump laser pulse. While the interpretation of transient-absorption signals has been widely discussed, and many of their features rationalized in physical terms, some aspects of the molecular-level origin and information content of recent high-sensitivity transient-absorption measurements on complex biological systems are in need of further elucidation. In particular, while phase-changes of the coherent oscillations between the blue and red sides of a probe wavelength

coinciding with either the absorption or fluorescence maximum have been observed in a number of systems and explained qualitatively, a more precise physical description and a more rigorous analysis should aid the thorough interpretation of transient-absorption data. Here, we report on a theoretical investigation of this and related phenomena together with simulations of broadband pump/spectrally-resolved-probe signals based on recently reported transient-absorption data for a photosynthetic light-harvesting complex. [1]

In broadband transient-absorption experiments, the pump and probe laser pulses often have identical durations, $\sim$10 fs, and power spectra; it is also not uncommon for the probe pulse to have greater bandwdith than the pump. Ideally, the pulse spectra amply cover the absorption spectrum of the system being studied. The pump-induced change in probe transmission as a function of probed frequency and pump-probe inter-pulse delay is the detected quantity. It is dominated by picosecond and nanosecond decay components, which reveal the timescales of processes like electron transfer, energy transfer, or radiative decay. When those exponential amplitude changes are subtracted from sufficiently high-quality data, multi-component sinusoidal oscillations in the signal amplitude as a function of pump-probe delay are easily seen, [47, 48, 49] even from systems with weak electronic-vibrational coupling. For example, a recent study of a photosynthetic light-harvesting protein coauthored by one of us distinguished several vibrational frequencies in the range 190-810 cm^{-1}. [1] Analysis of the vibrational wave-packet dynamics showed that—due to the brevity of the pump pulse relative to the periods of the relevant Franck-Condon-active modes and the absence of significant nuclear-coordinate dependence of the electronic transition dipole moment—the oscillations in this system were dominated by superpositions of multiple levels involving eight

vibrational modes in the excited electronic state. Whereas oftentimes experiments also produce coherent vibrational motion on the ground electronic state, [8, 50, 51] excitation with pulses whose spectral width exceeds the entire absorption spectrum generates only excited-state wave packets. [11, 52]

The wave packet executes multi-dimensional oscillatory motion about the minimum of a multi-dimensional potential-energy surface. Based on the evolving difference potential between the ground- and excited-state surfaces, the spatial distribution of the wave packet as a function of pump-probe delay is manifested in the transient-absorption spectrum, resolved by λ_{probe}. [53] The difference potential at the minimum of the excited-state potential roughly equals the peak frequency of steady-state fluorescence, while that at the minimum of the ground-state equals the peak absorption frequency. What is striking is a universal phase-flip in the coherent oscillations. For instance, although a nuclear wave packet's trajectory in the excited state need not pass directly through the configuration of minimal potential energy, the oscillatory portion of the transient-absorption signal resulting from stimulated emission (SE) nonetheless exhibits a 180-degree change in phase from one side to the other of the corresponding electronic transition frequency. This behavior is illustrated with the SE-dominated transient-absorption data from PC577 depicted in Fig. 17..

The multi-component oscillations in Fig. 17. clearly decrease in amplitude and abruptly change phase around $\lambda_{probe} = 640$ nm, which corresponds to the maximum of the fluorescence spectrum. That feature provides evidence that the source wave packet is propagating in the excited electronic state. Similar behavior was seen some time ago in simulations by Mukamel and coworkers. [13, 54, 55] The node in the PC577 spectrum further shows that the vibrational wave packets

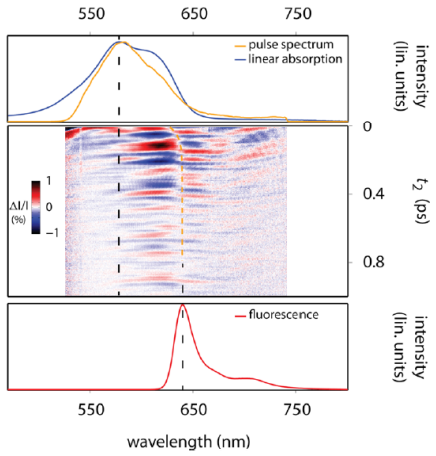

FIGURE 17. Steady-state and time-resolved spectral data on PC577 cryptophyte antenna. [1] Top panel shows absorption spectrum, peaking at 577 nm. Middle panel displays spectral oscillations in transient-transmission spectrum during first picosecond of probe delay, after subtraction of a decaying background. Quantum beats visible here were attributed to small-amplitude vibrational motion in singly excited electronic states within a collection of weakly interacting phycocyanobilin and dihydrobiliverdin chromophores. Note signficant degree of antiphasing between vibrational quantum beats on opposite sides of Stokes-shifting peak fluorescence frequency indicated by dashed orange curve tracing null-line in background-subtracted spectrum. Bottom shows steady-state fluorescence spectrum, peaking at 640 nm. Reprinted with permission from S. D. McClure, D. B. Turner, P. C. Arpin, T. Mirkovic, and G. D. Scholes, "Coherent oscillations in the PC577 cryptophyte antenna occur in the excited electronic state," J. Phys. Chem. B **118**, 1296-1308 (2014). Copyright (2014) American Chemical Society.

are carried along by a dynamic Stokes shift, which globally lowers the ground-to-excited electronic energy gap on a timescale longer than the periods of the observed vibrational beats. Careful analysis of the position and dynamic shift of this node as a function of time will reveal microscopic details of how the bath interacts with intramolecular reorganization.

Theory

Molecular Hamiltonian

We consider a molecular Hamiltonian comprising two electronic levels,

$$H = |g\rangle H_g \langle g| + |e\rangle H_e \langle e| \,, \tag{3.1}$$

each with its own nuclear Hamiltonian. In a light-harvesting complex, the electronic excited state of a given chromophore may be similar in energy and coupled by energy transfer to excited states of other chromophores. In the open structure of the PC577 complex, however, the coupling of the two higher-energy, dihydrobiliverdin (DBV) pigments to each other and to the six phycocyanobilins (PCB) is sufficiently weak that energy transfer proceeds at a rate slower than the frequencies of several vibrational modes whose equilibrium displacements are shifted slightly upon electronic excitation of the chromophore.[1] For this reason, we shall initially neglect excitation transfer from the e-state, and later treat it phenomenologically as part of a slow decay of the e-state amplitude. Our main interest here is with the effects of electronic-vibrational coupling, rather than electronic excitation-transfer coupling, on transient-transmission signals.

The molecule is subjected to a pump pulse and a delayed probe, both resonant with the $e \leftarrow g$ transition and having temporal envelopes of the same form. Hence $H(t) = H + v(t)$, with $v(t) = -\hat{m}[E_u(t) + E_r(t)]$, where

$$\hat{m} = m(|e\rangle\langle g| + |g\rangle\langle e|) \,, \tag{3.2}$$

$$E_u(t) = E_u f(t) \cos[\Omega t + \varphi_u] \,, \tag{3.3}$$

and

$$E_r(t) = E_r f(t - t_d) \cos[\Omega(t - t_d) + \varphi_r] \,. \tag{3.4}$$

The subscript u identifies parameters associated with the pump pulse, and r identifies those associated with the probe. t_d specifies the variable delay between these two ultrashort pulses. The absolute optical phases φ_u and φ_r are not under experimental control in an ordinary transient-absorption measurement. Nor, typically, is the inter-pulse shift $\varphi_r - \varphi_u$.

The spectrally resolved transient-transmission signal is the increase in the transmission of the probe pulse, within a certain narrow range of frequencies, due to the interaction of the chromophore with the pump pulse. [1] For an individual chromophore, this quantity can be written

$$\Delta U(\bar{\omega}) = \frac{1}{2\pi} \int \mathrm{d}^3 R \; E'_r(\mathbf{R}, t) \, \mathcal{E}_{u^2 r}(\mathbf{R}, t) \,, \tag{3.5}$$

where $E'_r(\mathbf{R}, t)$ is the portion of the probe pulse with frequency components in the narrow range, $\bar{\omega} - \delta\omega/2 < |\omega| < \bar{\omega} + \delta\omega/2$. [2] This change in electromagnetic energy of the transmitted probe results from interference between E'_r and the electric field radiated by the probe-induced molecular dipole (located at the spatial origin) that has been influenced by the presence of the pump:

$$\mathcal{E}_{u^2 r}(\mathbf{R}, t) = -\frac{1}{c^2 R} \ddot{m}_{u^2 r}(t - R/c) \,. \tag{3.6}$$

[1] The quantity measured and plotted in Ref.[1] is transient transmission, rather than transient absorption, which would differ from it in sign. We will refer to the calulated signals by either of these terms, without distinguishing between them, but will remain consistent in always referencing them to Eq. (3.5).

[2] We regard the fixed molecular location as the spatial origin. For a plane-wave probe pulse propagating in the z-direction then, $E_r(\mathbf{R}, t) = E_r(t - Z/c)$.

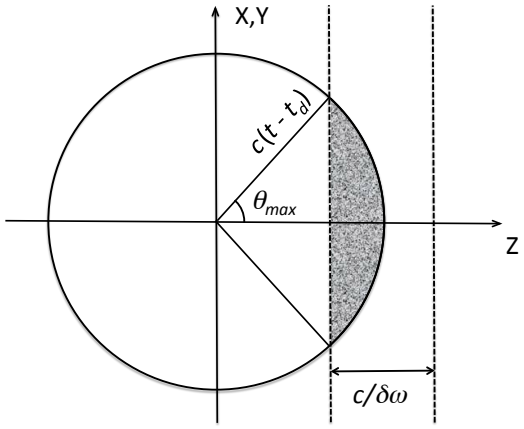

FIGURE 18. Spatial overlap of transient-absorption signal and filtered-probe fields. Signal field is contained within sphere of radius $c(t - t_d)$ emanating from source dipole at the origin. Filtered probe resides in slab of thickness $c/\delta\omega$ between two vertical dashed planes, where $\delta\omega$ is the spectral resolution of the measurement. Electromagnetic interference between the two occurs in shaded lozenge of opening half-angle $\theta_{max} \simeq 1/\sqrt{\delta\omega(t - t_d)}$.

The time t is assumed to be large enough that the spectrally filtered probe lies entirely in the far-field region of the radiating dipole. [56] This condition is in fact ensured by $(t - t_d)\delta\omega > 1$, which asserts that the filtered probe, itself many wavelengths in spatial extent, is well past the source dipole at time t. The quantity m_{u^2r} in Eq. (3.6) is the portion of the molecular induced electric dipole moment proportional to $E_u^2 E_r$; like the conventional derivation, that given here will be perturbative in the incident fields. The spatial integration in Eq. (3.5) extends over the disk-shaped region of overlap between the two fields, as pictured in Fig. 18.. This spatial integral over the overlapping fields will next be combined with quantum mechanical formulas for the various contributions to m_{u^2r} to obtain from this basic electrodynamical equation a working expression for the transient-transmission signal in terms of the underlying molecular dynamics (see Secs. 3.2 through 3.2 and Appendix B.2).

Transient-transmission dipole

Contributions to the transient-transmission dipole m_{u^2r} could arise from six different matrix elements of the dipole-moment operator (and their complex conjugates):

$$\underset{\text{GSB}}{\langle 0|\hat{m}|\uparrow_u\downarrow_u\uparrow_r\rangle} \quad \underset{\text{GSB}'}{\langle 0|\hat{m}|\uparrow_r\downarrow_u\uparrow_u\rangle} \quad \underset{e^{-2i\varphi_u}}{\langle 0|\hat{m}|\uparrow_u\downarrow_r\uparrow_u\rangle} \tag{3.7}$$

$$\underset{\text{SE}}{\langle\uparrow_u|\hat{m}|\uparrow_u\downarrow_r\rangle} \quad \underset{\text{SE}'}{\langle\uparrow_r|\hat{m}|\uparrow_u\downarrow_u\rangle} \quad \underset{e^{2i\varphi_u}}{\langle\uparrow_u|\hat{m}|\uparrow_r\downarrow_u\rangle} \tag{3.8}$$

An upward (downward) arrow signifies an absorptive (emissive) transition, and its subscript identifies the responsible pulse. The sequence of pulse actions proceeds from left to right within each ket or bra, but there is no specified order of action between pulses appearing in the bra and those appearing in the ket.

The first element in Eq. (3.7) accounts for the effect of ground-state bleaching by the pump pulse on the probe transmission. The second element is similar from the molecule's point of view, as the probe-induced transition and one pump transition have simply interchanged roles. The phase-factor $\exp\{-2i\varphi_u\}$ carried by the third element in (3.7) is uncontrolled, and the contribution of this term averages to zero over the many laser shots required to accumulate a transient-transmission signal. In Eq. (3.8), the first element governs stimulated emission, while the second is essentially similar, but with one pump interaction and the probe interaction switching roles. The third element in (3.8) is again proportional to a nonsurviving phase-factor. [3]

From their forms, which require that the probe pulse act after the pump, it can be seen that the GSB and SE contributions to the induced u^2r-dipole all vanish

[3]The remaining elements in Eqs. (3.7) and (3.8) carry typically-uncontrolled optical phase factors $\exp\{\pm i\varphi_r\}$, but each of these will be cancelled by its complex conjugate in the final signal expression.

for negative values of t_d larger in magnitude than the pulse duration. In GSB$'$, on the other hand, the probe must act before the pump, so this element vanishes beyond small *positive* delay times. SE$'$ does not specify the order of pulse action, so the matrix element itself does not necessarily vanish for sizable positive t_d; we will later discuss the delay dependence of the resulting signal contribution.

Formulating transient absorption spectroscopy in terms of perturbative contributions to the time-dependent molecular state in Hilbert space avoids the distinctions made in a Liouville-space treatment between time-ordered diagrams which differ only in the relative chronology of bra-side and ket-side events. The reason being that in a Hilbert-space description those "different" orderings are all naturally and automatically superposed. The surviving dipole matrix elements in Eqs. (3.7) and (3.8) can be considered as formulaic alternatives to 'time-circuit diagrams' for the sequence of 'forward' and 'backward' time-evolution processes contributing to a given nonlinear optical signal.[4, 57]

Bras and kets

Pulse propagators

In order to calculate the transient-transmission signal field (3.6), we need perturbative expressions for the zeroth-, first-, second-, and third-order bras and kets appearing in the four optically phase-stable dipole elements of Eqs. (3.7) and (3.8). Long before either pulse arrives, the molecule is in the electronic ground state and an arbitrary vibrational eigenstate $|\psi_0\rangle$ of H_g with energy ϵ_0 (in angular frequency units, as we set $\hbar = 1$). A straightforward analysis yields

$$|0\rangle = |g\rangle|\psi_0\rangle e^{-i\epsilon_0 t} \tag{3.9}$$

for the zeroth-order ket. The first-order kets are

$$|\uparrow_u\rangle = |e\rangle\, iF_u e^{-i\varphi_u} e^{-iH_e t} p^{(eg)}(t;\tau)|\psi_0\rangle \tag{3.10}$$

and

$$|\uparrow_r\rangle = |e\rangle\, iF_r e^{-i\varphi_r} e^{-iH_e(t-t_d)} p^{(eg)}(t-t_d;\tau)|\psi_0\rangle e^{-i\epsilon_0 t_d}\,, \tag{3.11}$$

where $F_{u(r)} = mE_{u(r)}\sigma/2$, with a pulse-duration parameter σ, and

$$p^{(eg)}(t;\tau) = \int_{-\infty}^{t} \frac{\mathrm{d}\tau}{\sigma}\, f(\tau) e^{-i\Omega\tau} e^{iH_e\tau} e^{-iH_g\tau}\,, \tag{3.12}$$

is a *reduced pulse propagator*. Our definition of the reduced pulse propagator incorporates a rotating-wave approximation. For the relevant second-order kets, we find

$$|\uparrow_u\downarrow_u\rangle = -|g\rangle\, F_u^2 e^{-iH_g t} p^{(ge)}(t;\tau) p^{(eg)}(\tau;\bar{\tau})|\psi_0\rangle \tag{3.13}$$

and

$$|\uparrow_u\downarrow_r\rangle = -|g\rangle\, F_u F_r e^{i\varphi_r - i\varphi_u} e^{-iH_g(t-t_d)} p^{(ge)}(t-t_d;\tau) e^{-iH_e t_d} p^{(eg)}(\tau+t_d;\bar{\tau})|\psi_0\rangle\,, \tag{3.14}$$

with $p^{(ge)} = (p^{(eg)})^\dagger$. The contributing third-order kets are found to be

$$|\uparrow_u\downarrow_u\uparrow_r\rangle = -|e\rangle\, iF_u^2 F_r e^{-i\varphi_r} e^{-iH_e(t-t_d)} p^{(eg)}(t-t_d;\tau) e^{-iH_g t_d} p^{(ge)}(\tau+t_d;\bar{\tau}) p^{(eg)}(\bar{\tau};\bar{\bar{\tau}})|\psi_0\rangle\,, \tag{3.15}$$

and

$$|\uparrow_r\downarrow_u\uparrow_u\rangle = -|e\rangle\, iF_u^2 F_r e^{-i\varphi_r} e^{-iH_e t} p^{(eg)}(t;\tau) p^{(ge)}(\tau;\bar{\tau}) e^{iH_e t_d} p^{(eg)}(\bar{\tau}-t_d;\bar{\bar{\tau}})|\psi_0\rangle e^{-i\epsilon_0 t_d}\,. \tag{3.16}$$

It is to be appreciated that the second- and third-order kets involve *nested* pulse propagators, for which the upper integration limit of an earlier-acting propagator depends on the integration variable of a later-acting one, as the notation indicates. These zeroth- first-, second-, and third-order state-kets are combined in Appendix A to give the sought-after matrix elements (3.7) and (3.8) of the electric dipole-moment operator.

Incident pulse envelopes

Any convenient form can be adopted for the envelope function of the incident pump and probe pulses. We use a simple shape that strikes a compromise between compactness and realism, $f(t) = g(t/\sigma)P(t/\sigma)$, with $g(x) = \cos(\pi x/2)$ and a pedestal function,

$$P(x) = \theta(x+1)\theta(x-1) = \begin{cases} 1 & -1 < x < 1 \\ \\ 0 & \text{otherwise} \end{cases} . \tag{3.17}$$

For this envelope, the parameter σ corresponds to the full-width at half-maximum of the incident intensity.

In the calculations that follow, the pulse-duration parameter will be regarded as having a value short enough that nuclear motion can be ignored in evaluating the reduced pulse propagators for the unfiltered pump and probe. [58][4] It is therefore possible to neglect the noncommutativity of the small quantities τH_e

[4]This approximation introduces an element of inconsistency to our treatment, as we shall later take account of the variation in amplitude of the spectrally filtered probe pulse across the absorption band: were the incident pulse truly vibrationally abrupt, its spectral amplitude would be flat across the absorption spectrum.

and τH_g in Eq. (3.12).[5] As in the experiments of Ref. 7, the pulses are assumed to be electronically resonant with $e \leftarrow g$. Even under the simplifying conditions of brevity and resonance with the single electronic transition, it is important to account properly for pulse turn-on and temporal overlap between the pump and probe pulses at small t_d.

Transient-transmission signals require a variety of nested double and triple pulse propagators for a range of pump-probe delays. Deriving analytical expressions for the required multiple propagators appropriate to the chosen pulse-shape is helpful because it sidesteps the burdensome task of numerically evaluating several different multiple integrals for every combination of t_d and probed wavelength. For a resonant single-pulse propagator (3.12), we find

$$p^{(eg)}(t;\tau) = \theta\left(\frac{t}{\sigma}+1\right)\left[G(t/\sigma)-G(-1)\right] - \theta\left(\frac{t}{\sigma}-1\right)\left[G(t/\sigma)-G(1)\right], \qquad (3.18)$$

with the indefinite integral $G(x) = \int dx\, g(x)$. It turns out that $p^{(eg)}(t;\tau) = p^{(ge)}(t;\tau) \equiv p(t)$ is a *real* number due to the condition of electronic resonance. It takes the form of a smoothed-out step function, as illustrated in the top panel of Fig. 19. for the case of a truncated-cosine pulse envelope, for which $G(x) = (2/\pi)\sin(\pi x/2)$.

While formulas for the required second- and third-order reduced pulse propagators can be worked out by hand for the truncated-cosine and other simple pulse envelopes, it is actually easier, and serves our purpose just as well, to generate those lengthy formulas by symbolic integration. Our symbolically

[5]The quantity τH_e includes τ times the bare electronic transition energy, which need not be small for τ in the range of the incident pulse duration; but this term is a constant and therefore commutes with τH_g.

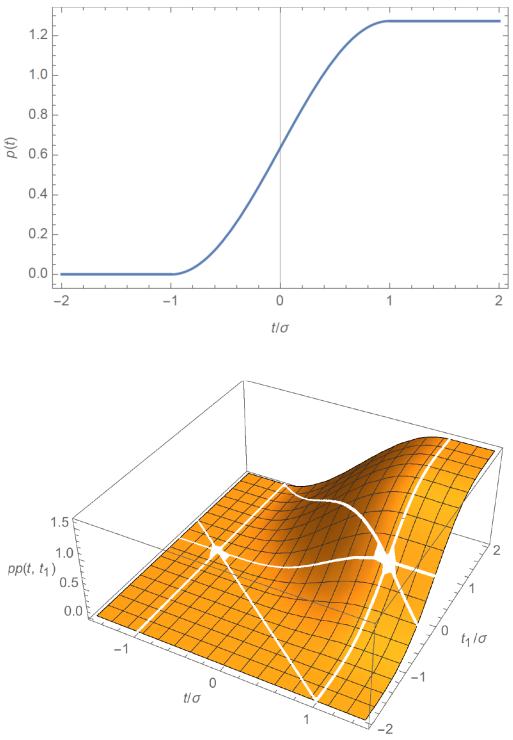

FIGURE 19. Top panel graphs single pulse propagator versus time, and bottom shows double pulse propagator as a function of both time arguments. Both plots are for a vibrationally abrupt, electronically resonant pulse with a truncated-cosine envelope. White lines on the plotted surfaces in bottom panel and in Fig. 20. are artifacts of the plotting program.

generated results for the double,

$$pp(t,\tau_1) \equiv p^{(ge)}(t;\tau)p^{(eg)}(\tau+\tau_1;\bar{\tau})\,, \tag{3.19}$$

and triple,

$$ppp(t,\tau_1,\tau_2) \equiv p^{(eg)}(t;\tau)p^{(ge)}(\tau+\tau_1;\bar{\tau})p^{(eg)}(\bar{\tau}+\tau_2;\bar{\bar{\tau}})\,, \tag{3.20}$$

pulse propagators were spot-checked by numerical integration. The temporal forms of $pp(t,\tau_1)$ and $ppp(t,\tau_1,\tau_2)$ are shown in the bottom panel of Fig. 19. and in Fig. 20., respectively. As with the single-pulse propagator, it is seen that under the present assumption of vibrationally abrupt incident pulses, the double-, and triple-pulse propagators appear as rounded step functions in all their time arguments, smoothed out over the nonzero pulse duration. Within the framework being developed in this work, these important functions control the onset and turn-off of the several contributions to the broadband transient-transmission signal (see next paragraph) and obviate the need to convolve a nonlinear optical response function over multiple pulse envelopes. A recent formal analysis[59] made use of quantities similar to our pulse propagators, providing definitions for the special case of a sequence of temporally nonoverlapping, nonzero-duration laser pulses.

Because the reduced pulse propagators are numbers, rather than nuclear operators, at the present level of approximation, they commute with the nuclear free-evolution operators appearing in Eqs. (B.1) - (B.4). This simplification leads to the following working expressions for the induced dipole moments contributing to the transient-transmission signal:

$$m_{GSB} = -imF_u^2F_r e^{-i\varphi_r}e^{i\epsilon_0(t-t_d)}\left\langle\psi_0|e^{-iH_e(t-t_d)}|\psi_0\right\rangle ppp(t-t_d,t_d,0) + \text{c.c.} \tag{3.21}$$

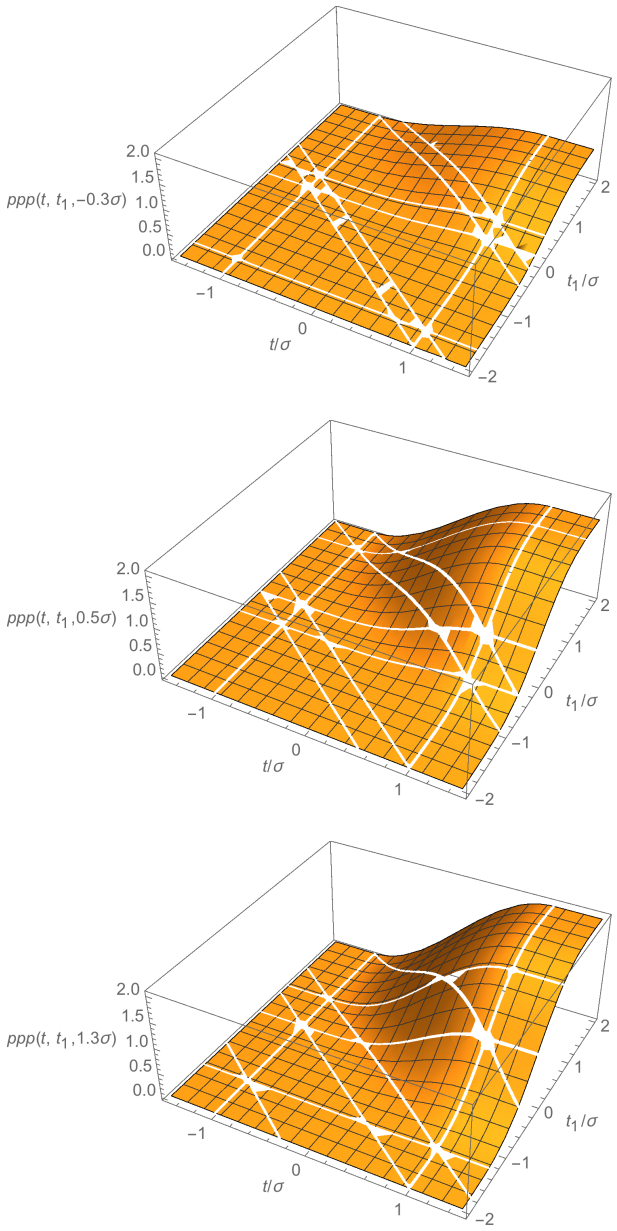

FIGURE 20. Triple pulse propagator as function of its three time variables. Top panel shows contour plot of $ppp(t, t_1, -0.3\sigma)$, middle shows $ppp(t, t_1, 0.5\sigma)$, and bottom shows $ppp(t, t_1, 1.3\sigma)$.

$$m_{SE} = \; imF_u^2 F_r e^{i\varphi_r} \left\langle \psi_0 | e^{iH_e t} e^{-iH_g(t-t_d)} e^{-iH_e t_d} | \psi_0 \right\rangle p(t) pp(t - t_d, t_d) + \text{c.c.} \tag{3.22}$$

$$m_{GSB'} = -imF_u^2 F_r e^{-i\varphi_r} e^{i\epsilon_0(t-t_d)} \left\langle \psi_0 | e^{-iH_e(t-t_d)} | \psi_0 \right\rangle ppp(t, 0, -t_d) + \text{c.c.} \tag{3.23}$$

$$m_{SE'} = imF_u^2 F_r e^{i\varphi_r} e^{-i\epsilon_0(t-t_d)} \left\langle \psi_0 | e^{iH_e(t-t_d)} | \psi_0 \right\rangle p(t - t_d) pp(t, 0) + \text{c.c.} \tag{3.24}$$

In the vibrationally abrupt limit, the GSB, GSB′, and SE′ dipoles are all seen to be determined by the Heller absorption kernel. [60, 61] Only the SE dipole depends on a more complicated overlap between nuclear wave packets undergoing evolution on both ground and excited electronic potential-energy surfaces. As anticipated, the GSB and SE dipoles vanish for t_d less than about $-\sigma$, and the GSB′ dipole does so for delay times greater than σ.

Signal

By spectrally windowing the Fourier coefficients of $E_r(\mathbf{R}, t)$ with a truncated-cosine pulse envelope and inverse Fourier transformation, it is found that the filtered probe-pulse has the temporal form

$$\begin{aligned} E_r'(\mathbf{R}, t) &= E_r' \left(t - \frac{Z}{c} \right) \\ &= E_r' f' \left(t - t_d - \frac{Z}{c} \right) \cos \left[\bar{\omega} \left(t - t_d - \frac{Z}{c} \right) + \varphi_r \right] , \end{aligned} \tag{3.25}$$

where

$$E_r' = 2\sigma \, \delta\omega \, E_r \frac{\cos(\bar{\omega} - \Omega)\sigma}{\pi^2 - 4\sigma^2(\bar{\omega} - \Omega)^2} , \tag{3.26}$$

and

$$f'(t) = \frac{2}{\delta\omega \, t} \sin \left(\frac{\delta\omega}{2} t \right) . \tag{3.27}$$

The electromagnetic interference between the transient-transmission signal field and the spectrally filtered, transmitted probe field given in Eq. (3.5) can be evaluated by a sequence of steps similar to those made by Cina and Kovac in deriving the fissors (i.e., femtosecond stimulated Raman spectroscopy) signal. [62] This derivation is outlined in Appendix B and leads to a compact formula for the transient-transmission signal in which the three-dimensional spatial integral is replaced by a one-dimensional integral over time:

$$\Delta U(\bar{\omega}) = -\bar{\omega} E_r' \int_{-\infty}^{\infty} \mathrm{d}t \; m_{u^2r}(t) f'(t - t_d) \sin[\bar{\omega}(t - t_d) + \varphi_r] \,. \tag{3.28}$$

It should be recalled that the various contributions to $m_{u^2r}(t)$ themselves depend upon the pump-probe delay, as shown in Eqs. (3.21)-(3.24).

Filtered-probe pulse propagator

The basic signal expression (3.28) can be further developed by introducing a reduced propagator for the spectrally filtered probe pulse. With the transient-transmission dipole, $m_{u^2r} = \sum m_A$, written as a sum of the four terms (3.21)-(3.24), the signal becomes $\Delta U = \sum \Delta U_A$ in which, for example,

$$\begin{aligned} \Delta U_{GSB}(\bar{\omega}) &= \bar{\omega} F_u^2 F_r F_r' \int_{-\infty}^{\infty} \frac{\mathrm{d}t}{\sigma'} \, f'(t) e^{i\bar{\omega}t} \, ppp(t, t_d, 0) \langle \psi_0 | e^{iH_g t} e^{-iH_e t} | \psi_0 \rangle \; + \; \text{c.c.} \\ &= \bar{\omega} F_u^2 F_r F_r' \, \langle \psi_0 | p'^{(ge)}(\infty; t) | \psi_0 \rangle \, ppp(t, t_d, 0) + \text{c.c.} \,; \end{aligned} \tag{3.29}$$

notice the additional t-nesting. We have introduced a filtered-probe pulse-duration parameter, $\sigma' = 2\pi/\delta\omega$, along with the new reduced propagator,

$$p'^{(ge)}(\infty;t) = \int_{-\infty}^{\infty} \frac{\mathrm{d}t}{\sigma'}\, f'(t) e^{i\bar{\omega}t} e^{iH_g t} e^{-iH_e t}\,, \tag{3.30}$$

and an $\bar{\omega}$-dependent function $F'_r = mE'_r\sigma'/2$. By similar arguments, we readily obtain

$$\Delta U_{SE}(\bar{\omega}) = \bar{\omega} F_u^2 F_r F'_r \,\langle \psi_e(t_d)|p'^{(eg)}(\infty;t)|\psi_e(t_d)\rangle\, p(t+t_d) pp(t,t_d) + \text{c.c.}\,, \tag{3.31}$$

where $|\psi_e(t_d)\rangle \equiv \exp\{-iH_e t_d\}|\psi_0\rangle$ and $p'^{(eg)} = (p'^{(ge)})^\dagger$;

$$\Delta U_{GSB'}(\bar{\omega}) = \bar{\omega} F_u^2 F_r F'_r \,\langle \psi_0|p'^{(ge)}(\infty;t)|\psi_0\rangle\, ppp(t+t_d,0,-t_d) + \text{c.c.}\,; \tag{3.32}$$

and

$$\Delta U_{SE'}(\bar{\omega}) = \bar{\omega} F_u^2 F_r F'_r \,\langle \psi_0|p'^{(eg)}(\infty;t)|\psi_0\rangle\, p(t) pp(t+t_d,0) + \text{c.c.}\,. \tag{3.33}$$

Because nuclear motion cannot be neglected on the prolonged σ'-timescale, it would be illegitimate to replace $e^{i\bar{\omega}t}e^{iH_g t}e^{-iH_e t}$ by unity in Eq. (3.30): this is the locus of whatever essential nuclear dynamics underlies a given contribution to the transient-absorption signal.

All four signal contributions are expressed in terms of t-dependent quantum mechanical overlaps between differently evolving nuclear wave packets. [9] Among them, under the present assumption of vibrationally abrupt incident pulses, only ΔU_{SE} is specified by an overlap depending additionally on the pump-probe delay t_d. The others depend on t_d only through the pulse propagators. It is through

this stimulated-emission contribution that the transient-absorption signal exhibits signatures of delay-dependent nuclear dynamics in the excited electronic state.

Signal Calculations

DBV model and pulse parameters

Using the framework spelled out above, we next simulate and interpret transient-transmission signals from a system roughly modeled on the DBV pigments of the PC577 algal light-harvesting complex. As our main purpose is to elucidate some specific features of vibrational quantum beats originating in an excited electronic state, the model incorporates only the ground and first excited electronic states of a single dihydrobiliverdin pigment. Higher states—and the process of excited-state absorption—could be incorporated by a straightforward extension of the theory. For simplicity, the two corresponding nuclear Hamiltonians are treated as mutually displaced, multidimensional harmonic oscillators. In addition to vibrational modes at each of the eight quantum-beat frequencies $\omega_6, \ldots, \omega_{13} = 190$, 270, 370, 450, 470, 510, 660, and 810 cm^{-1} identified by McClure *et al.*, citeMcClure14 we introduce five vibrations at the arbitrary lower frequencies $\omega_1, \ldots, \omega_5 = 29.0$, 36.3, 43.6, 57.7, and 71.8 cm^{-1} to mimic a 'continuum' of background modes responsible for 'solvation dynamics.' [63] We do not incorporate 'damping' of the individual modes due to their anharmonic interactions with each other or with additional auxiliary nuclear degrees of freedom, which could easily be accomplished within a multi-mode Brownian-oscillator model, [12] as a simple picture of multiple uncoupled vibrational degrees of freedom is adequate for our present purposes. Although the calculations presented in this section are for $T = 0$, it will be demonstrated below (in Sec. 3.4) that our basic theory applies as written

to nonzero temperature, despite its pure-state nature. While thermal effects at ambient temperature would likely be noticeable for the background modes, the qualitative interpretation of our illustrative simulations would be affected only slightly; the same would probably be the case for the introduction of small ground-to-excited-state shifts in the frequencies of the vibrations weakly coupled to the electronic transition. Nonzero-temperature effects could readily be introduced in our model as they were by Pollard, *et al.*, [8] using basic expressions from condensed-matter physics for thermal averages of the relevant wave-packet overlaps, given in our formulation by Eqs. (3.38) and (3.39) below, in terms of a thermally averaged version of the Heller kernel.

The nuclear Hamiltonians for the g- and e-states of our model are given by

$$H_g = \frac{1}{2}\left(P_1^2 + \cdots + P_{13}^2 + \omega_1^2 Q_1^2 + \cdots + \omega_{13}^2 Q_{13}^2\right) , \tag{3.34}$$

and

$$H_e = \frac{1}{2}\left[P_1^2 + \cdots + P_{13}^2 + \omega_1^2 (Q_1 - D_1)^2 + \cdots + \omega_{13}^2 (Q_{13} - D_{13})^2\right] + \epsilon \, , \tag{3.35}$$

respectively, with mass-weighted coordinates and momenta. McClure, *et al.*[1] do not quantify the observedly weak electronic-vibrational coupling of the modes responsible for the quantum beats in their transient absorption signals. In rough accord with their Fig. 4(b), we set each mode's Franck-Condon energy, $\omega_k \delta_k^2$, where $\delta_k \equiv D_k \sqrt{\omega_k/2}$, equal to a constant single-mode value λ_e. We arrive at a specific value, $\lambda_e = 53.3\,\mathrm{cm}^{-1}$, by hypothesizing—perhaps consistently with McClure's Fig. 2(c), the form of whose null-line suggests that about half of the Stokes shift derives from vibrationally *unresolved* solvation dynamics—that the vibrations

making discernible oscillatory contributions to the experimental signals are together responsible for the other half of the Stokes shift between the absorption peak at 577 nm and the steady-state fluorescence peak at 640 nm. In this way we are led to the choices $\delta_6, \ldots, \delta_{13} = 0.5297$, 0.4444, 0.3796, 0.3442, 0.3368, 0.3233, 0.2842, and 0.2566.

Serving in place of a quasi-continuum of many weakly coupled, low frequency background modes which remain unresolved in transient absorption due to spectral congestion, our five slower modes are again assigned Franck-Condon displacements such that each of them makes an equal contribution to the Stokes shift, and their combined contribution to the Stokes shift equals that of the eight higher-frequency vibrations (i.e. half of the total Stokes shift). Because these slow vibrations are fewer in number and lower in frequency than the 'molecular' vibrations, their assigned displacements are relatively large: $\delta_1, \ldots, \delta_5 = 1.090$, 1.216, 1.399, 1.533, and 1.715.

With $n_j = (n_{1j}, \ldots, n_{13j})$ and $j = g, e$, the eigenstates and eigenenergies of our model system are

$$|g\rangle|n_g\rangle \text{ and } \epsilon_{n_g} = \omega_1 \left(n_{1g} + \frac{1}{2}\right) + \cdots + \omega_{13} \left(n_{13g} + \frac{1}{2}\right) , \tag{3.36}$$

and

$$|e\rangle|n_e\rangle \text{ and } \epsilon_{n_e} = \epsilon + \omega_1 \left(n_{1e} + \frac{1}{2}\right) + \cdots + \omega_{13} \left(n_{13e} + \frac{1}{2}\right) . \tag{3.37}$$

Because the equilibrium nuclear positions in the e-state are shifted from those in g, we have $|n_e\rangle = \exp\{-i\mathbf{P} \cdot \mathbf{D}\}|n_g\rangle$. In the initial state $|g\rangle|\psi_0\rangle$, we take $|\psi_0\rangle = |0_{1g}, \ldots 0_{13g}\rangle$, the overall vibrational ground state.

Our choices for the mode frequencies give $\epsilon_0 = 1984.2$ cm^{-1} for the ground-state vibrational energy. Rather than assigning a value to ϵ, we simply treat this bare electronic (0-0) transition energy as large enough that variations in the probed frequency $\bar{\omega}$ over the range of significant transient absorption can be neglected in the prefactors of Eqs. (3.29) and (3.31)-(3.33). The transition dipole m is regarded as an unspecified constant.

The experimentally observed oscillations in the transient-transmission signal at various vibrational frequencies decay with a median damping time of about 400 fs. This damping could have multiple sources, including electronic energy transfer (from DBV to PCB), vibrational dephasing, and radiative decay. We account for such damping by introducing a phenomenological e-state amplitude decay rate $\Gamma/2$, with $\Gamma = 3.0 \times 10^{-3}$ fs^{-1} (corresponding to a population-decay time of 333 fs). Formally, amplitude decay is then incorporated by replacing the e-state time-evolution operator $\exp\{-iH_e t\}$ by $\exp\{-iH_e t - \Gamma|t|/2\}$ wherever it appears in the various wave-packet overlaps governing transient transmission. This *ad hoc* treatment of electronic excited-state amplitude decay does not contribute to electronic 'pure dephasing.' Within our model the latter process is the province of the small collection of low-frequency background modes which, if they were somewhat more numerous, would lead to a permanent decay of electronic coherence independent of electronic population decay.

We can now provide formulas for the overlaps required in Eq. (3.29) and Eqs. (3.31) - (3.33), with the reduced pulse propagator for the spectrally filtered probe written explicitly, as in Eq. (3.30). Phenomenological e-state amplitude decay at the rate $\Gamma/2$ is incorporated as described above. The GSB, GSB$'$, SE$'$ overlaps

depend on the $e \leftarrow g$ Heller absorption kernel, [64, 65]

$$\langle\psi_0|e^{iH_g t}e^{-iH_e t}|\psi_0\rangle = e^{-i\epsilon t-\frac{\Gamma}{2}|t|}\prod_k e^{\delta_k^2\left(e^{-i\omega_k t}-1\right)}, \tag{3.38}$$

where $\delta_k \equiv \sqrt{\frac{\omega_k}{2}}D_k$. The wave-packet overlap governing the SE process becomes

$$\langle\psi_e(t_d)|e^{iH_e t}e^{-iH_g t}|\psi_e(t_d)\rangle = \ e^{i\epsilon t-\frac{\Gamma}{2}|t_d|-\frac{\Gamma}{2}|t+t_d|}\prod_k e^{\delta_k^2\left[2i\sin\omega_k(t+t_d)-2i\sin\omega_k t_d+e^{-i\omega_k t}-1\right]}. \tag{3.39}$$

It remains to specify the optical features of the measurements to be simulated. We set the common carrier frequency Ω of pump and probe pulses equal to ϵ, so that their spectral density spans equally the steady-state absorption and fluorescence spectra. We use a short incident pulse-duration parameter $\sigma =$ 9.425 fs. As the amplitudes of both pulses are assumed to be in the weak-field limit, and all signal contributions to be proportional to $E_u^2 E_r^2$ as a result, it is unnecessary to assign specific values to E_u and E_r. The spectral resolution is set at $\delta\omega = 104.2$ cm^{-1}, so the filtered-probe duration parameter becomes $\sigma' = 320.0$ fs, which is intermediate between the periods of the slowest 'molecular' vibration and the fastest background mode.

In order to provide an initial optical characterization of the thirteen-mode model Hamiltonian, we calculate the linear absorption spectrum according to the formula [64]

$$\Sigma(\omega) = \frac{m^2}{2\pi}\int_{-\infty}^{\infty} dt\, e^{i\omega t}\langle\psi_0|e^{iH_g t}e^{-iH_e t}|\psi_0\rangle, \tag{3.40}$$

making use of Eq. (3.38). The resulting spectrum is shown in Fig. 21., along with the power spectrum of the incident pump and probe pulses to be used in our transient-transmission calculations.

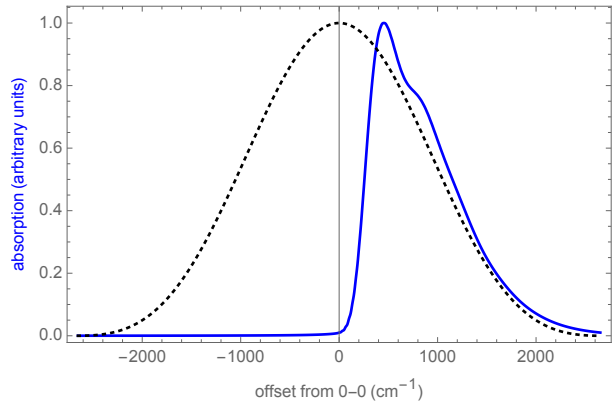

FIGURE 21. Electronic absorption spectrum of thirteen-mode model system is shown in blue. Common power spectrum of incident pump and probe pulses to be used in calculating time-resolved signals is given by dotted black curve.

Contributions to delay-dependent transient transmission

The calculated ground-state bleach contribution to the transient-transmission signal is pictured in the top panel of Fig. 22.. As anticipated, it turns on over the duration of the pump-probe overlap near $t_d = 0$, and, for positive delays, gives a positive signal contribution that resembles the absorption spectrum windowed by the spectral intensity of the incident pulses. In addition to the positive-going absorption-spectrum-like bleach to the blue of the bare electronic transition frequency, there is a small negative 'bleach' to the red of 0-0 that occurs only near zero delay-time. Due to the short-pulse approximation adopted for the reduced propagators, and the assumption of a coordinate-independent dipole-moment operator, the pump pulse does not generate nuclear motion in the electronic ground state by impulsive stimulated Raman excitation. [50] As a result, the GSB term does not exhibit vibrational quantum beats.

The bottom panel of Fig. 22. shows the stimulated-emission signal contribution for the model system. The main ridge of this largely positive-going

term commences near $t_d = 0$ and undergoes a dynamical Stokes shift over the next several hundred femtoseconds. High-frequency ripples corresponding to vibrational quantum beats—due to coherent nuclear motion in the excited electronic state—cross this descending peak-frequency ridge. There is a strong tendency for the peak (or trough) of each ripple on one side (the blue or the red) of the main ridge to become a trough (or peak) on the other side. These features are three-dimensional renderings of the antiphasing of vibrational oscillations on opposite sides of the Stokes-shifting peak emission frequency observed in Ref. 7.

Contour plots of both GSB and SE signals are presented in Fig. 23., with the latter plotted as tanh[constant $\times$ $\Delta U_{SE}(\bar{\omega})$] in order to emphasize its weaker features. Comparison of the two panels makes it clear that for the strongly Stokes-shifting model system under study, these signal contributions reside mostly in separate probed-frequency ranges (we shall see shortly that GSB$'$ and SE$'$ also do not significantly obscure the stimulated-emission signal to the red of the 0-0 transition frequency). This separation allows us meaningfully to regard the SE contribution as a *signal*—rather than a contribution to the signal—at positive delay times and to further interpret the connection between its spectral dynamics and the underlying multidimensional wave-packet motion in the excited electronic state.

Contour plots of the GSB$'$ and SE$'$ terms are given in Fig. 24.. As expected from Eq. (3.23), the former is confined mostly to short negative t_d. The latter term is nonzero for short negative delay-times as well, and also exhibits a GSB-like positive feature spanning the absorptive spectral region for all positive delays. In our model system excited by very short pulses, neither of these terms displays vibrational beating nor occupies the spectral/delay region housing most of the stimulated-emission signal.

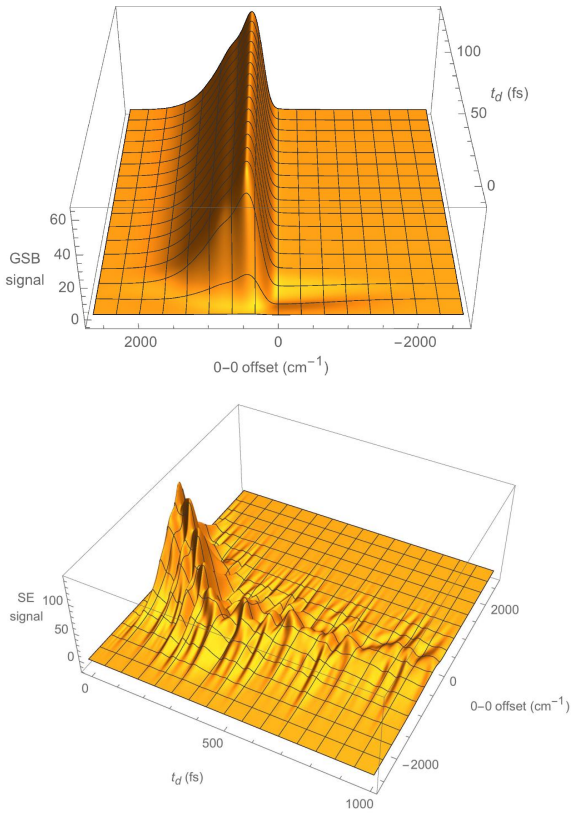

FIGURE 22. Plot of ground-state-bleach contribution (top) and stimulated-emission
contribution (bottom) to transient-transmission signal. Under vibrationally abrupt approximation, GSB turns on at zero delay over short interval $\sim \sigma$ and fails to exhibit vibrational oscillations; SE alone exhibits
vibrational quantum beats.

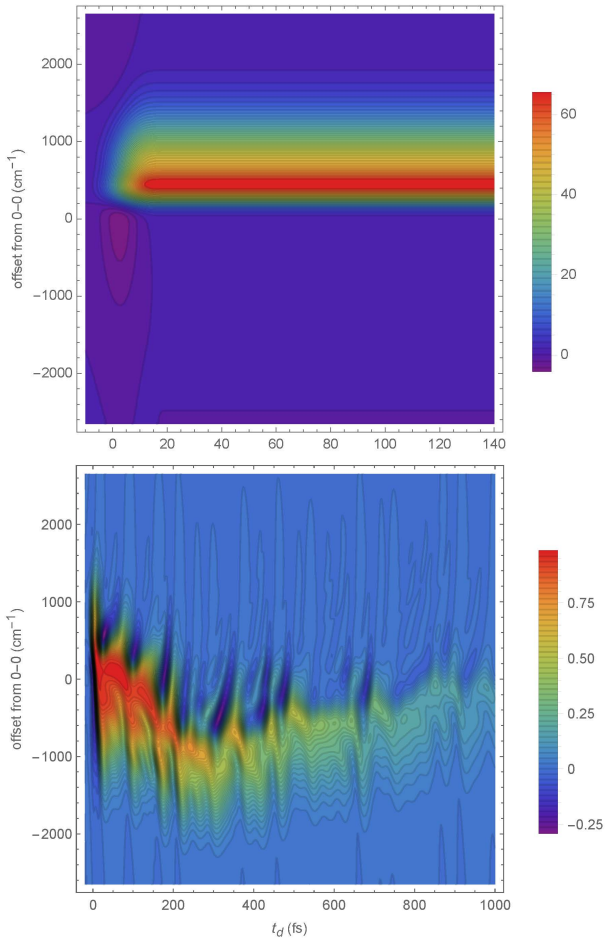

FIGURE 23. Contour plots of GSB (top) and SE (bottom, with hyperbolic-tangent scaling to emphasize low-amplitude features). GSB, while substantial in size for positive delays, does not exhibit quantum beats and, apart from small negative contribution to the red of 0-0 frequency near
$t_d = 0$, resides mostly to blue of SE.

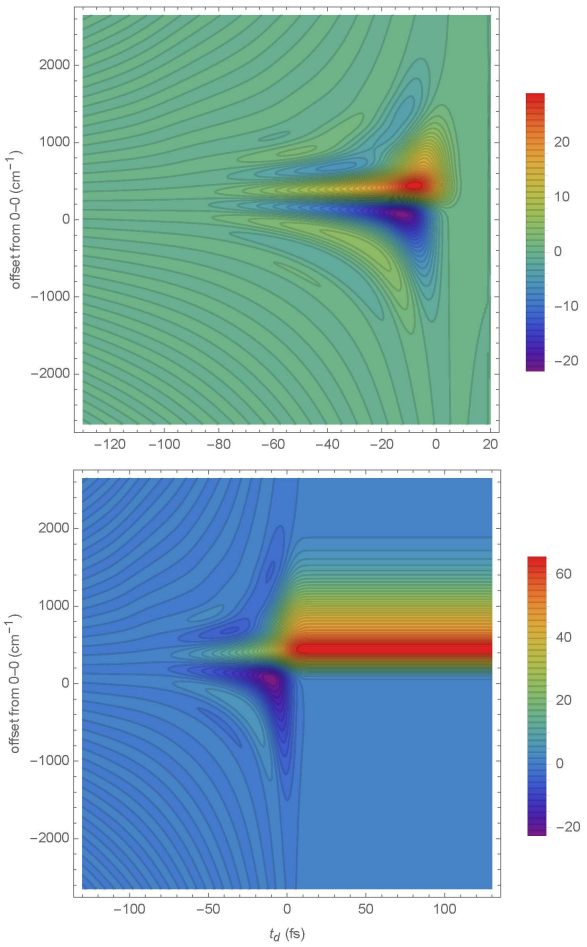

FIGURE 24. Contour plots of GSB′ (top) and SE′ (bottom) contributions to transient-transmission signal. GSB′ is substantial only for negative t_d. Like GSB (see preceding figure), SE′ is largely confined to positive delays, shows no quantum beats, and is concentrated to blue of SE.

Our GSB and GSB′ signal contributions both correspond to single 'diagrams' in the usual response-function description. [8] On the other hand, our SE and SE′ signals each comprise three double-sided diagrams within that formulation. [6] That this correspondence is rigorous, rather than qualitative, is argued further in Sec. **??**

Features of the stimulated-emission signal

The main peak of the calculated SE signal shown in the lower panels of Figs. 22. and 23. tracks the early-time dynamical Stokes shifting caused by excited-state wave-packet motion in the 'background modes' (i.e., those whose motion is slow enough to be time-resolved by the decay-time of the SE dipole of Eqs. (3.22) and (3.39)). This behavior is analogous to the frequency-tracking limit observed experimentally [66] and theoretically [62] in femtosecond stimulated Raman spectroscopy (fissors) signals when the frequency of a Raman-active vibrational transition is modulated by coherent motion of another, very slow 'structural' mode. The eight higher-frequency modes included in our model give rise to quantum-beat ripples analogous to the antiphased sidebands produced alongside fissors peaks by coupling to nuclear degrees of freedom too rapid to be time-resolved within the

[6] The matrix elements of the dipole-moment operator listed in Eqs. (7) and (8) are the source terms for the transient-absorption signal. In comparison with parts a through h in Fig. 1 of Pollard and coworkers, [8] we have

$$d = \mathrm{GSB}\,,$$
$$h = \mathrm{GSB}'\,,$$
$$a + b + f = \mathrm{SE}\,,$$

and

$$c + e + g = \mathrm{SE}'\,.$$

The positive-t_d signal that can appear in SE′ (see Sec. 3.3) in particular would enter through term-c in Pollard's description. These correspondences concur with those listed by Pollard, *et al.* in abstracting a wave-packet picture from the nonlinear response-function formalism.

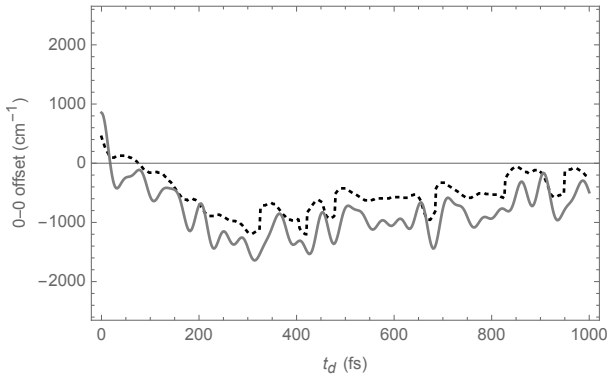

FIGURE 25. Comparison of time-evolving peak frequency in calculated SE spectrum (dotted) and time-dependent instantaneous difference potential for classical motion in e-state starting without initial momentum at Franck-Condon point (continuous curve). Offset between the curves is due in large part to fall-off in probe-pulse power spectrum with increasing red-shift from its center.

vibrational dephasing time or the trailing edge of the envelope of the narrow-band Raman pump pulse. [62, 67]

Approximate tracking of the instantaneous *electronic* transition frequency by the peak emission frequency of the SE signal is illustrated in Fig. 25.. Here are compared the time-dependent local electronic difference frequency between e- and g-states following short-pulse electronic excitation (solid curve) and the time-dependent peak frequency of the calculated stimulated-emission signal (dotted). The systematic shift to the blue of the SE peak frequency relative to the instantaneous difference frequency can be ascribed to the fall-off in spectral density of the probe pulse, whose center frequency coincides with 0-0 in our calculations.

The stimulated-emission signal intensity along the peak-emission ridge is plotted as the dotted curve in Fig. 26.. The diminished intensities observed along transient-transmission curves 275.9 cm^{-1} to the red and blue of the peak-emission path are also shown. Intensities on the red- and blue-shifted paths clearly exhibit the antiphasing expected in sidebands of a 'frequency modulated' emission signal.

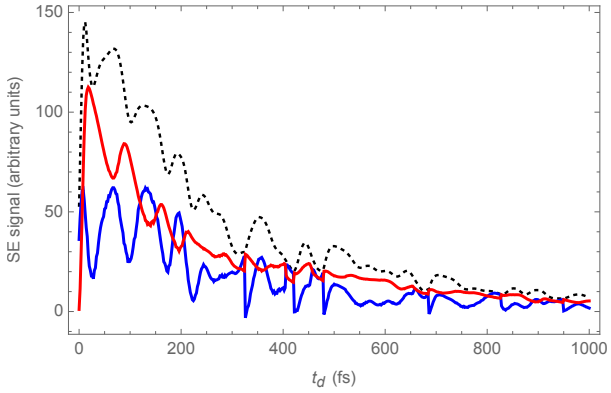

FIGURE 26. Dotted curve plots calculated SE signal along path of peak frequency as function of t_d shown in previous figure. Red and blue curves are SE signal along frequency-versus-t_d paths shifted by minus or plus 276 cm^{-1} from path of peak frequency, respectively. Note prominence of antiphasing between red and blue curves.

But such a description would be an oversimplification here, as the amplitude of the 'carrier wave' is also modulated and its frequency additionally shifted by motion in the slow background modes. In general, of course, the frequencies of vibrational modes signficantly coupled to a given electronic transition may constitute a quasi-continuum, and there need be no sharp break between modes responsible for observable shifts in the peak emission frequency and those generating antiphased sidebands.

Why the phase-flip?

Figure 27. illustrates the source of the observed antiphasing of sideband oscillations at probed frequencies having small, opposite shifts from that of peak fluorescence in a system having multiple vibrational modes which are weakly coupled to an electronic transition. It differs from prior analyses of emission-frequency oscillations in the pump-probe signals of systems undergoing large amplitude motion due to strong electronic-vibrational coupling (typically in a

single mode of vibration). [11, 50, 68, 69] Under such *large-amplitude* motion in an excited electronic state, with blue- and red-shifted emission emanating, say, from inner and outer turning points, respectively, of a single mode of vibration, the two emission traces will typically be out of phase with each other: when a compact nuclear wave packet is located at the inner turning point, blue-shifted emission is high and red emission low, and *vice versa* as the wave packet moves to the outer turning point. Prior to vibrational dephasing, emission at the intermediate probed frequency corresponding to the eventual peak of steady-state fluorescence typically oscillates at twice the frequency of vibrational motion, peaking at times midway between the maxima of red- and blue-shifted emission. A similar description applies to one-dimensional vibrational motion in the electronic ground state, with the peak frequency of transient absorption oscillating at the active-mode frequency about the peak frequency of continuous-wave absorption.

The situation at hand in PC577 is at once more complicated and simpler. On one hand, *many* vibrational modes are activated by short-pulse electronic excitation; on the other, these modes execute only small-amplitude motion (that is, motion of a smaller range than the zero-point width of the probability distribution in each vibrational degree of freedom). As indicated pictorially in Fig. 27., any small displacement of a multi-mode nuclear wave packet in the excited electronic state will tend to transfer probablity density from nuclear configurations favoring slightly blue-shifted to those favoring slightly red-shifted emission, or *vice versa*. Although emission in either channel will oscillate with increasing excitation-observation delay as some complicated superposition of various-frequency sinusoidal functions, the two time-traces will tend to be temporally out of phase. That is, when a wave packet happens to be slightly displaced from the minimum of the

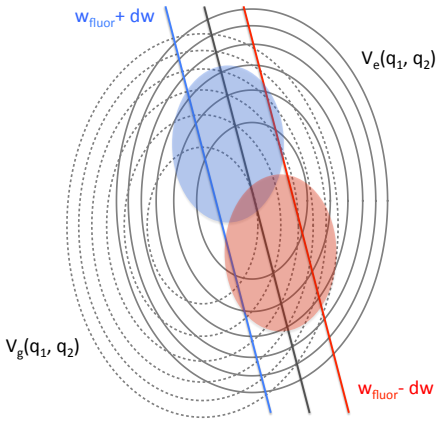

FIGURE 27. Schematic illustration of source of antiphased sideband oscillations in stimulated-emission signal. Plot shows contour diagrams of hypothetical two-dimensional ground- and excited-state electronic potential energy surfaces. Slanted black line through minimum of $V_e(q_1, q_2)$ is locus of points for which excited-minus-ground difference potential equals steady-state peak fluorescence frequency. Difference potential is shifted by plus or minus some small amount along blue and red lines, respectively. When nuclear wave packet (light blue oval) executes arbitrary small displacement (to pink location), probability amplitude is lost (or gained) along blue-shifted resonance line and simultaneously gained (or lost) along red-shifted line.

multidimensional potential surface as indicated by the blue region in Fig. 27., then the net oscillating component of the pump-probe signal will be opposite in phase from when the wave packet's motion takes it to the red region. In either case, the wave packet is only slightly displaced from the black line indicating the probed frequency at which the node is observed.

This explanation of sideband antiphasing is qualitative and generic. In general, wave-packet spreading and deformation can lead to more complicated relationships between emission traces at different frequencies. For instance, in the presence of spreading, the emission signals in red- and blue-shifted channels considered above could increase or decrease in phase with each other, or have their relative intensities change in some arbitrary way reflective of the evolution

of nuclear probability density along 'red' and 'blue' difference-potential loci. Nor do these loci need to correspond to 'flat' surfaces in nuclear configuration space (lines in 2D); nor even to (N-1)-dimensional surfaces (curves in 2D).

In the transient-transmission data of Ref. 7 and our calculated SE signal, sideband antiphasing is observed about the *Stokes-shifting* peak emission frequency, not just the steady-state value. A simple analysis based on the differing behavior of the lower- and higher-frequency modes reveals the source of this multi-mode antiphasing in the vibrational sidebands arising from the latter group. A more formal treatment of Eq. (3.39) based on a Fourier-Bessel expansion could be useful for a quantitative analysis of the stimulated-emission signal. [7] The partitioning of vibrational modes between 'slow' and 'not so slow,' here corresponding to vibrations 1 through 5 and 6 through 13, respectively, is based on whether or not $\omega_k t_o \ll 1$, where t_o is the relevant 'optical dephasing time' (approximate lifetime of the SE overlap).

Making a short-t expansion for the slow modes in the exponent of Eq. (3.39) and a power-series expansion in the squared Franck-Condon displacements of the faster modes, the SE overlap can be approximated as

$$\begin{aligned}\langle\psi_e(t_d)|e^{iH_e t}e^{-iH_g t}|\psi_e(t_d)\rangle \cong\ & e^{it\epsilon_s(t_d)-t^2\chi_s(t_d)-\frac{\Gamma}{2}|t_d|+\frac{\Gamma}{2}|t+t_d|} \\ \times\{1+\sum_f \delta_f^2\left[2i\sin\omega_f(t+t_d)-2i\sin\omega_f t_d+e^{-i\omega_f t}-1\right]+\dots\}\,, & \qquad (3.41)\end{aligned}$$

where

$$\epsilon_s(t_d)=\epsilon+\sum_s \omega_s\delta_s^2(2\cos\omega_s t_d-1) \qquad (3.42)$$

[7] A. T. N. Kumar, *et al.* make use of such an expansion for a single-mode system.

and

$$\chi_s(t_d) \equiv \chi_s' + i\chi_s''(t_d) = \sum_s \omega_s^2 \delta_s^2 \left(\frac{1}{2} + i \sin \omega_s t_d \right) . \tag{3.43}$$

$\epsilon_s(t_d)$ represents the contribution of the slow modes to the time-dependent electronic difference potential (compare Fig. 27.). The real part of $\chi_s(t_d)$ provides a maximum value $\sqrt{\ln 2/\chi_s'}$ (= 43.8 fs in our model) for the optical dephasing time.

The expansion inside the curly brackets of Eq. (3.41) is motivated by the small size, $\delta_f^2 \ll 1$, of the dimensionless Franck-Condon displacements of the fast vibrational modes. This expansion leads to a power-series expression for the stimulated-emission signal:

$$\Delta U_{SE}(\bar{\omega}) \cong \Delta U_{SE}^{(0)} + \Delta U_{SE}^{(1)} + \Delta U_{SE}^{(2)} + \cdots . \tag{3.44}$$

If the reduced pulse propagators in Eq. (3.31) involving incident pulses are approximated with step functions,

$$p(t + t_d) pp(t, t_d) \simeq p_{max}^3 \theta(t) \theta(t_d) , \tag{3.45}$$

where $p_{max} = \int_{-\infty}^{\infty} \frac{dt}{\sigma} f(t)$—here equal to $4/\pi$—the zeroth-order portion of the SE signal then becomes

$$\begin{aligned} \Delta U_{SE}^{(0)} \cong\ & 2\bar{\omega} F_u^2 F_r F_r' p_{max}^3 \theta(t_d) e^{-\Gamma t_d} \\ & \times \int_0^{\infty} \frac{dt}{\sigma'} f'(t) e^{-t^2 \chi_s' - \frac{\Gamma}{2} t} \cos\{t[\bar{\omega} - \epsilon_s(t_d)] + t^2 \chi_s''(t_d)\} . \end{aligned} \tag{3.46}$$

This signal contribution, plotted in the top panel of Fig. 28., does not exhibit quantum beats at the higher vibrational frequencies. It is more-or-less evenly peaked about a Stokes shifting probed frequency $\bar{\omega} = \epsilon_s(t_d)$ and has width

consistent with the estimate $\Delta\bar{\omega} \simeq 2\pi\sqrt{\chi_s'/\ln 2}$ (= 761 cm^{-1} in the present model).

Making the same approximations in the first-order SE signal leads to

$$\Delta U_{SE}^{(1)}(\bar{\omega}) \cong 2\bar{\omega}F_u^2F_rF_r'p_{max}^3\theta(t_d)e^{-\Gamma t_d}\int_0^\infty \frac{dt}{\sigma'}\,f'(t)e^{-t^2\chi_s'-\frac{\Gamma}{2}t}$$
$$\times\Bigg\{\cos[t(\bar{\omega}-\epsilon_s(t_d))+t^2\chi_s''(t_d)]\sum_f\delta_f^2[\cos\omega_f t-1]$$
$$+\sin[t(\bar{\omega}-\epsilon_s(t_d))+t^2\chi_s''(t_d)]$$
$$\times\sum_f\delta_f^2[\sin\omega_f t(2\cos\omega_f t_d-1)+2(\cos\omega_f t-1)\sin\omega_f t_d]\Bigg\}\,. \qquad (3.47)$$

In this form, $\Delta U_{SE}^{(1)}$ is seen to be a source for quantum beats at the fundamental vibrational frequencies ω_f and to die out for probed-frequency offsets $|\bar{\omega}-\epsilon_s(t_d)|$ greater than about $\pi\sqrt{\chi_s'/\ln 2}$. The first-order contribution to the SE signal is plotted in the bottom panel of Fig. 28.. It exhibits antiphasing of the vibrational quantum-beat structure to the blue and red of the instantaneous peak-emission frequency.

The assigned values of the fast-mode Franck-Condon factors in our model are not actually small enough to justify truncation of the expansion of Eq. (3.39) at low order in

$$\phi_{fast}(t,t_d)=\sum_f\delta_f^2\left[2i\sin\omega_f(t+t_d)-2i\sin\omega_f t_d+e^{-i\omega_f t}-1\right]\,; \qquad (3.48)$$

indeed, this quantity is seen in Fig. 29. to have magnitudes larger than unity at many time-points. As a result, an expansion in the form of Eq. (3.44) would converge numerically only at high order. This observation is consistent with the

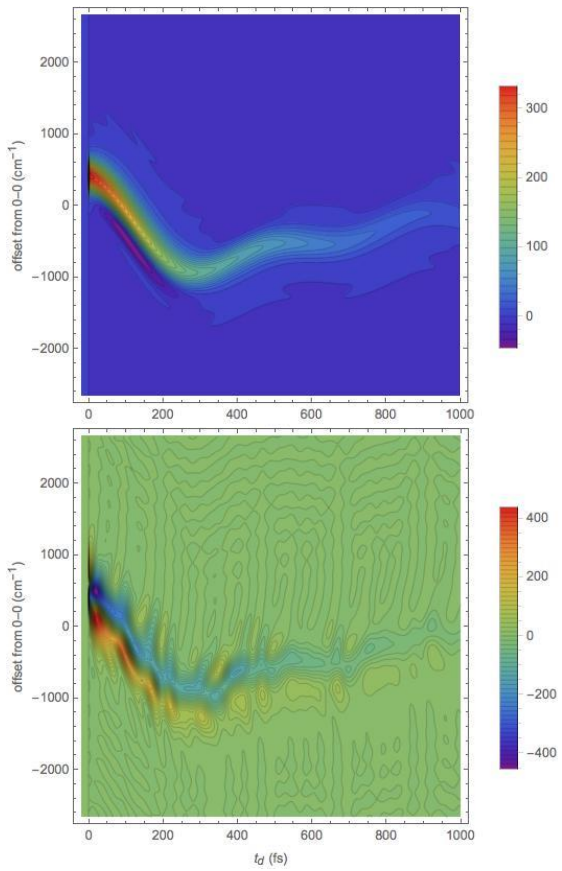

FIGURE 28. Approximate contribution to the stimulated-emission signal of zeroth order in the squares of the fast-mode Franck-Condon displacements (top), as given by Eq. (3.46), and of first order in the squares of the fast-mode Franck-Condon displacements (bottom), calculated from Eq. (3.47). Note the phase-flip in vibrational beat structure evidenced by the difference in sign of the first-order signal on opposite sides of the evolving peak-emission frequency $\epsilon_s(t_d)$.

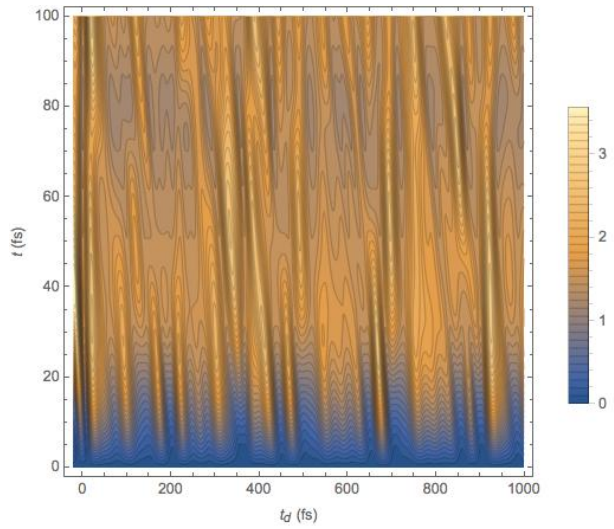

FIGURE 29. Absolute value of the function $\phi_{fast}(t, t_d)$ appearing in the exponent of Eq. (3.39) and accounting for role of higher-frequency vibrational modes in the time- and delay-time evolution of the stimulated- emission overlap.

comparable sizes of the approximate $\Delta U_{SE}^{(0)}$ and $\Delta U_{SE}^{(1)}$ plotted in Fig. 28..

In order to account for the appearance of quantum beats at the fundamental of a particular higher-frequency vibration in a certain probed-frequency range, it is nonetheless useful to identify terms proportional to $e^{\pm i\omega_f t_d}$ within $\Delta U_{SE}^{(1)}$. To that purpose, we can make the replacement

$$\begin{aligned} & 2i\sin\omega_f(t+t_d) - 2i\sin\omega_f t_d + e^{-i\omega_f t} - 1 \\ &= e^{i\omega_f(t+t_d)} - e^{-i\omega_f(t+t_d)} - e^{i\omega_f t_d} + e^{-i\omega_f t_d} + e^{-i\omega_f t} - 1 \\ &\to e^{i\omega_f t_d}[e^{i\omega_f t} - 1] - e^{-i\omega_f t_d}[e^{-i\omega_f t} - 1]\,; \end{aligned} \tag{3.49}$$

the omitted terms cannot give rise to ω_f-oscillations as a function of t_d, and make signal contributions smaller by about δ_f^2 than $\Delta U_{SE}^{(0)}$. The ω_f-fundamental part of

the first-order SE signal is then

$$\begin{aligned}\Delta U_{SE,\omega_f}(\bar{\omega}) \cong\ & \delta_f^2 \bar{\omega} F_u^2 F_r F_r' p_{max}^3 \theta(t_d) e^{-\Gamma t_d} \\ & \times \int_0^\infty \frac{dt}{\sigma'} f'(t) e^{-t^2\chi_s' - \frac{\Gamma}{2}t} e^{-it(\bar{\omega} - \epsilon_s(t_d)) - it^2\chi_s''(t_d)} \\ & \times \left\{ e^{i\omega_f t_d}[e^{i\omega_f t} - 1] - e^{-i\omega_f t_d}[e^{-i\omega_f t} - 1] \right\} + \text{c.c.}\,. \end{aligned} \tag{3.50}$$

For probed frequencies near the delay-dependent peak-emission frequency ($\bar{\omega} \simeq \epsilon(t_d)$), the minus-one terms within the square brackets predominate, and

$$\begin{aligned}\Delta U_{SE,\omega_f}(\epsilon_s(t_d)) \approx\ & -4\delta_f^2 \sin(\omega_f t_d) \epsilon_s(t_d) F_u^2 F_r F_r' p_{max}^3 \theta(t_d) e^{-\Gamma t_d} \\ & \times \int_0^\infty \frac{dt}{\sigma'} f'(t) e^{-t^2\chi_s' - \frac{\Gamma}{2}t} \sin[t^2\chi_s''(t_d)]\,. \end{aligned} \tag{3.51}$$

On the other hand, if the probed frequency is off emission resonance by $\pm\omega_f$, then one of the $e^{\pm i\omega_f t}$ terms in square brackets predominates, and we get

$$\begin{aligned}\Delta U_{SE,\omega_f}(\epsilon_s(t_d) \pm \omega_f) \approx\ & \pm 2\delta_f^2(\epsilon_s(t_d) \pm \omega_f)) F_u^2 F_r F_r' p_{max}^3 \theta(t_d) e^{-\Gamma t_d} \\ & \times \int_0^\infty \frac{dt}{\sigma'} f'(t) e^{-t^2\chi_s' - \frac{\Gamma}{2}t} \cos[\omega_f t_d \mp t^2\chi_s''(t_d)]\,. \end{aligned} \tag{3.52}$$

With our choice of model parameters,

$$\int_0^\infty \frac{dt}{\sigma'} f'(t) e^{-t^2\chi_s' - \frac{\Gamma}{2}t} \cos[t^2\chi_s''(t_d)]$$

turns out to be about four times larger than

$$\int_0^\infty \frac{dt}{\sigma'} f'(t) e^{-t^2\chi_s' - \frac{\Gamma}{2}t} \sin[t^2\chi_s''(t_d)]$$

over most of the range $0 < t_d < 1\,\mathrm{ps}$, and this disparity would become more pronounced with a wider, more closely spaced spectrum of low-frequency modes. So we see that $\Delta U_{SE,\omega_f}(\epsilon_s(t_d) \pm \omega_f)$ is dominated by the portion proportional to $\pm\cos\omega_f t_d$. As observed experimentally and in our numerical results, the ω_f-oscillations offset by plus and minus ω_f from emission resonance are therefore nearly 180 degrees out of phase from each other. A difference in their relative magnitude derives mostly from the change in the filtered-probe-field factor F_r' between frequencies $\epsilon_s(t_d) + \omega_f$ and $\epsilon_s(t_d) - \omega_f$.

The same disparity between $\cos(t^2\chi_s'')$- and $\sin(t^2\chi_s'')$-terms accounts for the near absence of high-frequency vibrational oscillations along the locus of Stokes-shifting peak-emission frequencies (compare Eqs. (3.51) and (3.52)). The observation by McClure *et al.* [1] that the Fourier amplitude of the 270-cm^{-1} vibrational quantum beat peaks broadly about 300 cm^{-1} (500 cm^{-1}) to the red (blue) of its null is consistent with the prediction of our analysis that the antiphased fundamental beats of an ω_f-vibration should be most prominent at probed frequencies ω_f above and below the slowly varying peak emission frequency.

Turner and coworkers have introduced a frequency-windowing procedure in the work-up of ultrafast transient-absorption data. [48] In this method, Fourier frequency components within a narrow range surrounding a putative vibrational frequency are isolated before reverting to the t_d-domain. A procedure of this kind could usefully be applied to testing features of vibrational oscillation amplitude and phase of the kind considered here.

Sign of the second derivative

Vibrational quantum beats were identified in Ref. 7 by Fourier analyzing the residual transient-transmission spectrum of PC577 obtained by subtracting probed-wavelength-dependent fits of the signal to a sum of two decaying exponentials. Before Fourier analysis, the residual delay traces were subject to a Heaviside frequency filter from 130 to 1000 cm^{-1}. This procedure eliminated a constant background and the noise above 1000 cm^{-1}, where the experimental setup lacked the time resolution necessary to observe oscillatory signal contributions.

Here, we briefly explore an alternative strategy for bringing quantum beats to light in transient-transmission data. Even small-amplitude beats are expected to produce sign changes in the *derivatives* of a spectrum with respect to inter-pulse delay. For instance, the second derivative should be negative in the vicinity of a peak or downward-curving shoulder in the signal and positive near a trough or upward-curving shoulder. Figure 30. shows a plot of the *sign* of the second derivative of the calculated SE signal at each probed frequency with respect to t_d—without background subtraction. Figure 31. shows similar plots of the sign of the second derivative for experimental transient-absorption signals from PC577 and methylene blue.[70] Finite-difference expressions for the second delay-derivative were used to make the plots in both Fig. 30. and Fig. 31.. The PC577 data—measured with identical 20-fs pump and probe pulses—were convolved with a Gaussian smoothing function of 25-fs FWHM to remove high-frequency noise and to produce evenly spaced data-points ($\Delta t_d = 5$ fs). The methylene blue data were convolved with a narrower Gaussian smoothing function of 20-fs FWHM due to the 16-fs pump and probe pulses used in the experiment, with data points every 2.5 fs. In both figures, abrupt changes in the sign of the second derivative at a given

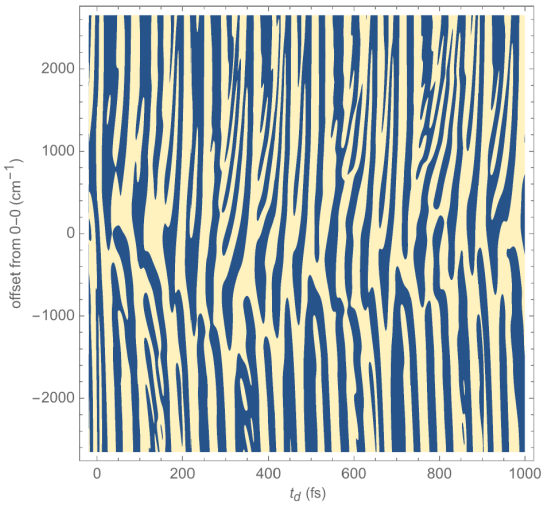

FIGURE 30. Vibrational quantum beats in calculated SE signal visualized by plotting the sign of the second derivative of the signal for fixed probed frequency with respect to t_d. Light (dark) represents negative (positive) second derivative, occurring in delay ranges of concave downward (upward) transient-transmission. Ordinate is offset of probed wavenumber from 0-0 in cm^{-1}.

delay in the vicinity of the instantaneous peak-emission frequency signify phase-flips in the vibrational quantum beats. The sensitivity of the second-derivative sign maps to the presence of small-amplitude oscillations and the phase of all contributing oscillations, promotes their use in detecting subtle features of the transient-absorption spectrum. Residual pulse chirp can be discerned through sloped or curving stripes in the sign map. Taking note of the differing ordinates of the two panels in Fig. 31., we observe that the slopes in both cases may suggest the presence of residual down-chirp in the incident probe pulses. Especially in the calculated SE signal of Fig. 14, an additional *fingering* is observed in the sign$[d^2(\Delta U_{SE})/dt_d^2]$ stripes at larger offsets from the evolving emission peak. By further elaboration of the analysis in the preceding subsection, we will show that this branching can be ascribed to overtones of individual vibrations or combinations between them.

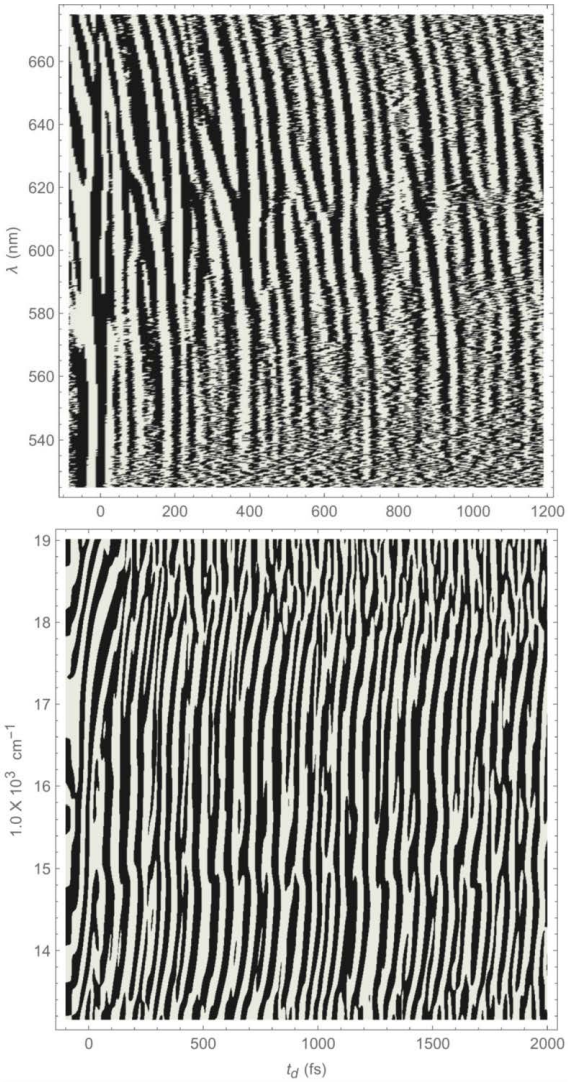

FIGURE 31. Vibrational quantum beats in measured transient-transmission spectra of PC577 and methylene blue visualized by plotting the sign of the second derivative of the signal for fixed probed frequency with respect to t_d. Light (dark) represents negative (positive) second derivative, occurring in delay ranges of concave downward (upward) transient-transmission. Ordinate in PC577 plot (top) is probed wavelength in nanometers, while that for the methylene blue data (bottom) is probed frequency in cm^{-1}.

A theoretical basis for some of these fingers can be sought in $\Delta U_{SE}^{(2)}$ and higher-order terms in Eq. (3.44). For example, we can isolate the terms giving rise to $2\omega_f$-overtones:

$$\Delta U_{SE,2\omega_f}^{(2)}(\bar{\omega}) \cong \frac{\delta_f^4}{2}\bar{\omega}F_u^2F_rF_r'p_{max}^3\theta(t_d)e^{-\Gamma t_d}$$
$$\times\int_0^\infty \frac{dt}{\sigma'}\, f'(t)e^{-t^2\chi_s'-\frac{\Gamma}{2}t-it(\bar{\omega}-\epsilon_s(t_d))-it^2\chi_s''(t_d)}$$
$$\times\left\{e^{2i\omega_f t_d}\left[e^{2i\omega_f t}-2e^{i\omega_f t}+1\right]+e^{-2i\omega_f t_d}\left[e^{-2i\omega_f t}-2e^{-i\omega_f t}+1\right]\right\}+\text{c.c.}\,. \qquad (3.53)$$

The contributions to Eq. (3.53) from the stationary phases at $\bar{\omega}-\epsilon_s(t_d)\simeq 0$ or $\pm\omega_f$ are not of immediate interest, because δ_f^4-terms in these probed-frequency ranges are small compared to $\Delta U_{SE}^{(0)}$ and $\Delta U_{SE}^{(1)}$. The overtone beats exhibit an additional resonance along the probed-frequency path $\bar{\omega}=\epsilon_s(t_d)\pm 2\omega_f$, where

$$\Delta U_{SE,2\omega_f}(\epsilon_s(t_d)\pm 2\omega_f) \approx \delta_f^4(\epsilon_s(t_d)\pm 2\omega_f)F_u^2F_rF_r'p_{max}^3\theta(t_d)e^{-\Gamma t_d}$$
$$\times\int_0^\infty \frac{dt}{\sigma'}\, f'(t)e^{-t^2\chi_s'-\frac{\Gamma}{2}t}\cos[2\omega_f t_d\mp t^2\chi_s''(t_d)]\,. \qquad (3.54)$$

Since $t^2\chi_s''(t_d)$ is small over most of the t_d range for $t\ <\ t_o$, these two signal contributions will tend to be in phase with each other. But the overtone beats along the blue-shifted path are favored by their larger $\bar{\omega}F_r'$. The emergence of overtone (and similar combination) oscillations along paths offset from emission resonance by the corresponding overtone or combination frequency can be a source for fingering of the sort seen in Fig. 30.. But overtones and combination bands must of course be distinguished from the fundamental quantum beats of higher-frequency modes, which could become visible at similar resonance offsets. The

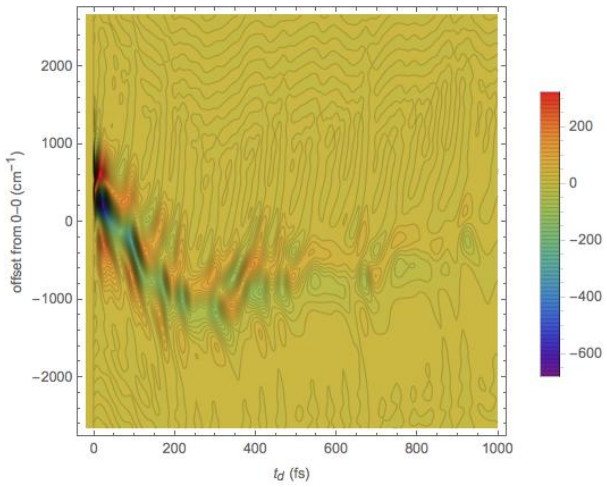

FIGURE 32. Contour plot of portion of $\Delta U_{SE}(\bar{\omega})$ that is second order in squared Franck-Condon displacements of the higher-frequency vibrations. Beat structure is generally higher in frequency than first-order portion depicted in bottom panel of Fig. 28. due to the presence of overtone and combination-band oscillations, which become prominent at probed frequencies offset from Stokes-shifting emission peak by plus or minus the corresponding doubled or summed vibrational frequencies, respectively.

experimental search for fingering due to overtones and combination bands should be facilitated by the application of broadband white-light probing. [47]

For the purpose of comparison to the bottom panel of Fig. 28., it is interesting to plot the full second-order term in Eq. (3.44). This second-order portion of the stimulated-emission signal is displayed in Fig. 32.. Vibrational oscillations in this signal contribution occur at notably higher frequencies than those seen in Fig. 28.. This feature of $\Delta U_{SE}^{(2)}$ is attributable to vibrational overtones and combinations to the red and especially to the blue of the time-evolving peak emission frequency visualized in the top panel of Fig. 28..

For the sake of completeness, the supplementary material[71] develops an alternative treatment of the fast-mode factor in the stimulated-emission overlap based on its decomposition in terms of vibrational eigenstates and eigenenergies.

Concluding Discussion

In its chapter devoted to resonant gratings, pump-probe, and hole-burning spectroscopy, Shaul Mukamel's comprehensive treatise [72] describes two theoretical approaches to ultrafast nonlinear optical spectroscopy: "The issue is whether to carry out all averagings over the matter degrees of freedom first, obtain the response functions, and then worry about the convolution with the fields, or to include the fields from the start and calculate the dynamics in terms of wavepackets, performing the trace over the relevant material coordinates only at the end of the calculation." While that work and several others [73, 74] give their main emphasis to the former approach, the formulation of transient-absorption spectroscopy developed in this paper—a revisitation of Mathies and coworkers' theoretical treatment using nonlinear response functions, but emphasizing their interpretation in terms of wave packets[8]—opts for the second strategy. Both frameworks are physically equivalent, or can be made so at any given level of approximation. The Hilbert-space, wave-packet picture spelled out here and used to elucidate several generic features of recently measured, high-quality broadband transient-absorption signals, is seen to facilitate certain computational and interpretive efficiencies which, while not strictly unique to this approach, nonetheless emerge from it in a logical and practical way.

Such broadband ultrafast transient-absorption spectroscopy signals [75] exhibit extensive vibronic structure in the form of vibrational quantum beats whose amplitude and phase vary in characteristic ways as a function of probed frequency and delay-time.[76, 77, 78, 79, 80] These features are of keen interest in their own right, as they provide detailed information on the coupling of vibrational and electronic molecular excitations. Their interest is amplified by the

influence that Franck-Condon-active molecular vibrations can exert over impulsive-stimulated Raman excitation of coherent nuclear motion in the electronic ground state, [81] intersystem-crossing dynamics through conical intersections, [48] and photosynthetic and other electronic excitation transport.[82, 83]

Spatially-resolved ultrafast transient-absorption spectroscopy has found recent utility in discerning the extent of structural and orientational heterogeneity in organic semiconducting thin films.[84] In another application to materials-related processes, Dawlaty and coworkers[85] have used broadband transient-*reflection* spectroscopy to reveal the ability of impulsive-Raman-driven phonons to modulate the electronic structure of quinhydrone.

In this report, we have used a simple model of the vibrational structure in the light-harvesting chromphores of PC577 [1, 86] to investigate some important aspects of the quantum-beat structure of transient-absorption signals. Starting from a wave-packet/pulse-propagator picture describing the short-pulse excitation and probing of an individual molecule, we have provided a comprehensive explanation for the common, striking observation of the antiphasing of the vibrational quantum beats that appear on opposite sides of the Stokes-shifting peak emission frequency in the stimulated-emission signal contribution. Our analysis applies even in the presence of several vibrational modes weakly coupled to the electronic transition.

A similar analysis would apply to the antiphasing of vibrational quantum beats on opposite sides of the peak absorption frequency appearing in the ground-state bleach signal component and originating from coherent nuclear motion in the electronic ground state, though the impulsive-Raman excitation of such ground-state motion was precluded here by the assumption of a sufficiently brief pump

pulse. It is worth noting in this connection that, while the SE signal takes the form of the expectation value of a certain Hermitian operator on the nuclear degrees of freedom in a first-order pump-generated nuclear wave packet evolving on the excited electronic potential surface, the GSB component involves the interference between a second-order pump-generated nuclear wave packet on the ground-state surface and a zeroth-order wave packet (i.e., the original stationary nuclear state).

The interpretation of transient-absorption data from PC577 [1] complements that from bacteriorhodopsin (BR_{568}) [8] in that observed vibrational quantum beats are ascribed primarily to the electronic excited state in the former and to the ground state in the latter. Pollard, *et al.* explained the absence of quantum beats in the stimulated-emission signal component of BR_{568} as a consequence of the rapid evacuation by its pump-induced nuclear wave packet in the excited state, along the route of the photochemical reaction coordinate, of the region in which the excited-to-ground-state difference potential lay within the spectral bandwidth of their 12-fs probe pulse.

Calculations on a 29-mode displaced-harmonic BR_{568} model [8] were carried out via numerical integration of the nonlinear response functions over the temporal envelopes of nonzero-duration pump and probe pulses. Because the spectrum of their probe pulse lay to the red of the peak absorption frequency of BR_{568}, it was not possible observe phase-flips between quantum beats to the blue and red of peak absorption. Some such antiphasing does appear to be present in Pollard's Fig. 9(d), which plots the impulsive Raman signal contribution (equivalent to our GSB term) that would be obtained with a hypothetical delta-function probe pulse.

In addition to quantum beats at vibrational fundamentals, our analysis considered the multiple-frequency contributions to the transient absorption signal

that should arise as signatures of vibrational overtones and combinations between modes of different frequency. These multiple-frequency beats are predicted to become prominent at larger offsets from the peak frequency, and their observation would therefore be facilitated by probing with a white-light source. [47]

Despite the fact that the calculations of Sec. 3.3 are carried out at zero temperature, our *derivation* and basic signal expressions are much more general. In order to validate this claim, recall that the inital state $|\psi_0\rangle$ in Eq. (3.9) is assumed to be an eigenstate of H_g—not necessarily the ground state—and note that this Hamiltonian could in principle be taken to govern both 'system' and 'environmental' nuclear degrees of freedom: the former would comprise the translational, orientational, and internal vibrational modes of a target chromophore together with the nuclear degrees of freedom of the solvent within a certain distance of that molecule, while the latter would consist of the solvent degrees of freedom of the rest of the surrounding medium. In this case, the electric-dipole matrix elements (B.1)-(B.4) determining the transient-absorption signal all have the form $\langle\psi_0|\hat{O}|\psi_0\rangle = \mathrm{Tr}_{env}\mathrm{Tr}_{sys}[\hat{O}\rho_0]$, with $\hat{O}$ being a nuclear operator and $\rho_0 = |\psi_0\rangle\langle\psi_0|$ being the *microcanonical* density operator corresponding to the system-plus-environment energy ϵ_0. Provided the system-environment boundary is set far enough away from the solvated chromophore that sound waves emanating from this molecule due to pulse-induced electronic transitions and the accompanying nuclear dynamics could not propagate to the boundary and back on the ultrashort timescale of a transient-absorption measurement (i.e., the observation time t and the inter-pulse delay t_d), the relevant nuclear operators $\hat{O} \cong \hat{O}_{sys} \otimes I_{env}$ pertain to the system alone. The reduced pulse propagators, in particular, take simplified forms such as $p^{(eg)} \cong p^{(eg)}_{sys} \otimes I_{env}$ to an excellent approximation as soon as the same

condition applies to the incident pulse duration. It follows that the signal dipole-elements obey $\langle\psi_0|\hat{O}|\psi_0\rangle = \mathrm{Tr}_{sys}[\hat{O}_{sys}\sigma_0]$, where $\sigma_0 = \mathrm{Tr}_{env}[\rho_0]$ is the *canonical* density operator of the system at a temperature T that is proportional to and easily determined from ϵ_0. [87] So the basic transient-absorption signal expression obtained by combining Eq. (3.28) with Eqs. (B.1)-(B.4) applies as written to a molecular system initially in equilibrium with a surrounding environment at nonzero temperature to which it is weakly coupled.

Bridge

This chapter has outlined the theory of transient absorption, and simulated an experimental signal from a simple model of the PC577 chromophore. Much of the theory laid out here may be used as is with our forthcoming perturbative formulation of FVB/GB to calculate transient absorption signals from condensed phased systems. Such a calculation would serve to probe the dynamics of the guest chromophore's vibrational coherence and its interaction with the bath. As the decoherence and energy dissipation processes remain challenging to simulate, the combination of the works described in the previous two chapters provides the possibility of further progress in this area. In chapter IV we go on to develop the theory of femtosecond stimulated Raman scattering which may as well be implemented with perturbative FVB/GB to simulated experimental spectra from interesting model systems.

CHAPTER IV

HOW FISSORS WORKS: OBSERVING VIBRATIONALLY ADIABATIC CONFORMATIONAL CHANGE THROUGH FEMTOSECOND STIMULATED RAMAN SPECTROSCOPY

This work was previously published in the Journal of Physical Chemistry A in April 2013. Jeffrey Cina began this work. Jeffrey Cina and Philip Kovac derived all analytic expression and performed the calculations separately. Jeffrey A. Cina wrote the paper and was the principle investigator during this work.

Introduction

Over the last decade, Mathies and co-workers have developed and tested a specialized version of pump/spectrally-resolved-probe-transmission spectroscopy termed femtosecond stimulated Raman spectroscopy (FSRS or "fissors") to monitor the response of high-frequency internal-molecular vibrations to slower—but still ultrafast—conformational motion. [88] The technique measures Raman gain in the power spectrum of a transmitted electronically nonresonant broadband probe pulse due to the simultaneous presence of a narrow-band pump. [14] Of particular interest is the variation of Raman gain in the vicinity of vibrational resonances associated with high-frequency modes due to their coupling to slower conformational motion, with the latter having been initiated by an earlier "actinic" pump pulse (in which case the conformational change occurs in an excited electronic state) or by impulsive stimulated Raman scattering (leading to low-frequency conformational motion in the electronic ground state).

Early applications used fissors to monitor the evolution of β-carotene's vibrational structure with femtosecond time resolution, [15] ultrafast intersystem crossing in the transition-metal complex $Ru(bpy)_3^{2+}$, [89] anharmonic coupling between low-frequency coherent bending motion in deuterio-chloroform and higher-frequency stretching vibrations, [90] and the photochemical isomerization of 11-*cis* retinal. [91] These initial studies inspired a number of additional applications and generalizations, [92], [93], [94] including recent FSRS studies of charge-transfer dynamics in 4-(dimethylamino)benzo-nitrile, [95] excited-state proton transfer from the photoacid pyranine, [96] exciton conformational dynamics of poly(3-hexylthiophene), [97] and hydrogen-bonding dynamics in photoactive yellow protein. [98]

The development of femtosecond stimulated Raman spectroscopy has been accompanied by the concurrent theoretical analysis of S.-Y. Lee and coworkers. [99] This theory, which is based on a treatment of the coupled propagation of pump and probe beams through an extended sample, [100] entertains both a phenomenological description within the Placzek approximation of the variation in medium polarizability with coherent motion of the targeted high-frequency vibration and a treatment of this variation by a quantum mechanical density-matrix theory. The quantum mechanical description explains how the ingenious choices of pump- and probe-pulse properties in an electronically nonresonant fissors experiment combine to reduce the nonlinear optical response to a single dominant term within a perturbative expansion. This foundational paper also generalized the formula for the induced medium polarization to include a nonstationary initial density matrix prepared by a prior actinic pulse.

A subsequent theoretical study [101] investigated situations more general than those arising in a "canonical" fissors experiment. That paper considered spectrally as well as temporally overlapping pump and probe pulses for which the roles of Raman and Stokes pulses can be interchanged and also the case in which the pump pulse is electronically resonant. Further classically-based [102] and quantum mechanical [103] treatments of FSRS experiments on $CDCl_3$ subject to impulsive stimulated Raman excitation studied the effects of cascades comprising two third-order processes on different molecules and found that these may typically dominate the contribution arising from the sought-after fifth-order signal from individual molecules. Mukamel and Biggs have provided an interesting discussion of the trade-off between time and frequency resolution in fissors experiments. [104]

The present paper was motivated by our desire to revisit the subject of femtosecond stimulated Raman spectroscopy from the basic perspective of time-dependent molecular quantum mechanics. We hoped to discover whether it is possible to formulate a theoretical description that starts from a molecular Hamiltonian augmented with time-dependent operators for interaction with given external fields of the pump and probe pulses, makes full use of the special temporal and spectral characteristics of those pulses in a fissors experiment, and makes minimal appeal to concepts of macroscopic electrodynamics and wave propagation. By way of an illustrative example, we also hope our treatment can set the stage for future first-principles simulations and interpretations of fissors-related signals starting from specified electronic potential-energy surfaces and transition-dipole functions. Although our analysis treats only the simplest case of a fissors signal from one representative model system, we believe that it can complement the existing, much more general analyses.

We start by specifying a model Hamiltonian for a system of two electronic levels and two nuclear degrees of freedom. A high-frequency mode stands for a vibration of the type whose Raman gain is the subject of a typical fissors experiment. The other, slower nuclear degree of freedom represents a conformational coordinate whose motion following an impulsive electronic or Raman transition one aims to track indirectly through its influence on the fissors signal observed in proximity to resonance with the high-frequency mode. In keeping with the typically large separation in frequency between the directly observable vibrational mode and the conformational coordinate, our treatment explicitly adopts an approximation of *vibrationally adiabatic conformational motion* that is analogous to the standard Born-Oppenheimer separation between fast electronic and slow nuclear degrees of freedom.

Using time-*independent* perturbation theory in a frame rotating at the center frequency of the Raman pump pulse, we find an expression for the molecular state as it follows the—also vibrationally adiabatically varying—field strength of the pump. In our example system, the impulsive onset of nonstationary conformational motion is effected by a rapid switch in the value of a certain conformational-potential parameter. In contrast with existing treatments, we account for the fact that this "actinic pulse" typically occurs *during* the prolonged pump pulse, rather than prior to it. The action of the probe pulse, which generates a fissors dipole specific to the nonlinear optical response of an individual molecule, is handled with time-dependent perturbation theory. The decay and eventual turn-off of the fissors dipole is governed by the trailing edge of the pump pulse and by vibrational decoherence—the loss of overlap between conformational wave packets propagating

on the slightly different adiabatic potential energy curves characteristic of the ground and first excited states of the intramolecular vibration.

A central result of our theory is an expression for the spectrally filtered, transmitted probe field as a function of monochrometer frequency within the bandwidth of the probe and the delay between the actinic potential-switch and the simultaneous arrival times of the pump and probe. A signal expression is derived by evaluating the change in energy of this transmitted field due to interference between the spectrally filtered, forward-propagated incident probe field and the field radiated by the third-order fissors dipole of an individual source molecule.

We report numerical simulations of fissors signals from our model system under two regimes that both honor a timescale separation between vibrational and conformational motion. In the first case, the mass associated with the conformation, though large enough to support the vibrationally adiabatic approximation, is small enough (and changes in conformation therefore fast enough) that the fissors signal consists of a central peak at a Raman shift characteristic of a conformationally averaged vibrational frequency and sidebands shifted by small-integer multiples of the transition frequencies between the various states superposed in the conformational wave packet. In a second case, we increase the conformational mass so as to decrease the conformational level-spacing to such a degree that the "conformational sidebands" merge with the central Raman-gain peak and to approach the vibrational frequency-tracking limit in which the Raman shift of this peak follows the local value of the conformational coordinate.

Theory

Model Hamiltonian

We consider a simple model system illustrative of those studied by fissors. It features two relevant electronic states and two nuclear degrees of freedom. The latter two consist of a Raman-active high-frequency vibrational mode and a slower conformational coordinate. The molecular Hamiltonian takes the form

$$H = |g\rangle\, H_g\, \langle g| + |e\rangle\, H_e\, \langle e| \ , \tag{4.1}$$

in which the nuclear Hamiltonian in the $j = g, e$ electronic state is

$$H_j = \frac{\hat{P}^2}{2M} + \frac{\hat{p}^2}{2m} + \frac{m\omega^2(\hat{Q})}{2}(\hat{q} - q_j(\hat{Q}))^2 + v_j(\hat{Q}) \ . \tag{4.2}$$

The hats in 4.2 denote quantum mechanical operators; the conformation-dependent vibrational frequency is taken to be

$$\omega(Q) = \omega - \frac{K}{m\omega l^4}Q^2 \ ; \tag{4.3}$$

the conformation-dependent equilibrium vibrational coordinate in the electronic ground state is

$$q_g(Q) = \frac{2K}{m\omega^2 l^3}Q^2 \ ; \tag{4.4}$$

that in the electronic excited state is shifted slightly to

$$q_e(Q) = q_g(Q) + \delta q \ ; \tag{4.5}$$

the conformational potential in the electronic ground state is assigned the form

$$\upsilon_g(Q) = \frac{4K}{5} - \Gamma Q - \frac{K}{l^2}Q^2 + \frac{5K}{6l^4}Q^4 \ ; \tag{4.6}$$

and the conformational potential in the electronic excited state is

$$\upsilon_e(Q) = \upsilon_g(Q) + \hbar\epsilon \ . \tag{4.7}$$

We choose the vibrational displacement parameter $\delta q = \sqrt{\hbar/2m\omega}$; this shift upon electronic excitation is responsible for vibrational Raman scattering. The conformational length parameter is assigned the value $l = 15\sqrt{\hbar/2m\omega}$. The coupling constant between vibrational and conformational degrees of freedom is $K = 4\hbar\omega$; and a conformational reduced mass, $M = 30m$—much larger than the vibrational reduced mass—ensures that the conformational motion will be vibrationally adiabatic (that is to say, conformational motion does not induce changes in the vibrational quantum number).[1] The (arbitrary) bare electronic excitation frequency is set to $\epsilon = 1500\omega$.

In the absence of an "external field" Γ, the conformational potentials υ_j are symmetric double wells, with minima at $Q = \pm l\sqrt{3/5}$. These two values of the conformational coordinate can be regarded as specifying equivalent "binding sites" on a substrate for a ligand of total mass M featuring an internal vibration

[1] A specific condition for the vibrational adiabaticity of conformational motion is that $\hbar \langle \bar{n}_j(Q) | \partial n_j(Q)/\partial Q \rangle$ for unequal $\bar{n}_j$ and n_j times the conformational speed P/M be much smaller in magnitude than a vibrational quantum. Using 4.4 and our chosen values for K and l, an estimate $\langle \bar{n}_j(Q) | \partial n_j(Q)/\partial Q \rangle \approx l^{-1}$ can be arrived at as the inverse of the conformational displacement needed to change the equilibrium vibrational coordinate by $q_{rms} = \sqrt{\hbar/2m\omega}$. The conformational trajectory shown in Fig. 35. suggests $P/M \approx l\omega/14\pi$, so the product described is of approximate size $\hbar\omega/44$ for the model system whose fissors signals are plotted in Figs. 35. and 36..

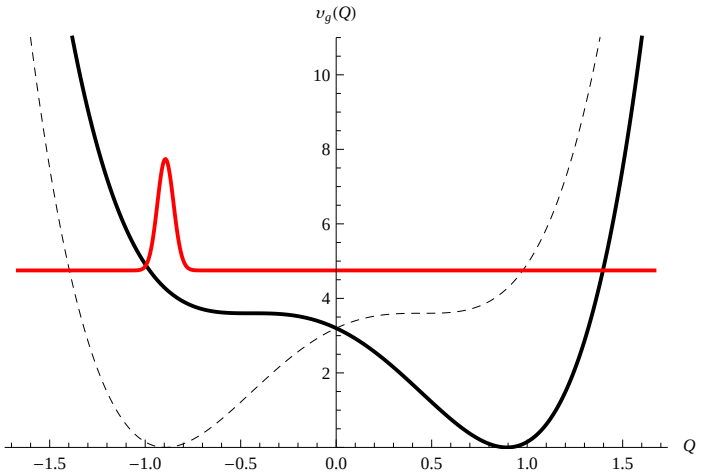

FIGURE 33. Dashed curve is bare conformational potential $v_g(Q)$ (for case $\Gamma = -\Gamma_\circ$) in units of $\hbar\omega$ as function of Q in units of l. Thick curve is the bare conformational potential after the potential flip (for case $\Gamma = \Gamma_\circ$). The red curve plots probability density associated with conformational wave packet at the end of the rapid potential flip at $t = \tau_f/2$ (see further, below).

of reduced mass m and frequency $\omega(Q)$. A positive (negative) value of Γ stabilizes conformations with $Q > 0$ ($Q < 0$). We shall use a rapid change in the value of this external field parameter to generate a nonstationary conformational wave packet (see below), but will primarily be interested in the dynamics of the model Hamiltonian for the fixed value $\Gamma_\circ = 4K/3\sqrt{5}l$, whose conformational potentials exhibit a single minimum at $Q = 2l/\sqrt{5}$ and an inflection point at $Q = -l/\sqrt{5}$ (see Fig. 33.).

We define vibrational Hamiltonians for a fixed value of the conformational coordinate by zeroing out the conformational kinetic energy in 4.2:

$$h_j(Q) = \frac{\hat{p}^2}{2m} + \frac{m\omega^2(Q)}{2}(\hat{q} - q_j(Q))^2 + v_j(Q) \ . \tag{4.8}$$

The vibrational eigenstates and eigenfrequencies obey

$$h_j(Q)|n_j(Q)\rangle = \hbar\epsilon_{jn}(Q)|n_j(Q)\rangle \ , \tag{4.9}$$

with

$$\hbar\epsilon_{jn}(Q) = \hbar\omega(Q)\left(n+\frac{1}{2}\right) + \upsilon_j(Q) \ . \tag{4.10}$$

Given the separation that is assumed to exist between the timescales of vibrational and conformational motion, the nuclear eigenstates, which obey

$$H_j|X_{jn\chi}\rangle = \left\{\frac{\hat{P}^2}{2M} + h_j(\hat{Q})\right\}|X_{jn\chi}\rangle = \hbar\mathcal{E}_{jn\chi}|X_{jn\chi}\rangle \ , \tag{4.11}$$

with eigenfrequencies $\mathcal{E}_{jn\chi}$, can be sought in the approximate form of *conformationally correlated products*,

$$|X_{jn\chi}\rangle \cong |n_j(\hat{Q})\rangle|\chi_{n_j}\rangle \ . \tag{4.12}$$

In 4.12 it is to be noted that $\hat{Q}$ is a Hermitian operator, rather than a coordinate variable. [2] Under this vibrationally adiabatic approximation, $\left\{\hat{P}^2/2M + h_j(\hat{Q})\right\}|X_{jn\chi}\rangle \cong$

$|n_j(\hat{Q})\rangle\left\{\hat{P}^2/2M + \hbar\epsilon_{jn}(\hat{Q})\right\}|\chi_{n_j}\rangle$, with the vibrational eigenenergy, 4.10, serving as a conformational potential energy operator. Note, in particular, that although $\upsilon_g(Q)$ is independent of the vibrational quantum number, the adiabatic potential energy curves $\hbar\epsilon_{g0}(Q)$ and $\hbar\epsilon_{g1}(Q)$ differ by $\omega(Q)$. In practice, we solve

[2] These states are not tensor products, but rather "sums" of tensor products: $|n(\hat{Q})\rangle|\chi\rangle = \int dQ|n(Q)\rangle|Q\rangle\langle Q|\chi\rangle$.

the resulting conformational Schrödinger equation,

$$\left\{ \frac{\hat{P}^2}{2M} + \hbar\epsilon_{jn}(\hat{Q}) \right\} |\chi_{n_j}\rangle = \hbar\mathcal{E}_{jn\chi}|\chi_{n_j}\rangle \ , \tag{4.13}$$

numerically on a discrete, one-dimensional position grid, and treat the dynamics by expanding the nonstationary conformational states in the bases $\{|\chi_{n_j}\rangle\}$ of conformational eigenstates.

To the molecular Hamiltonian of 4.1 is added an interaction with the time-dependent fields of contemporaneous pump and probe pulses:

$$H(t) = H(\Gamma(t)) - \hat{\mu}E(t) \ , \tag{4.14}$$

where $\hat{\mu} = \mu(|e\rangle\langle g| + |g\rangle\langle e|)$ and $E(t) = E_1(t) + E_2(t)$, with

$$E_I(t) = E_I f_I(t - t_d)\cos[\Omega_I(t - t_d) + \varphi_I] \ . \tag{4.15}$$

The pump-pulse envelope function is given by

$$f_1(t) = \begin{cases} \cos\left(\frac{\pi}{2\tau_1}(t + \tau_2)\right) & -\tau_1 - \tau_2 < t < -\tau_2 \\ 1 & -\tau_2 < t < \tau_2 \\ \cos\left(\frac{\pi}{2\tau_1}(t - \tau_2)\right) & \tau_2 < t < \tau_1 + \tau_2 \\ 0 & \text{otherwise} \end{cases} \ , \tag{4.16}$$

and the probe-pulse envelope is

$$f_2(t) = \begin{cases} \cos\left(\frac{\pi}{2\tau_2}t\right) & -\tau_2 < t < \tau_2 \\ 0 & \text{otherwise} \end{cases} \ . \tag{4.17}$$

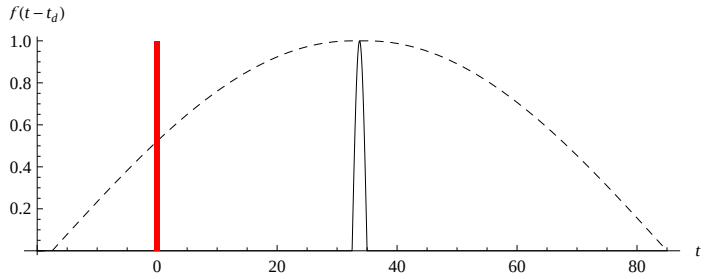

FIGURE 34. Pump (dashed) and probe (solid) envelope functions centered at t_d (here t_d is set to $33.75(2\pi/\omega)$) versus time in units of vibrational period $2\pi/\omega$. Red shaded area represents the duration of the potential flip (actinic pulse), which is centered at $t = 0$.

The center frequency of the pump is set well below electronic resonance, at $\Omega_1 = \epsilon - 4\omega$, and its duration parameter, $\tau_1 = 50(2\pi/\omega)$, is long enough that its bandwidth, $\sim 2\pi/\tau_1$, is slightly smaller than the conformationally-induced variation in the vibrational frequency, $\Delta\omega \approx K/m\omega l^2$. The probe pulse is red-shifted by about a vibrational quantum, with $\Omega_2 = \epsilon - 5\omega$, and is much shorter than the pump, with $\tau_2 = (5/4)(2\pi/\omega) \ll 2\pi/\Delta\omega$; its spectral bandwidth exceeds the range of variation in $\omega(Q)$, but is not so large as to overlap with that of the pump. The temporal envelopes of the pump and probe pulses are pictured in Fig. 34..

The external conformational-field parameter has been rendered time dependent in 4.14. It is made to switch rapidly from $\Gamma = -\Gamma_\circ$ to $+\Gamma_\circ$ at time-zero so as to flip the stable conformation from negative to positive Q. This field-flip initiates conformational motion and serves as an "actinic" pulse. The time dependence of the conformational-field parameter is accounted for by introducing a ramp function,

$$\rho_\tau(t) = \begin{cases} -1 & t < -\tau \\ t/\tau & -\tau < t < \tau \\ 1 & \tau < t \end{cases} , \tag{4.18}$$

and writing $\Gamma(t) = \Gamma_\circ \rho_{\tau_f/2}(t)$. The field-flip thereby takes place over a short interval, $\tau_f = 2\pi/\omega$, equal to one vibrational period, centered at $t = 0$. It is to be executed during the episode of increasing pump-pulse amplitude and to be completed before the advent of the probe, so the delay-time obeys $\tau_2 + \tau_f/2 < t_d < \tau_1 + \tau_2 - \tau_f/2$.

Fissors signal

The state of the system evolves according to $|\dot{\Psi}(t)\rangle = -i\hbar^{-1}H(t)|\Psi(t)\rangle$, starting from an initial condition $|\Psi(t_\circ < \tau_f/2 - \tau_1)\rangle = |g\rangle|0_g(\hat{Q})\rangle|\chi(t_\circ)\rangle$. The laser electric-field amplitudes are assumed to be sufficiently weak that we need only find perturbative solutions of the time-dependent Schrödinger equation of low order in E_1 and E_2. We may describe the nuclear wave packets in the ground and excited electronic states with the schematic expressions

$$\langle g|\Psi(t)\rangle = |\Phi_\circ\rangle + |11\rangle + |21\rangle + |12\rangle + |22\rangle + \ldots \tag{4.19}$$

and

$$\langle e|\Psi(t)\rangle = |1\rangle + |2\rangle + |211\rangle + |121\rangle + |112\rangle + \ldots \tag{4.20}$$

respectively. $|\Phi_\circ\rangle$ is the (time-dependent) vibrational-conformational amplitude in the electronic ground state unperturbed by the pump or probe fields. $|21\rangle$, for example, is the g-state nuclear wave packet generated by the sequential action of the temporally overlapping pump and probe pulses.

Fissors experiments are typically performed in a pump-probe geometry, with pulse-1 and pulse-2 laser beams crossed at a small angle in the sample volume. The measured quantity can be regarded as the spectral intensity in the direction of

probe propagation *with* minus that *without* the pump pulse. This difference turns out (see below) to be proportional, in any narrow frequency window, to the change in energy of the electromagnetic field due to interference between the *spectrally filtered transmitted probe field* and a *spectrally filtered fissors field*. The latter field arises from the radiation emitted by those contributions to the time-dependent dipole moment proportional to $E_1^2 E_2$ of each molecule in the illuminated volume. As the former field is of course proportional to E_2, the measured quantity goes as $E_1^2 E_2^2$ and is therefore bilinear in the pump- and probe-pulse intensities.

With reference to 4.19 and 4.20, we identify the portion of $\langle\Psi(t)|\hat{\mu}|\Psi(t)\rangle = 2\mu\mathrm{Re}\{\langle\Psi(t)|e\rangle\langle g|\Psi(t)\rangle\}$ proportional to $E_1^2 E_2$ as

$$\mu_{E_1^2 E_2}(t) = 2\mu\mathrm{Re}\{\langle 211|\Phi_\circ\rangle + \langle 121|\Phi_\circ\rangle + \langle 112|\Phi_\circ\rangle + \langle 2|11\rangle + \langle 1|12\rangle + \langle 1|21\rangle\} \ . \quad (4.21)$$

The bra in the first wave-packet overlap in curly brackets, $\langle 211|\Phi_\circ\rangle$, is generated by the upward action of the pump, the downward action of the pump, and the upward action of the probe. Because of the narrow bandwidth of the pump pulse, there is no opportunity here for vibrational resonance after the second action of the pump, and hence no contribution from this term to the Raman gain (increased intensity within the probe-pulse bandwidth at a frequency red-shifted from that of the pump by a vibrational frequency of the system). The bra in $\langle 121|\Phi_\circ\rangle$ involves two upward-going pump-induced transitions and therefore carries an optical phase factor $\exp\{2i\varphi_1\}$. Since the absolute phase of the pulses is not controlled in a fissors experiment, and can be regarded as varying randomly within a series of laser shots, this term averages to zero during signal accumulation. Neither the bra in $\langle 112|\Phi_\circ\rangle$ nor the ket in $\langle 2|11\rangle$ offers any opportunity for vibrational resonance, so

these terms cannot contribute to the Raman gain. The wave-packet overlap $\langle 1|12\rangle$ carries a non-surviving phase factor $\exp\{2i\varphi_1\}$ *and* lacks vibrational resonance.

In a macroscopic description of the radiated field a long distance from a sample containing many molecules, the fields arising from spatially distributed dipoles corresponding to the single-molecule sources $\langle 121|\Phi_\circ\rangle$ and $\langle 1|12\rangle$ would not be properly phase-matched to contribute to a signal beam in the direction of probe propagation. To further establish the connection with prior analyses, it can be pointed out that the wave-packet overlaps $\langle 211|\Phi_\circ\rangle$, $\langle 112|\Phi_\circ\rangle$, $\langle 2|11\rangle$, and $\langle 1|21\rangle$ correspond, respectively, to the IRS(II), IRS(I), SRS(II), and SRS(I) contributions to the third-order polarization described by Lee and co-workers.[101], [105]

Given the choices made for the center frequency and pulse duration of the pump and probe, the last overlap inside the curly brackets of 4.21 is the sole contributor to the Raman gain in a fissors experiment. It gives rise to the source dipole,

$$\mu_{FSRS}(t) = 2\mu \mathrm{Re}\{\langle 1|21\rangle\} \ , \tag{4.22}$$

which radiates a signal electric field given by

$$E_{FSRS}(\mathbf{R},t) \cong \frac{\Omega_2^2}{c^2 R}\mu_{FSRS}\left(t-\frac{R}{c}\right) \tag{4.23}$$

at points $\mathbf{R} = R\mathbf{n}$, with $R \gg 2\pi c/\Omega_2$, much farther from the molecule than the wavelength of the emitted light. [56], [3]

With the source field just obtained, we can calculate the *fissors signal*—the pump-induced change in the electromagnetic energy of the transmitted probe beam

[3]The single overlap retained in 4.22 corresponds to the "loop diagram" considered in Mukamel and Biggs' discussion of FSRS.[104]

within some narrow spectral range. Within a spectral window of width $\delta\omega$ centered at $\bar{\omega}$, the change in energy of the probe field due to the presence of the pump is

$$\begin{aligned}\Delta\mathcal{U}(\bar{\omega}) &= \frac{1}{4\pi}\int d^3R\ \{[E_2'(\mathbf{R},t)+E_{FSRS}'(\mathbf{R},t)]^2 - E_2'^2(\mathbf{R},t)\} \\ &\cong \frac{1}{2\pi}\int d^3R\ E_2'(\mathbf{R},t)E_{FSRS}'(\mathbf{R},t)\ ;\end{aligned} \tag{4.24}$$

the spectrally filtered fields are primed, and $E_2(\mathbf{R},t) = E_2 f_2(t-t_d(\mathbf{R}))\cos[\Omega_2(t-t_d(\mathbf{R}))+\varphi_2]$, with $t_d(\mathbf{R}) = t_d + Z/c$ (the probe being taken to propagate in the laboratory z-direction). A straightforward analysis consisting of Fourier transformation, spectral windowing, and inverse Fourier transformation shows that the spectrally filtered probe field can be written in the conventional carrier-wave/ envelope form as

$$E_2'(\mathbf{R},t) = E_2' f_2'(t-t_d(\mathbf{R}))\cos[\bar{\omega}(t-t_d(\mathbf{R}))+\varphi_2]\ , \tag{4.25}$$

where the ($\bar{\omega}$-dependent) amplitude is

$$E_2' = E_2\frac{2\tau_2\delta\omega}{\pi^2}\frac{\cos(\bar{\omega}-\Omega_2)\tau_2}{1-[2\tau_2(\bar{\omega}-\Omega_2)/\pi]^2}\ , \tag{4.26}$$

and the envelope function is

$$f_2'(t) = \frac{\sin(\delta\omega\, t/2)}{\delta\omega\, t/2}\ . \tag{4.27}$$

$E_2'(\mathbf{R},t)$ comprises frequency components ranging from $\bar{\omega}-\delta\omega/2$ to $\bar{\omega}+\delta\omega/2$ (and $-\bar{\omega}-\delta\omega/2$ to $-\bar{\omega}+\delta\omega/2$) and, concomitantly, wave-vector components in the z-direction from $\bar{\omega}/c-\delta\omega/2c$ to $\bar{\omega}/c+\delta\omega/2c$ (and $-\bar{\omega}/c-\delta\omega/2c$ to $-\bar{\omega}/c+\delta\omega/2c$). E_{FSRS}' in 4.24 can be replaced by E_{FSRS} itself, as only wave-vector components

of the unfiltered signal field within these prescribed ranges survive the spatial integration. We therefore omit spectral filtering of the fissors field and rewrite the signal expression as

$$\Delta\mathcal{U}(\bar{\omega}) = \frac{1}{2\pi}\int d^3R\ E_2'(\mathbf{R},t)E_{FSRS}(\mathbf{R},t)\ . \tag{4.28}$$

Like the bandwidth of the pump pulse, the monochrometer slit-width in a fissors experiment is typically chosen to be similar in size to the conformationally-induced variation in the vibrational frequency. In the numerial calculations reported here, we set $\delta\omega = 1.0\times10^{-2}\omega$, which is similar to the bandwidth of the pump and much smaller than that of the probe.

With 4.25 for the filtered probe field and 4.23 for the fissors field, the signal expression given in 4.28 becomes

$$\begin{aligned}\Delta\mathcal{U}(\bar{\omega}) &= \frac{E_2'\Omega_2^2}{2\pi c^2}\int d^3R\, f_2'\big(t-t_d-\tfrac{Z}{c}\big)\cos\big[\bar{\omega}\big(t-t_d-\tfrac{Z}{c}\big)+\varphi_2\big]\frac{\mu_{FSRS}(t-\frac{R}{c})}{R}\\ &= E_2'\frac{\Omega_2^2}{c^2}\int_0^\infty R\,dR\ \mu_{FSRS}\left(t-\frac{R}{c}\right)\ I(R)\ .\end{aligned} \tag{4.29}$$

In the last member of 4.29, we have switched to spherical polar coordinates and defined

$$I(R) = \int_0^\pi d\theta\sin\theta\ f_2'\left(t-t_d-\frac{R}{c}\cos\theta\right)\cos\left[\bar{\omega}(t-t_d-\frac{R}{c}\cos\theta)+\varphi_2\right]\ . \tag{4.30}$$

This integral can be evaluated by parts and, with the recognition that $\dot{f}_2'/\bar{\omega} \ll f_2'$, reduces to $I \cong -(c/\bar{\omega}R)\, f_2'(t-t_d-R/c)\sin[\bar{\omega}(t-t_d-R/c)+\varphi_2]$. Hence, using $\bar{\omega}\approx\Omega_2$ in the prefactor for monochrometer settings within the probe bandwidth and changing the integration variable from R to $t' = t - R/c$ (and then dropping

the prime), we arrive at a working expression for the fissors signal as minus the imaginary part of a windowed Fourier transform of the fissors dipole:

$$\Delta\mathcal{U}(\bar{\omega}) = -E_2'\Omega_2 \int dt\, \mu_{FSRS}(t)\, f_2'(t-t_d) \sin[\bar{\omega}(t-t_d)+\varphi_2] \ . \tag{4.31}$$

The time integral goes from early to late. Although the filtered-probe envelope extends from about $t_d - 5.57/\delta\omega$ to $t_d + 5.57/\delta\omega$, it will be seen below that the fissors dipole does not turn on until the beginning of the *unfiltered* probe pulse at $t_d - \tau_2$.

Fissors dipole

The set-up for numerical evaluation of the fissors signal, 4.31, remains to be completed by describing a concrete procedure for calculating the requisite dipole moment contribution given by 4.22. In each of the finite intervals

I	$t_\circ < t < t_d - \tau_1 - \tau_2$	before advent of pump
II	$t_d - \tau_1 - \tau_2 < t < -\tau_f/2$	during pump, before potential flip
III	$-\tau_f/2 < t < \tau_f/2$	during potential flip
IV	$\tau_f/2 < t < t_d - \tau_2$	after potential flip, before probe
V	$t_d - \tau_2 < t < t_d + \tau_2$	during probe
VI	$t_d + \tau_2 < t < t_d + \tau_1 + \tau_2$	after probe, before pump ends

(4.32)

we need at most the contribution to the e-state amplitude linear in E_1 and the g-state amplitude through the term bilinear in E_1 and E_2 with the former field having acted first.

An essential feature of fissors experiments is the elongated nature of the pump pulse, whose envelope (given by 4.16)—like the conformational coordinate—varies slowly on the vibrational timescale. The slow variation of $f_1(t)$ motivates a second adiabatic approximation, for which the stage can be set by transforming to a rotating frame. We define $|\Psi_R(t)\rangle = R(t)|\Psi(t)\rangle$, where

$$R(t) = e^{i\Omega_1(t-t_d)|e\rangle\langle e|} \ . \tag{4.33}$$

The time-dependent Schrödinger equation in the rotating frame is found to be $|\dot{\Psi}_R\rangle = -i\hbar^{-1}H_R(t)|\Psi_R\rangle$, subject to the initial condition $|\Psi_R(t_\circ)\rangle = |\Psi(t_\circ)\rangle$, with

$$H_R(t) \cong \frac{\hat{P}^2}{2M} + H_1\left(f_1(t-t_d), \hat{Q}, \Gamma(t)\right) + H_2(t) \ ; \tag{4.34}$$

$$\begin{aligned} H_1(f, Q, \Gamma) = {} & |g\rangle h_g(Q,\Gamma)\langle g| + |e\rangle\left(h_e(Q,\Gamma) - \hbar\Omega_1\right)\langle e| \\ & -\frac{\mu E_1}{2} f\left(|e\rangle e^{-i\varphi_1}\langle g| + |g\rangle e^{i\varphi_1}\langle e|\right) \ ; \end{aligned} \tag{4.35}$$

$$H_2(t) = -\frac{\mu E_2}{2} f_2(t-t_d)\,|g\rangle e^{i(\Omega_2-\Omega_1)(t-t_d)+i\varphi_2}\langle e| + H.c. \tag{4.36}$$

The approximate equality in 4.34 reflects rotating-wave approximations in the definitions of 4.35 and 4.36, which are supported by the center frequency and bandwidth of the pump and probe pulses in a fissors experiment. The initial molecular state is taken to be the electronic, vibrational, and conformational ground state with $\Gamma(t_\circ) = -\Gamma_\circ$: $|\Psi_R(t_\circ)\rangle = |g\rangle|X_{g00}(-\Gamma_\circ)\rangle = |g\rangle|0_g(\hat{Q})\rangle|0_{0_g}(-\Gamma_\circ)\rangle$. This eigenstate only acquires a phase during interval I, so that by the beginning of interval II, $|\Psi_R(t_d-\tau_1-\tau_2)\rangle = \exp\{-i\mathcal{E}_{g00}(t_d-\tau_1-\tau_2-t_\circ)\}|g\rangle|0_g(\hat{Q})\rangle|0_{0_g}(-\Gamma_\circ)\rangle$.

As the pump-field amplitude grows in during intervals II, III, and IV, the state's evolution obeys

$$|\dot{\Psi}_R\rangle = -i\hbar^{-1}\left\{\frac{\hat{P}^2}{2M} + H_1\left(f_1(t-t_d),\hat{Q},\Gamma(t)\right)\right\}|\Psi_R\rangle \ . \tag{4.37}$$

Because the bandwidth $2\pi/\tau_1$ and the Rabi frequency $\mu E_1/2\hbar$ are smaller than the offset $\epsilon - \Omega_1$, and the parts of H_1 proportional to $\Gamma(t)$ are electronically and vibrationally diagonal, *the vibronic state in the rotating frame follows* $f_1(t-t_d)$ *as well as* Q *adiabatically*:

$$|\Psi_R(t)\rangle = |\zeta(f_1(t-t_d),\hat{Q})\rangle|\chi(t)\rangle \ , \tag{4.38}$$

where

$$H_1(f,Q,\Gamma)|\zeta(f,Q)\rangle = \hbar\epsilon_\zeta(f,Q,\Gamma)|\zeta(f,Q)\rangle \ . \tag{4.39}$$

Specifically, $|\zeta(f,Q)\rangle$ is the eigenket of $H_1(f,Q,\Gamma)$ that reduces to $|g\rangle|0_g(Q)\rangle$ as f goes to zero. Here, we need an expansion of the vibronic eigenstate only through first order in E_1, which is given by time-independent perturbation theory as [4]

$$|\zeta(f,Q)\rangle \cong |g\rangle|0_g(Q)\rangle + |e\rangle\frac{\mu E_1}{2\hbar}fe^{-i\varphi_1}\sum_{n_e}\frac{|n_e(Q)\rangle\langle n_e(Q)|0_g(Q)\rangle}{\epsilon_{n_e}(Q,\Gamma)-\epsilon_{0_g}(Q,\Gamma)-\Omega_1} \ . \tag{4.40}$$

We also need the vibronic eigenenergy, given *through* first order in E_1 by

$$\hbar\epsilon_\zeta(f,Q,\Gamma) \cong \langle 0_g(Q)|\langle g|H_1(f,Q,\Gamma)|g\rangle|0_g(Q)\rangle = \hbar\epsilon_{0_g}(Q,\Gamma) \ . \tag{4.41}$$

[4]The notation is consistent, as the Γ-dependence cancels on the right-hand side.

The time development of the conformational wave packet during the II-III-IV episode can be found from

$$\begin{aligned}\langle\zeta(f_1(t-t_d),\hat{Q})|\dot{\Psi}_R(t)\rangle &= \langle\zeta|\dot{\zeta}\rangle|\chi\rangle + \langle\zeta|\zeta\rangle|\dot{\chi}\rangle \\ &= -i\hbar^{-1}\langle\zeta|\left\{\hat{P}^2/2M + H_1(f_1(t-t_d),\hat{Q},\Gamma(t))\right\}|\zeta\rangle|\chi\rangle \ .\end{aligned} \tag{4.42}$$

$\langle\zeta|\dot{\zeta}\rangle = \mathcal{O}(E_1^2) \cong 0$ for our purposes, [5] so we find

$$|\dot{\chi}\rangle = -i\hbar^{-1}\left\{\hat{P}^2/2M + \hbar\epsilon_{0_g}(\hat{Q},\Gamma(t))\right\}|\chi\rangle \ , \tag{4.43}$$

through first order in the pump-pulse electric field. During the entire episode of amplitude growth of the pump pulse—including the abrupt potential flip—the conformational wave packet continues to evolve under a Hamiltonian for the electronic and vibrational ground state. By the end of interval IV, when the pump-pulse reaches its maximum amplitude,

$$|\Psi_R(t_d-\tau_2)\rangle = |\zeta(1,\hat{Q})\rangle|\chi(t_d-\tau_2)\rangle \ , \tag{4.44}$$

whose conformational wave packet is

$$|\chi(t_d-\tau_2)\rangle = u_0(t_d-\tau_2-\tau_f/2,\Gamma_\circ)v(\tau_f)u_0(-\tau_f/2-t_\circ,-\Gamma_\circ)|0_{0_g}(-\Gamma_\circ)\rangle \ . \tag{4.45}$$

In this expression, $u_0(t,\Gamma) = \exp\{-it[\hat{P}^2/2M\hbar + \epsilon_{0_g}(\hat{Q},\Gamma)]\}$ is the propagator for conformational evolution on the lowest vibronic potential energy curve with

[5] It is readily seen that in fact $\langle\zeta|\dot{\zeta}\rangle = 0$ to all orders, by a slight adaptation of an argument given in Berry, M. V. Quantal phase-factors accompanying adiabatic changes. Proc. R. Soc. London A **1984**, *392*, 45-57.

external field Γ, and $v(\tau_f)$ is the conformational evolution operator during the potential flip of interval III. In practice, we divide III into several tens of time slices during each of which $\Gamma(t)$ remains sensibly constant, express the conformational propagator during each slice as a Trotter product in a discrete conformational position representation, and matrix-multiply the propagators for successive time-slices to obtain $v(\tau_f)$ and store it for repeated use.

During the interval (V) of probe-pulse action, the amplitude of the pump remains constant, and $|\dot{\Psi}_R\rangle = -i\hbar^{-1}\{H_R(t_d - \tau_2) + H_2(t)\}|\Psi_R\rangle$. We make an additional, interaction-picture transformation,

$$|\tilde{\Psi}_R\rangle = e^{i\frac{t-t_d}{\hbar}H_R(t_d-\tau_2)}|\Psi_R\rangle \ , \tag{4.46}$$

noting that $H_R(t_d - \tau_2)$ is a specific, time-independent Hamiltonian. This rotating-frame/interaction-picture state obeys $|\dot{\tilde{\Psi}}_R\rangle = -i\hbar^{-1}\tilde{H}_2(t)|\tilde{\Psi}_R\rangle$, with

$$\begin{aligned}
\tilde{H}_2(t) &= e^{i\frac{t-t_d}{\hbar}H_R(t_d-\tau_2)}H_2(t)e^{-i\frac{t-t_d}{\hbar}H_R(t_d-\tau_2)} \\
&\cong e^{i\frac{t-t_d}{\hbar}H_1(1,\hat{Q},\Gamma_\circ)}e^{i(t-t_d)\frac{\hat{P}^2}{2M\hbar}}H_2(t)e^{-i(t-t_d)\frac{\hat{P}^2}{2M\hbar}}e^{-i\frac{t-t_d}{\hbar}H_1(1,\hat{Q},\Gamma_\circ)} \\
&= e^{i\frac{t-t_d}{\hbar}H_1(1,\hat{Q},\Gamma_\circ)}H_2(t)e^{-i\frac{t-t_d}{\hbar}H_1(1,\hat{Q},\Gamma_\circ)} \ ,
\end{aligned} \tag{4.47}$$

and an initial condition $|\tilde{\Psi}_R(t_d - \tau_2)\rangle = \exp\{-i(\tau_2/\hbar)H_R(t_d - \tau_2)\}|\Psi_R(t_d - \tau_2)\rangle \cong |\zeta(1,\hat{Q})\rangle u_0(t_d - \tau_f/2, \Gamma_\circ)v(\tau_f)u_0(-\tau_f/2 - t_\circ, -\Gamma_\circ)|0_{0_g}(-\Gamma_\circ)\rangle$. In 4.47, we have used the fact that the probe duration is much less than the characteristic timescale of conformational motion to make a *semiclassical Franck-Condon approximation* by neglecting the noncommutation of $\hat{P}^2/2M$ and

$H_1(1,\hat{Q},\Gamma_\circ)$. Because H_2 is a purely electronic operator, it commutes with the conformational kinetic energy, leading to a further simplification.

Particular matrix elements of $\tilde{H}_2(t)$ may vary slowly enough to survive integration over time from $t_d - \tau_2$ to $t \leq t_d + \tau_2$ and make a non-negligible contribution (of first order in E_2, which is all we need) to

$$|\tilde{\Psi}_R(t)\rangle = \left\{1 - \frac{i}{\hbar}\int_{t_d-\tau_2}^{t} d\tau\, \tilde{H}_2(\tau)\right\} |\tilde{\Psi}_R(t_d - \tau_2)\rangle \ . \tag{4.48}$$

If we identify

$$|\zeta'(f,Q)\rangle \cong |g\rangle|1_g(Q)\rangle + |e\rangle\frac{\mu E_1}{2\hbar} f e^{-i\varphi_1} \sum_{n_e} \frac{|n_e(Q)\rangle\langle n_e(Q)|1_g(Q)\rangle}{\epsilon_{n_e}(Q,\Gamma) - \epsilon_{1_g}(Q,\Gamma) - \Omega_1} \tag{4.49}$$

as the eigenket of $H_1(f,Q,\Gamma)$ that reduces to $|g\rangle|1_g(Q)\rangle$ as $f \to 0$, and

$$\epsilon_{\zeta'}(f,Q,\Gamma) \cong \epsilon_{1_g}(Q,\Gamma) = \epsilon_{0_g}(Q,\Gamma) + \omega(Q) \tag{4.50}$$

as the corresponding eigenfrequency (compare with 4.40 and 4.41), then the only element contributing in 4.48 in the present instance is

$$\langle\zeta'(1,\hat{Q})|\tilde{H}_2(\tau)|\zeta(1,\hat{Q})\rangle \cong -\frac{\mu^2 E_1 E_2}{4\hbar} f_2(\tau - t_d) e^{i\Delta(\hat{Q})(\tau - t_d) + i\varphi_2 - i\varphi_1} \alpha_{10}(\hat{Q}) \ . \tag{4.51}$$

Here, $\Delta(Q) = \omega(Q) + \Omega_2 - \Omega_1$, and

$$\alpha_{10}(Q) = \sum_{n_e} \frac{\langle 1_g(Q)|n_e(Q)\rangle\langle n_e(Q)|0_g(Q)\rangle}{\epsilon_{n_e}(Q,\Gamma_\circ) - \epsilon_{0_g}(Q,\Gamma_\circ) - \Omega_1} \tag{4.52}$$

specifies an element of the conformational-coordinate-dependent Raman tensor. The Hamiltonian matrix element of 4.51 connects the e-state component of $|\zeta\rangle$ to the vibrationally excited g-state component of $|\zeta'\rangle$. [6]

Evaluation of 4.48 using

$$\begin{aligned} J(t-t_d,\Delta) &= \int_{t_d-\tau_2}^{t} d\tau f_2(\tau-t_d)e^{i(\tau-t_d)\Delta} \\ &= -\frac{i}{2}\left\{\frac{e^{i(t-t_d)(\Delta+\pi/2\tau_2)}}{\Delta+\pi/2\tau_2}+\frac{e^{i(t-t_d)(\Delta-\pi/2\tau_2)}}{\Delta-\pi/2\tau_2}\right\}-\frac{\pi}{2\tau_2}\frac{e^{-i\tau_2\Delta}}{\Delta^2-(\pi/2\tau_2)^2} \end{aligned} \tag{4.53}$$

and reversion to the simple rotating frame yield

$$\begin{aligned} |\Psi_R(t)\rangle &= |\zeta(1,\hat{Q})\rangle u_0(t-t_d,\Gamma_\circ)|\chi(t_d)\rangle \\ &\quad + |\zeta'(1,\hat{Q})\rangle\frac{\mu^2E_2E_1}{4\hbar^2}e^{i\varphi_2-i\varphi_1}u_1(t-t_d,\Gamma_\circ)\gamma(t-t_d,\hat{Q})\alpha_{10}(\hat{Q})|\chi(t_d)\rangle\ . \end{aligned} \tag{4.54}$$

In 4.54 we have introduced the unperturbed conformational wave packet at the pulse-center,

$$|\chi(t_d)\rangle = u_0(t_d-\tau_f/2,\Gamma_\circ)v(\tau_f)u_0(-\tau_f/2-t_\circ,-\Gamma_\circ)|0_{0_g}(-\Gamma_\circ)\rangle\ , \tag{4.55}$$

the turn-on function, $\gamma(t,Q) = iJ(t,\Delta(Q))$ (compare to 4.53), [7] and the propagator for conformational motion on the 1_g vibronic potential curve, $u_1(t,\Gamma) = \exp\{-it[\hat{P}^2/2M\hbar+\epsilon_{1_g}(\hat{Q},\Gamma)]\}$.

It would be adequate for present purposes to replace $|\zeta'(1,\hat{Q})\rangle$ in 4.54 with $|g\rangle|1_g(\hat{Q})\rangle$. By the end of the probe pulse, the molecular state $|\Psi_R(t_d+\tau_2)\rangle$ has

[6] We neglect a nonresonant contribution to this element that oscillates at frequencies $\omega(Q)+\Omega_1-\Omega_2 \approx 2\omega > 2\pi/\tau_2$ and connects the g-state component of $|\zeta\rangle$ to the vibrationally excited e-state component of $|\zeta'\rangle$.

[7] Note that $\gamma(-\tau_2,Q) = 0$, $\gamma(0,Q) = \frac{\Delta(Q)-(i\pi/2\tau_2)e^{-i\tau_2\Delta(Q)}}{\Delta^2(Q)-(\pi/2\tau_2)^2}$, and $\gamma(\tau_2,Q) = -\frac{i\pi}{\tau_2}\frac{\cos\tau_2\Delta(Q)}{\Delta^2(Q)-(\pi/2\tau_2)^2}$ at the beginning, middle, and end of the probe pulse, respectively.

acquired its maximal 1_g-amplitude due to permanent Raman population of the vibrationally excited state.

During interval VI the pump-pulse amplitude makes a slow decline, during which the evolution is governed by 4.37 with $\Gamma(t) = \Gamma_\circ$. The vibronic states $|\zeta(f_1(t-t_d),\hat{Q})\rangle$ and $|\zeta'(f_1(t-t_d),\hat{Q})\rangle$ cling to the instantaneous value of the f_1-envelope and the conformational wave packet accompanying each of these moves adiabatically. The molecular state,

$$|\Psi_R(t)\rangle = |\zeta(f_1(t-t_d),\hat{Q})\rangle u_0(t-t_d,\Gamma_\circ)|\chi(t_d)\rangle + |\zeta'(f_1(t-t_d),\hat{Q})\rangle \frac{\mu^2 E_2 E_1}{4\hbar^2} e^{i\varphi_2 - i\varphi_1} u_1(t-t_d,\Gamma_\circ)\gamma(\tau_2,\hat{Q})\alpha_{10}(\hat{Q})|\chi(t_d)\rangle \ , \quad (4.56)$$

differs from 4.54 only in the first argument of the two vibronic kets becoming explicitly time-dependent and $\gamma(\tau_2,\hat{Q})$ replacing $\gamma(t-t_d,\hat{Q})$. These two formulas can be combined with the help of the ramp function defined in 4.18:

$$|\Psi_R(t)\rangle = |\zeta(f_1(t-t_d),\hat{Q})\rangle u_0(t-t_d,\Gamma_\circ)|\chi(t_d)\rangle + |\zeta'(f_1(t-t_d),\hat{Q})\rangle \frac{\mu^2 E_2 E_1}{4\hbar^2} e^{i\varphi_2 - i\varphi_1} u_1(t-t_d,\Gamma_\circ)\gamma(\tau_2\rho_{\tau_2}(t-t_d),\hat{Q})\alpha_{10}(\hat{Q})|\chi(t_d)\rangle \ . \quad (4.57)$$

This expression is valid during both intervals V and VI, and can be transformed back to the nonrotating frame to obtain $|\Psi(t)\rangle = R^\dagger(t)|\Psi_R(t)\rangle$.

According to the analysis preceding 4.22, the portion of $\langle g|\Psi\rangle$ relevant for calculating the fissors dipole is

$$|21\rangle = |1_g(\hat{Q})\rangle F_1 F_2 e^{i\varphi_2 - i\varphi_1} u_1(t-t_d,\Gamma_\circ)\gamma(\tau_2\rho_{\tau_2}(t-t_d),\hat{Q})\alpha_{10}(\hat{Q})|\chi(t_d)\rangle \ , \quad (4.58)$$

while the relevant portion of $\langle e|\Psi\rangle$ is

$$|1\rangle = F_1 f_1(t-t_d)e^{-i\Omega_1(t-t_d)-i\varphi_1}\sum_{n_e}\frac{|n_e(\hat{Q})\rangle\langle n_e(\hat{Q})|0_g(\hat{Q})\rangle}{\epsilon_{n_e}(\hat{Q},\Gamma_\circ)-\epsilon_{0_g}(\hat{Q},\Gamma_\circ)-\Omega_1}u_0(t-t_d,\Gamma_\circ)|\chi(t_d)\rangle\ , \tag{4.59}$$

where $F_I = \mu E_I/2\hbar$. Hence, according to 4.22, the fissors dipole is given by

$$\mu_{FSRS}(t) = 2\mu F_2 F_1^2 f_1(t-t_d)\mathrm{Re}\left\{e^{i\Omega_1(t-t_d)+i\varphi_2}\right.$$
$$\left.\times\ \langle\chi(t_d)|u_0^\dagger(t-t_d,\Gamma_\circ)\alpha_{10}^\dagger(\hat{Q})u_1(t-t_d,\Gamma_\circ)\gamma(\tau_2\rho_{\tau_2}(t-t_d),\hat{Q})\alpha_{10}(\hat{Q})|\chi(t_d)\rangle\right\}\ . \tag{4.60}$$

This dipole can be seen to turn on during the probe pulse (via γ); its subsequent decrease follows the trailing edge of the pump envelope f_1 combined with the loss of overlap between the conformational bra and ket due to the differing evolution under u_0 and u_1 (that is to say, vibrational dephasing, see Figs. 35. and 37. below). This expression for μ_{FSRS}, along with 4.31 for the fissors signal, is the central theoretical finding of the present work.[8]

4.31 and 4.60 are more general than the specific model Hamiltonian and the form of the pump and probe pulses for which they have been derived. The derivations make use only of the qualitative features of that Hamiltonian and those pulses. According to these formulas, the fissors signal is directly calculable from—and thereby reports upon—the electronically and vibrationally adiabatic evolution of the conformational wave packet $|\chi(t_d)\rangle$.

[8]That 4.60 reduces the fissors dipole to a measured quantity dependent only on the conformational state of the system can be emphasized by writing it as the expectation value with respect to the wave packet $|\chi(t_d)\rangle$ of the purely conformational Hermitian operator $\mu F_2 F_1^2 f_1(t-t_d)e^{i\Omega_1(t-t_d)+i\varphi_2}u_0^\dagger(t-t_d,\Gamma_\circ)\alpha_{10}^\dagger(\hat{Q})u_1(t-t_d,\Gamma_\circ)\gamma(\tau_2\rho_{\tau_2}(t-t_d),\hat{Q})\alpha_{10}(\hat{Q}) + H.c.$ The signal at frequency $\bar{\omega}$ given by 4.61 can be similarly transcribed as a conformational expectation value.

Because u_1 in 4.60 varies at the frequency of a singly-excited vibration, while u_0 varies at only conformational frequencies, the fissors dipole has components in a narrow range about $\sim \Omega_1 - \omega$; frequencies in a broader range resulting from the abrupt, probe-induced turn-on are overwhelmed by those in this narrower range due to the long life ($\lesssim \tau_1$) of the dipole. An apparent need to use a very small time-step δt in numerically evaluating the fissors-signal integral of 4.31 in order to catch the optical-frequency oscillations of μ_{FSRS} and the filtered probe field is obviated by a rotating-wave approximation to their product, which yields

$$\Delta\mathcal{U}(\bar{\omega}) = E_2'\Omega_2\mu F_2 F_1^2 \,\mathrm{Im}\int dt\, f_2'(t-t_d) f_1(t-t_d) e^{i(\Omega_1-\bar{\omega})(t-t_d)}$$
$$\times \langle\chi(t_d)|u_0^\dagger(t-t_d,\Gamma_\circ)\alpha_{10}^\dagger(\hat{Q})u_1(t-t_d,\Gamma_\circ)\gamma(\tau_2\rho_{\tau_2}(t-t_d),\hat{Q})\alpha_{10}(\hat{Q})|\chi(t_d)\rangle \ . \quad (4.61)$$

The integrand now varies at conformational frequencies, so the increment δt need only be short on the corresponding timescale. [9]

Results and Discussion

Signal calculations

The expectation value of the conformational coordinate following the rapid flip at time zero of the conformational potential from one having a single miniumum at $Q = -2l/\sqrt{5}$ to one having a miniumum at $Q = 2l/\sqrt{5}$ is shown in the upper panel of Fig. 35.. The conformational wave packet generated by the potential flip (see Fig. 33.) originates from the ground state of the system with $\Gamma = -\Gamma_\circ$ and becomes a linear superposition comprising roughly the 70^{th} through 90^{th} conformational eigenstates in the 0_g vibrational level of the system with

[9] The phase φ_2 vanishes from this expression, as it should.

$\Gamma = \Gamma_\circ$. The ~ 0.035-$\hbar\omega$ spacing of levels in this superposition is consistent with the observed round-trip time of about 28 vibrational periods. The conformational wave packet can be seen to move more rapidly in the positive-Q than the negative-Q region.

The pulse delays for which fissors spectra are presented are $t_d = 1.75, 8.25, 14.75, 20.75$ and 28.75 times $2\pi/\omega$, whose average conformational coordinates are -0.813l, 0.002l, 1.268l, 0.037l, and -0.816l, respectively. The first of these fissors signals, for the earliest admissible time delay, is plotted in the bottom panel of Fig. 35.. It consists of a strong central peak at a Raman shift corresponding to the vibrational frequency $\omega(Q)$ motionally averaged over the whole accessible range of conformational coordinate values along with weaker sidebands separated from the central peak by various frequency differences between nearby eigenstates contributing to the conformational wave packet. Also shown, in the middle panel of Fig. 35., is the magnitude of the fissors dipole as a function of time for the case $t_d = 1.75(2\pi/\omega)$.

At the second through fifth delay-times, whose fissors signals are plotted in Fig. 36., the central Raman peak remains largely unchanged while the sideband structure varies on the conformational timescale. In particular, the structure of the conformational sidebands at the fifth delay, corresponding to a near round-trip in $\langle Q(t) \rangle$, is seen approximately to recapitulate that of the first delay shown in Fig. 35..

The conditions of validity for the vibrationally adiabatic approximation to conformational motion are comfortably met by the molecular parameters we have chosen. Because of the low dimensionality of nuclear motion in our model, it is possible to check the accuracy of this approximation directly. By

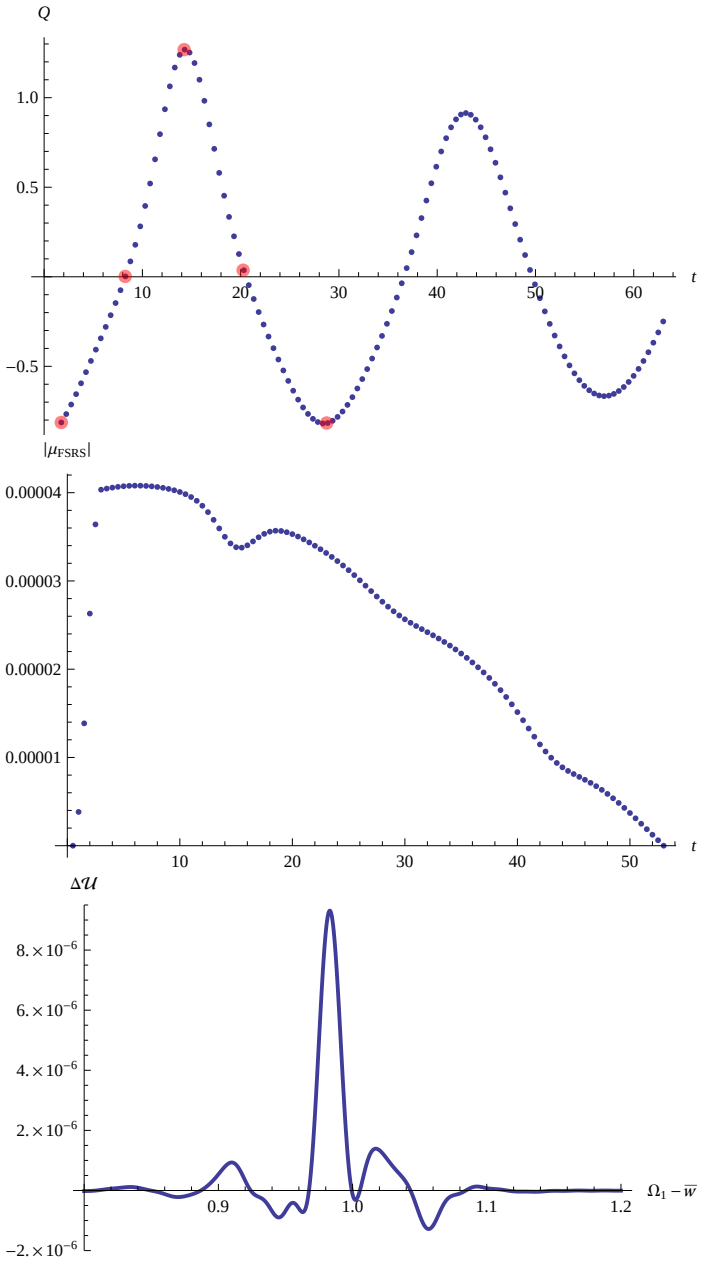

FIGURE 35. Top: Expectation value of conformational coordinate in units of l versus time in units of vibrational period $2\pi/\omega$. Points show $\langle Q(t)\rangle$ at half-period intervals. Large dots indicate value of conformational coordinate at a sequence of five potential-flip/pulse delays t_d for which a fissors signal is displayed. Middle: Magnitude of the fissors dipole for $t_d = 1.75(2\pi/\omega)$ in units of $\mu F_2 F_1^2$ as a function of time in units of $2\pi/\omega$. Note the abrupt, γ-induced turn-on of the dipole followed by the slow $f_1(t-t_d)$ dependent decay with the dips attributable to vibrational dephasing. Bottom: Calculated fissors signal $\Delta\mathcal{U}(\bar{\omega})$ in units of $2\hbar\Omega_2 F_1^2 F_2^2$ as function of resonance offset $\Omega_1 - \bar{\omega}$ in units of vibrational frequency ω at first of the five delays $t_d = \tau_f/2 + \tau_2 = 1.75(2\pi/\omega)$.

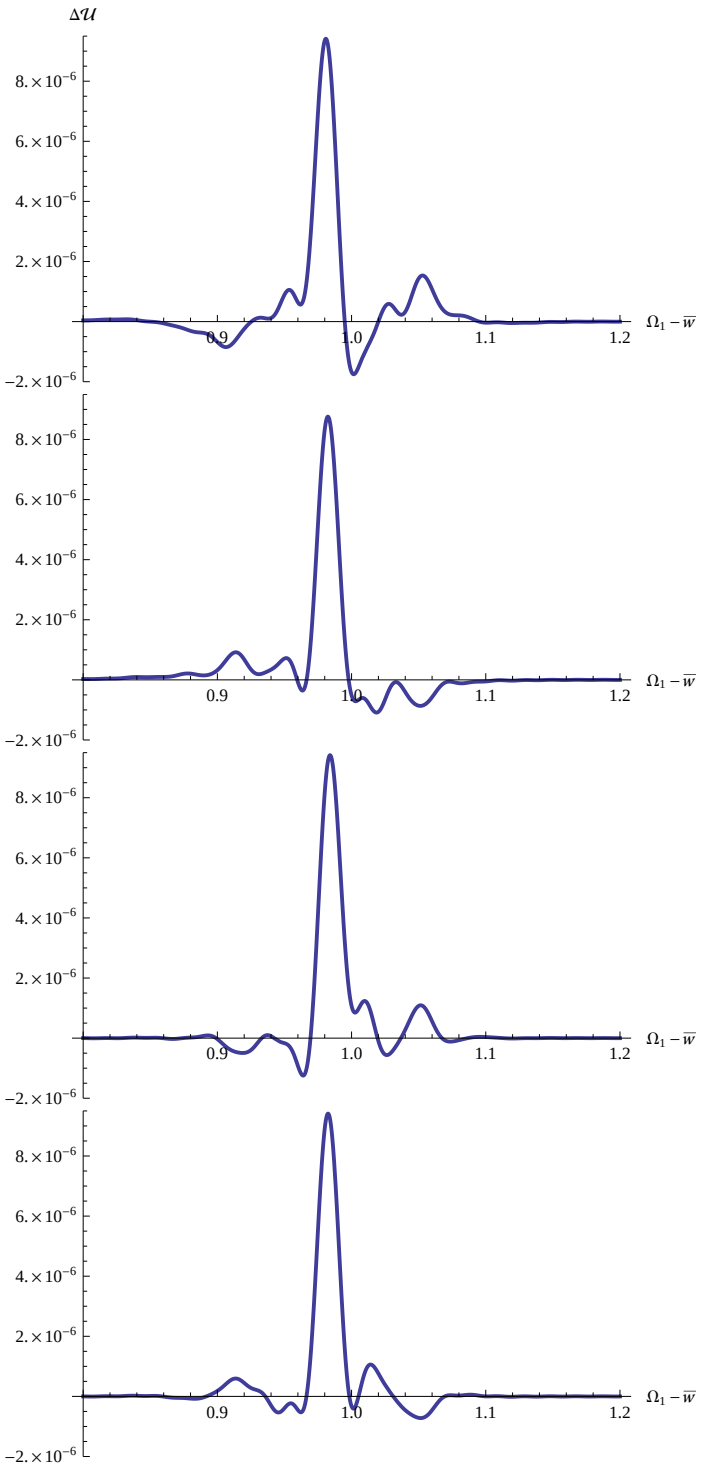

FIGURE 36. Fissors signals of model system at second through fifth delays $t_d = 8.25, 14.75, 20.75$ and 28.75 times $2\pi/\omega$, respectively, top to bottom. Note near constancy of central peak in Raman gain and similarity between signals at fifth delay and first (shown in Fig. 35.).

combining a fixed harmonic oscillator basis for the vibration with the discrete position representation for the conformation, we numerically evaluated the fidelity $|\langle\Phi_\circ(t)|\Phi_{\rm exact}(t)\rangle|^2$, where $|\Phi_{\rm exact}(t)\rangle$ and $|\Phi_\circ(t)\rangle$ are the exact and vibrationally adiabatically approximated two-dimensional nuclear wave packets following an *instantaneous* flip of the external conformational field from $-\Gamma_\circ$ to $\Gamma_\circ$. The fidelity was found to remain safely in excess of 0.99 for all times less than $100(2\pi/\omega)$.

How fissors works

The appearance in the fissors spectra (Figs. 35. and 36.) of sub-peaks of time-varying shape separated by shifts similar to conformational transition frequencies ($\approx$ 0.035ω for the particular conformational wave packet under study) suggests an analysis in terms of a sequence of vibrational-conformational eigenstates and eigenenergies. Such an interpretation simplifies if we neglect the weak dependence of α_{10} and γ on the conformational coordinate. With this simplification, 4.61 for the fissors signal becomes

$$\Delta\mathcal{U}(\bar\omega) \approx E_2'\Omega_2\mu F_2 F_1^2|\alpha_{10}(0)|^2\,{\rm Im}\int dt\, f_2'(t-t_d)f_1(t-t_d)\gamma(\tau_2\rho_{\tau_2}(t-t_d),0) \times e^{i(\Omega_1-\bar\omega)(t-t_d)}\langle\chi(t_d)|u_0^\dagger(t-t_d,\Gamma_\circ)u_1(t-t_d,\Gamma_\circ)|\chi(t_d)\rangle\ . \quad (4.62)$$

The signal is now expressed as the imaginary part of the Fourier component at frequency $\Omega_1-\bar\omega$ of a windowed overlap between copies of the conformational wave packet propagated on the vibrationally excited and vibrationally unexcited potential energy curves. [10,] [7] That overlap can be resolved in conformational

[10]There is a clear analogy between this description and that of electronic absorption in terms of Heller's overlap kernel between nuclear wave packets moving on different electronic potential

eigenstates (see 4.13):

$$\langle\chi(t_d)|u_0^\dagger(t-t_d,\Gamma_\circ)u_1(t-t_d,\Gamma_\circ)|\chi(t_d)\rangle$$
$$= \sum_{\chi_0\,\chi_1} e^{i(\mathcal{E}_{g0\chi_0}-\mathcal{E}_{g1\chi_1})(t-t_d)}\langle\chi(t_d)|\chi_0\rangle\langle\chi_0|\chi_1\rangle\langle\chi_1|\chi(t_d)\rangle \ . \quad (4.63)$$

According to 4.62 and 4.63, peaks should appear in the fissors spectrum at frequencies $\bar{\omega}$ down-shifted from the pump by the various vibrational-conformational transition frequencies $\mathcal{E}_{g1\chi_1} - \mathcal{E}_{g0\chi_0}$. These peaks are broadened slightly by the rapidly rising and slowly falling window function $\gamma \cdot f_1$ (see 4.16 and following 4.55). Importantly, *the weighting and shape of each contribution is determined by a complex coefficient* $\langle\chi(t_d)|\chi_0\rangle\langle\chi_0|\chi_1\rangle\langle\chi_1|\chi(t_d)\rangle$, *which varies with* t_d *on the conformational timescale.* A direct interpretation in terms of individual vibrational-conformational transitions would be complicated by the near degeneracy of many transition frequencies involving an increase or decrease of a certain number of conformational quanta. Given the similar form of the 0_g and 1_g vibrationally adiabatic conformational potential curves in the model system under study, the largest Franck-Condon overlaps $\langle\chi_0|\chi_1\rangle$ are those with $\chi_1 = \chi_0$, and this sequence accounts for the steady central peak in the fissors spectra. The Franck-Condon overlaps are smaller for transitions with $\chi_1 = \chi_0 \pm 1, \pm 2, \ldots$, but $\langle\chi_0|\chi(t_d)\rangle$ and $\langle\chi_1|\chi(t_d)\rangle$ depend differently on delay-time in these cases, so the products $\langle\chi(t_d)|\chi_0\rangle\langle\chi_1|\chi(t_d)\rangle$ remain t_d-dependent. As a result, the side-band structure varies with conformational motion.

---

energy surfaces. See Section 14.1 of D. J. Tannor, *Introduction to Quantum Mechanics: A Time-Dependent Perspective*, (University Science Books, Sausalito, 2007).

Vibrational frequency-tracking limit

How slowly must the conformational wave packet move in order to reach the limit in which fissors observes a well defined time-varying vibrational frequency? For a conformational wave packet of width ΔQ the range of "instantaneous" vibrational frequencies is $\Delta Q\, d\omega/dQ$. The time required for the peak vibrational frequency to change by this amount is $\dot{\omega}^{-1}\Delta Q\, d\omega/dQ = (\dot{Q}\, d\omega/dQ)^{-1}\Delta Q\, d\omega/dQ = \dot{Q}^{-1}\Delta Q$. For fissors to detect a well-defined vibrational frequency, rather than a complicated average over many such values, $\dot{Q}^{-1}\Delta Q$ must therefore exceed the lifetime of the fissors dipole, which, in the present instance is mostly set by τ_1 (the magnitude of the conformational wave-packet overlap in the integrand of 4.62 stays within the range 0.71 - 1.00 during $t_d - \tau_2 < t < t_d + \tau_2 + \tau_1$). Here, this criterion becomes $l/2l(0.034\omega) = 2.3(2\pi/\omega) \gtrsim \tau_1$. But a pump pulse this short could begin to compromise the spectral separation of pump and probe and would, in any case, give rise to a fissors dipole of bandwidth so large that it would fail to spectrally resolve the variations $\Delta\omega \approx K/m\omega l^2 = 0.036\omega$ in vibrational frequency.

In a model system identical in all other respects to that considered so far, but having the mass associated with conformational motion increased from $M = 30m$ to $480m$, the timescale of conformational motion should be approximately quadrupled. With the pump parameter shortened slightly to $\tau_1 = 25.0(2\pi/\omega)$, we begin to approach vibrational frequency-tracking behavior, in which the fissors dipole is short-lived enough catch the "instantaneous" value of $\omega(Q)$ without becoming so broad as to sacrifice the spectral resolution necessary to remain sensitive to variations in that quantity. In the fissors spectra themselves, plotted in Figs. 37. and 38., the conformational sidebands begin to merge with the "central

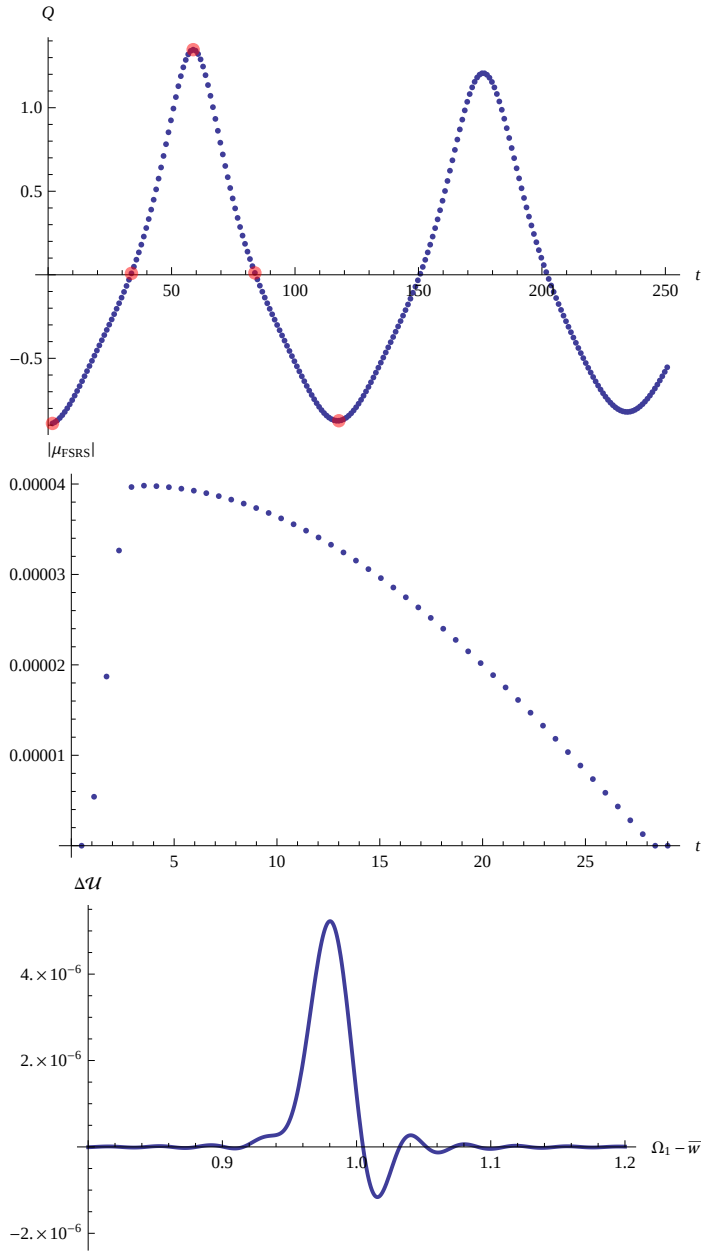

FIGURE 37. Conformational trajectory, magnitude of the fissors dipole, and the fissors signal for our model system having increased mass $M = 480m$ associated with conformational motion. Top: Expectation value of conformational coordinate in units of l versus time in units of vibrational period $2\pi/\omega$. Points show $\langle Q(t)\rangle$ at one-period intervals. Large dots indicate coordinate at sequence of five potential-flip/pulse delays for which a fissors signal is presented. Middle: Magnitude of the fissors dipole for $t_d = 1.75(2\pi/\omega)$ in units of $\mu F_2 F_1^2$ as a function of time in units of $2\pi/\omega$. Bottom: Fissors signal in units of $2\hbar\Omega_2 F_1^2 F_2^2$ as function of resonance offset in units of vibrational frequency ω at first of the five delays $t_d = 1.75(2\pi/\omega)$.

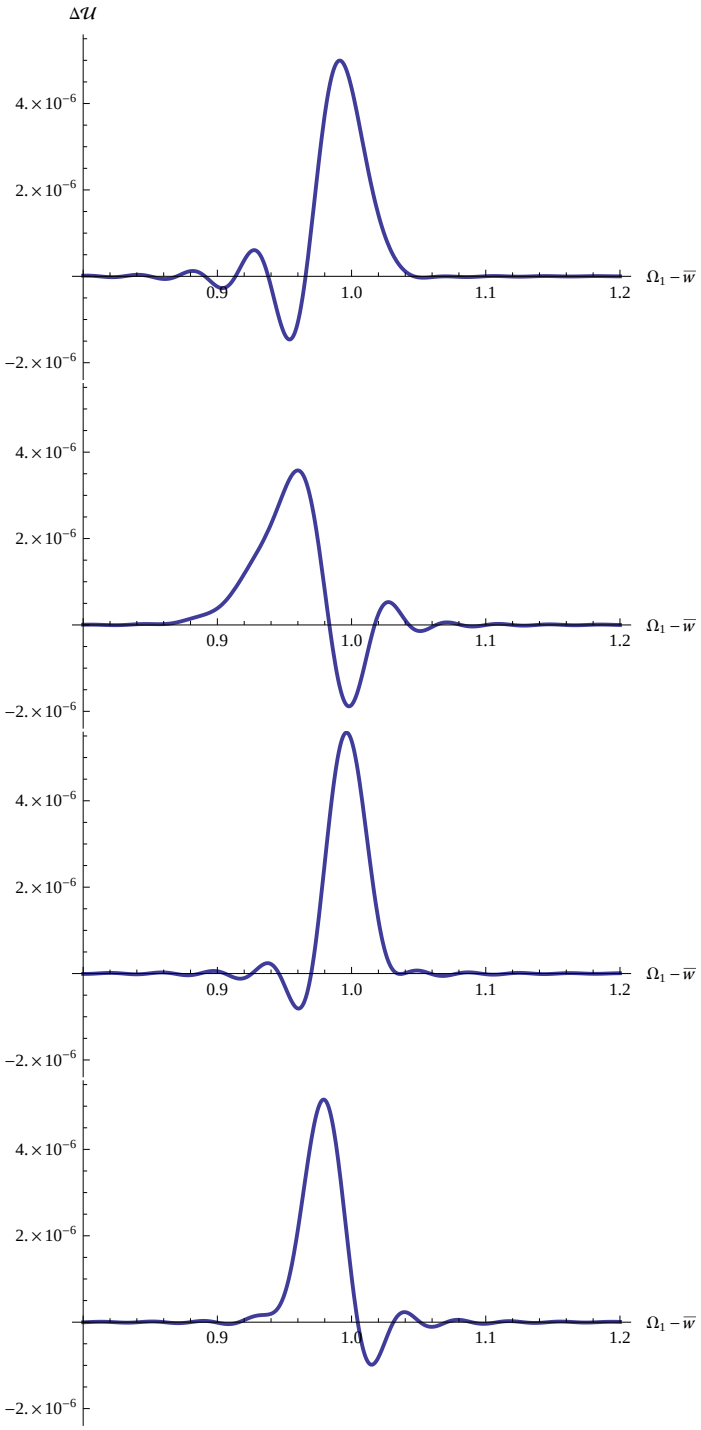

FIGURE 38. Fissors signals of model system with increased conformational mass at second through fifth delays $t_d = 33.75, 58.75, 83.75$ and 117.75 times $2\pi/\omega$, respectively, top to bottom. Note variation in main fissors peak as local vibrational frequency tracks slowly changing conformation.

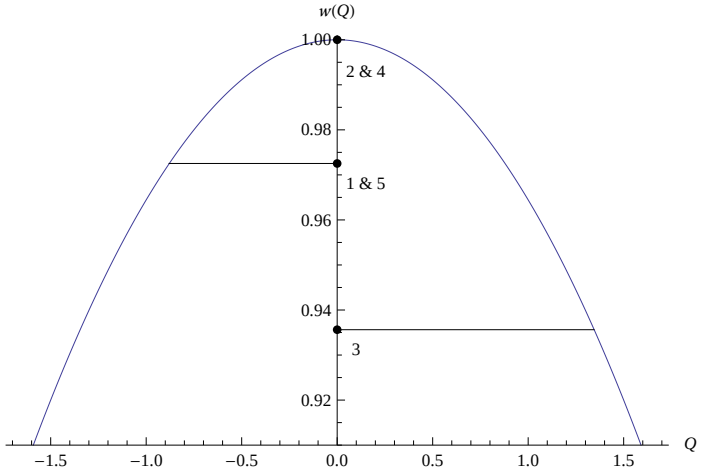

FIGURE 39. $\omega(Q)$ in units of ω versus Q in units of l. Dots indicate approximate value of vibrational frequency for expectation value of conformational coordinate at pulse arrival for the delays 1 through 5 whose signals are plotted in Figs. 37. and 38..

peak," but the latter remains narrow enough that its location adjusts discernibly to conformation-induced changes in the vibrational transition frequency.

The average value of the conformational coordinate is $\langle Q(t)\rangle = -0.890l$, $0.008l$, $1.348l$, $0.011l$, and $-0.874l$ at the first through fifth time delays indicated by large dots in the upper panel of Fig.38.. The round-trip time for conformational motion is about 120 vibrational periods in this case, in keeping with the $\sim 0.0085\omega$ spacing between adjacent levels in the conformational wave packet (now a linear superposition dominated by the 300^{th} to 340^{th} eigenstates). From a plot of $\omega(Q)$ shown in Fig. 39., we see that the local vibrational frequency associated with $\langle Q(t)\rangle$ tends approximately to track the Raman shift of the most prominent peak in the fissors spectrum. The approximate nature of this correspondence can be attributed in part to the change in $\omega(Q)$ that still occurs during the 27.5-vibrational-period duration of the fissors dipole.

Concluding Comments

The approach to femtosecond stimulated Raman spectroscopy developed here complements existing treatments by taking advantage of the timescale separation between "vibrational" and "conformational" nuclear degrees of freedom to justify a vibrationally adiabatic approximation to the conformational dynamics. Our derivations of the fissors-dipole expression of 4.60 and the fissors-signal expression of 4.61 rely only on time-dependent molecular quantum mechanics and the microscopic classical electrodynamical formula for the field radiated by an oscillating dipole. The numerical calculations of fissors spectra reported above exemplify the cases of relatively small and relatively large conformational mass in which, respectively, conformational sidebands accompany a nearly stationary central peak in the Raman gain and the sidebands merge with a central peak whose frequency tracks the evolving conformational coordinate.

For the sake of simplicity, the model Hamiltonian investigated here was taken to possess only two electronic levels; it was also assumed that the pulse center frequencies—in particular that of the elongated pump pulse—were far enough from electronic resonance that the temporal envelope of the pump varies adiabatically in the rotating frame. A more fully realistic analysis taking account of multiple, higher electronic levels and a closer approach of the pump-pulse center frequency to electronic resonance could potentially make use of a recent, throrough analysis of simultaneous adiabatic and nonadiabatic effects in electronic transitions.[106] That work by Mandal and Hunt could perhaps also serve a future treatment of the effect on fissors signals of vibrationally nonadiabatic corrections to the conformational motion.

Fissors measurements are said to be intrinsically heterodyne detected in that Raman gain results from interference between the fissors field and the transmitted probe pulse. [88] But the optical phase of the transmitted probe pulse is not independently controlled, as this is the same pulse that participates in stimulated-Raman generation of the fissors dipole. True heterodyne detection would become possible if the fissors field were made to interfere with an *external* local oscillator, which could be set up by passing a high-amplitude copy of the probe pulse around the sample and controlling its optical phase independently of the probe pulse incident upon the sample. From heterodyne-detected fissors signals, it would be possible to reconstruct the amplitude and phase of the time-evolving fissors dipole by combining the results of measurement with different phase-shifts—say in-phase and in-quadrature—between the incident probe field and the local oscillator.

CHAPTER V

DISCUSSION AND FUTURE PROSPECTS

We have presented a mixed quantum/semiclassical wave packet-dynamical approach to calculating spectroscopic signals, as well as theoretical works focused on the information content of Transient Absorption and femtosecond stimulated Raman spectroscopy. All three of these projects make use of a wave packet picture in the calculation of spectroscopic signals and emphasize the usefulness of a time-domain approach both in utility and accessibility.

Chapter II of this dissertation presents a demonstration of Fixed Vibrational Basis Gaussian Bath Theory (FVB/GB) in the calculation of linear absorption from the realistic three-dimensional model cluster I_2Kr_6. FVB/GB avails itself by making use of the timescale separation between the comparatively rapid dynamics of the mostly intermolecular system coordinate and the slower more extended motion of the bath in the partition of these two coordinates. As FVB/GB is a wave function based method, the total state of the complex remains a pure state for all time in the form of a tensor product of system times bath states. The advantage of this approach over basis set methods lies in the levels of treatment of the degrees of freedom in the model under study; the system dynamics are treated with conventional basis set methods and the bath degrees of freedom are subject to a multidimensional thawed Gaussian form. Parametrization of the bath degrees of freedom lends itself by decreasing the computational effort required in FVB/GB versus basis set methods; effort has power law dependence in FVB/GB wheres basis set methods scale exponentially for the number of degrees of freedom.

The wave packet dynamical approach is developed and tested both in the simulation of dynamics and the calculation of a linear absorption spectrum. Bath wave packet parameter paths are successfully calculated for $\approx$ 2.5 ps with a 100 as time-step with implementation of a fourth-order Runge-Kutta numerical integration routine. Use is made of Heller's absorption kernel[9] in the calculation of a linear absorption spectrum for I_2Kr_6 where resolution on the order of ten cm^{-1} is obtained despite the presence of several thousand spectral lines and multiple resonances within the spectrum. This result is compared with a numerically exact absorption spectrum for I_2Kr_6 calculated through basis set methods and interpretation of the spectra based on analysis of the absorption kernel followed.

Chapter III rebuilds the theory of transient absorption spectroscopy with the goal of clarifying the source of anti-phased oscillations about the Stokes-shifting node in a recent transient absorption spectrum from photosyntheic light-harvesting protein PC577.[1] Making use of reduced pulse propagators, expressions for the relevant time-dependent dipole moments that give rise to transient absorption spectra are isolated and expressed as time-dependent wave packet overlaps, and the spectrally resolved transient-transmission signal is expressed as the change in electromagnetic energy of the transmitted probe pulse. A realistic model system of PC577 is developed and transient absorption signals are calculated.

The contribution from the stimulated emission dipole was found to be the primary source of the Stokes shifting node and anti-phased quantum beats in this work and an analogy with femtosecond stimulated Raman spectroscopy signals was made to explain the time-resolution in the stokes shifting node yet lack there of for the anti-phased quantum beats seen on either side of the node. The source of the side bands was explained schematically and accompanied by the argument that

small amplitude displacement of a multidimensional wave packet about the steady state fluorescence maximum leads to simultaneous loss (or gain) of probability amplitude along a blue shifted frequency and gain (or loss) along a slightly red-shifted frequency about the steady state fluorescence maximum.

Chapter IV offered a theoretical investigation and interpretation of the information content of femtosecond stimulated Raman spectroscopy signals. A simple yet realistic model system was developed comprising two modes with time-scales such that the slower conformational mode adiabatically followed the vibrational mode and an expression for the time-dependent dipole in a fissors experiment was isolated. It was argued that the overlap between the ket which interacted with the sequential action of the pump then probe pulse with a bra which only interacted with the pump is the sole contribution to the Raman gain in a fissors experiment. Using this overlap in the expression for the fissors signal, the resolution and information content of the technique were explored by considering the signal from the model with two different conformational masses. In the case with a light conformational mass, a nearly steady central peak in the Raman gain was observed with time-dependent sidebands spaced from the central peak by the various frequency differences that make up the conformational wavepacket. Switching to a heavier conformational mass, which slowed conformational motion, lead to the merging of the sidebands with the central peak such that the expectation value of the conformational coordinate was approximately followed by the time-dependant central Raman-gain peak. Further arguments were offered for the time and frequency resolution in a fissors experiment.

Future directions for this work include the dynamics simulation of larger dimensional clusters with FVB/GB and the calculation of ultrafast spectroscopic

signals from these systems. With the model systems I_2Kr_17, I_2Kr_18, I_2Kr_72 and I_2Kr_182 already in hand, it will be a straightforward task to apply the theory on these clusters to test the notions that it will not be necessary to include artificial decay functions in the calculation of spectra and the boundary of the cluster having less of an effect as the bath size increases. Steps in theses directions necessitate a re-derivation of FVB/GB theory to include a multidimensional bath and developing a perturbative formualtion of the theory out to various orders in the electric field to facilitate calculation of the spectroscopic observables of interest.

We also maintain the interest in investigating the implementation of femtosecond stimulated Raman spectroscopy in the ground electronic state through the use of a sequence of weak ultra-short pulses which together act as a signal pump pulse in the experiment. This approach has the possibility of minimizing the effect of third-order cascades signals that overwhelm the fifth order ground state fissors signal.

APPENDIX A

FVB/GB APPENDIX

Many-Body Potential

We approximate the total potential energy function in a given electronic state of the I_2 chromophore as a sum of atom-atom pair-potentials,

$$V(r) = \sum_{i=1}^{N-1} \sum_{j=i+1}^{N} \upsilon_{ij}(r_{ij}), \tag{A.1}$$

N specifies the number of atoms in a particular model system. The atomic indices i and j on υ_{ij} specify the contributing pair-potentials in the sum, and the argument of each pair-potential, r_{ij}, is the distance between the i^{th} and j^{th} atom in 3-dimensional Cartesian coordinate space.

Given the Gaussian ansatz for the bath degrees of freedom, we can analytically evaluate matrix elements of the bath and interaction potential that appear in the FVB/GB equations if all atom-atom pair potentials are expressed as sums of Gaussian functions of the interatomic distance.[43] The fitting function has the general form,

$$\upsilon_{ij}(r_{ij}) = \sum_{k=1}^{g} c_k e^{-\alpha_k {r_{ij}}^2}, \tag{A.2}$$

with g specifying the number of Gaussian functions used in a particular fit.

I_2 X-state pair potential

The X-state I-I pair potential for the models is defined as a four-Gaussian fit to the RKR data points;[107] the fit parameters are given in Table 1.. In all

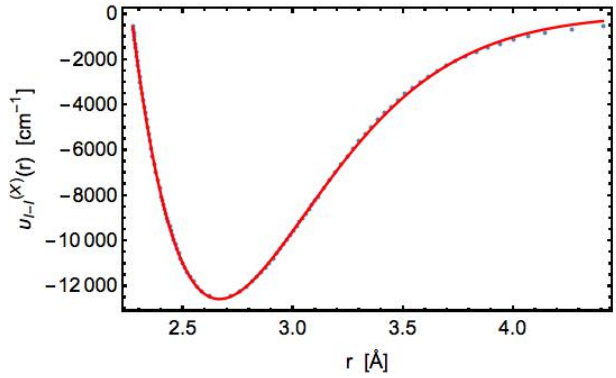

FIGURE 40. Plot of I_2 X-state RKR data points (blue) and fit composed of a sum of four Gaussians (red).

tabulated quantities below, $\hbar = 1$ which renders energy and angular frequency as numerically equivalent. The units reported on frequency values, cm^{-1}, are to be read as inverse wavelengths, or wave-numbers. To quantify the quality of

TABLE 1. I-I X-state potential parameters

Parameter	Value
c_1	-5.25838 × 10^5 cm^{-1}
α_1	0.485029 Å^{-2}
c_2	1.24037 × 10^6 cm^{-1}
α_2	0.640439 Å^{-2}
c_3	8.89558 × 10^5 cm^{-1}
α_3	0.636006 Å^{-2}
c_4	-2.17614 × 10^5 cm^{-1}
α_4	0.346135 Å^{-2}

TABLE 2. I-I X-state fit comparison values

Quantity	RKR[107]	4 G fit
r_0	2.66767 Å	2.66502 Å
ω	214.642 cm^{-1}	217.824 cm^{-1}
D_e	12542 cm^{-1}	12562 cm^{-1}

the fit, we compare the equilibrium distance (r_0) fundamental frequency (ω) and

dissociation energy relative to the minimum of the potential (D_e) between the fit and the RKR data points in Table 2..

Working with the RKR data sets[107, 108], r_0 is defined as the average of the distance values corresponding to the $\nu = 0$ data points. The fundamental frequency is taken as two times the average energy between the $\nu = 0$ and $\nu = 1$ data points. We rely on Herzberg's[41] reported value for the dissociation energy of I_2 from $\nu = 0$ in the X-state and then add the zero point energy from above to find the dissociation energy relative to the potential minimum. This is done because the dataset does not extend to the dissociation limit.

For all analytic pair-potential functions, the equilibrium position is found by equating $\frac{\partial \upsilon(r)}{\partial r}$ to zero and solving, sometimes numerically, for r. The fundamental frequency is found through Eq. (A.3), where m_1 and m_2 specify the masses of the two atoms interacting in a given potential. Lastly, the dissociation energy is found by evaluating each pair-potential at its equilibrium position, as we shift the energy of each pair potential so that its dissociation energy lies at zero.

$$\omega = \sqrt{\frac{m_1 + m_2}{m_1 m_2} \left(\frac{\partial^2 \upsilon(r)}{\partial r^2} \right) \Big|_{r=r_0}}. \tag{A.3}$$

I_2 B-state pair potential

Due to its narrow width, and drastic change in slope between $r = 4$ Å and $r = 7$ Å , the I_2 B-state RKR[108] data set was weighted in order to yield a good fit for this pair-potential. A trial fit revealed that the RKR points between $r = 4$ Å and $r = 7$ Å were problematic to capture with an un-weighted fitting routine. Using the residuals from the trial fit, we assigned weight to the data set by multiplying each data point by the absolute value of its residual.

After implementing the weighting function, we arrived at an accurate three-Gaussian fit to the B-state I-I pair potential. The equilibrium position, fundamental frequency and dissociation energy of our fit are compared with those from the RKR data in Table 3.. The dissociation energy relative to the potential minimum was obtained from Reference 5. The fit parameters are summarized in Table 4., and a plot of the RKR data points along with the fit is shown in Figure 41..

TABLE 3. I-I B-state fit comparison values

Quantity	RKR[108]	3 G fit
r_0	3.02825 Å	3.02398 Å
ω	124.929 cm^{-1}	125.831 cm^{-1}
D_e	4381.3 cm^{-1}	4373.9 cm^{-1}

TABLE 4. I-I B-state potential parameters

Parameter	Value
c_1	1.45402×10^6 cm^{-1}
α_1	0.623856 $Å^{-2}$
c_2	-3.28908×10^3 cm^{-1}
α_2	0.098624 $Å^{-2}$
c_3	-2.25092×10^5 cm^{-1}
α_3	0.36657 $Å^{-2}$

Kr-Kr pair potential

The Kr-Kr pair potential is a two-Gaussian fit to a Buckingham-type function[40, 5] of the form,

$$\upsilon_{\text{Kr-Kr}}(r) = Ae^{-Br} - C/r^6 - D/r^8. \tag{A.4}$$

A plot of the fit and the analytic function is shown in Figure 42.. We compare

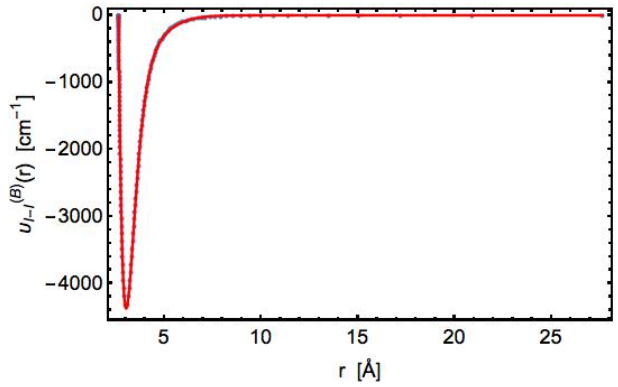

FIGURE 41. Plot of I_2 B-state RKR data points (blue) and fit composed of a sum of three Gaussian functions (red).

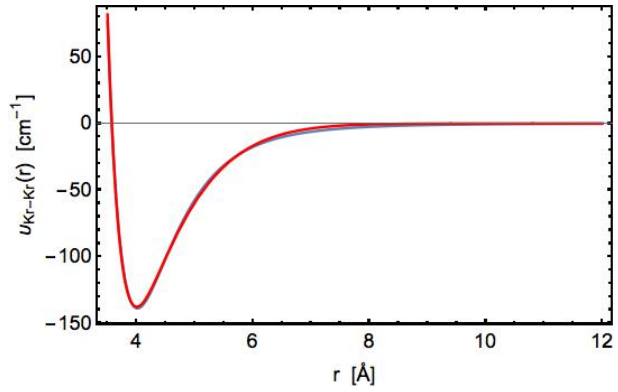

FIGURE 42. Plot of Buckingham-type function used to model the Kr-Kr potential (blue) and our fit composed of a sum of two Gaussian functions (red).

the equilibrium position, fundamental frequency and dissociation energy of our two-Gaussian fit with those of the Buckingham-type function in Table 5.. The fit parameters and the Buckingham function parameters[5] are displayed in Table 6..

TABLE 5. Kr-Kr Fit comparison values

Quantity	Buckingham-type	2 G fit
r_0	4.01373 Å	4.00221 Å
ω	16.482 cm^{-1}	16.350 cm^{-1}
D_e	138.929 cm^{-1}	137.668 cm^{-1}

TABLE 6. Kr-Kr potential parameters

Parameter	Value
A	8.57701×10^7 cm^{-1}
B	3.26046 $Å^{-1}$
C	4.32949×10^5 cm^{-1} $Å^6$
D	1.43582×10^7 cm^{-1} $Å^8$
c_1	9.20553×10^5 cm^{-1}
α_1	0.64499 $Å^{-2}$
c_2	-1.06524 $\times 10^3$ cm^{-1}
α_2	0.11543 $Å^{-2}$

I-Kr pair-potential

The I-Kr pair potential is approximated by the Xe-Kr Lennard-Jones potential,[6]

$$\upsilon_{\text{I-Kr}}(r) = 4\epsilon\Big(\frac{\sigma^{12}}{r^{12}} - \frac{\sigma^6}{r^6}\Big). \tag{A.5}$$

We fit the Lennard-Jones potential to a sum of two Gaussian functions. The potential parameters for the I-Kr Lennard Jones function and those for the fit are listed in Table 8.. The equilibrium distance, fundamental frequency, and dissociation energy values are compared in Table 7., and a plot showing the fit and the analytic function is displayed in Figure 43..

TABLE 7. I-Kr Fit Comparison Values

Quantity	Lennard-Jones	2 G fit
r_0	4.19801 Å	4.18298 Å
ω	14.971 cm^{-1}	14.833 cm^{-1}
D_e	162.3 cm^{-1}	160.2 cm^{-1}

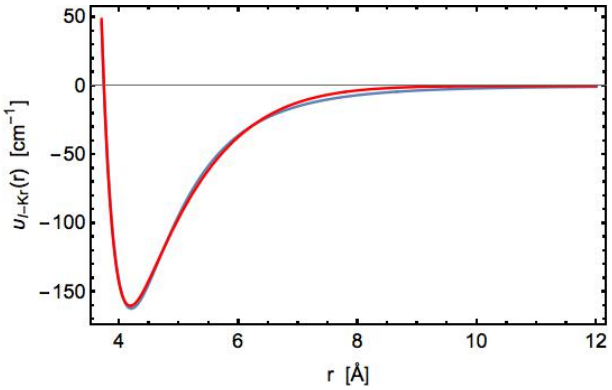

FIGURE 43. Plot of Xe-Kr Lennard Jones function used to model the I-Kr potential
(blue) and fit composed of a sum of two Gaussians (red).

TABLE 8. I-Kr potential parameters

Parameter	Value
σ	3.74 Å
ϵ	162.3 cm^{-1}
c_1	2.88397×10^6 cm^{-1}
α_1	0.668716 $Å^{-2}$
c_2	-840.973 cm^{-1}
α_2	0.0868177 $Å^{-2}$

Harmonic Net Potential

To realistcally depict an extended bulk krypton lattice doped with and iodine molecule, the question of how big to make the host lattice arises. A lattice consisting of several thousand atoms would accurately mimic a molecular crystal produced in a lab, but even with the computational advantages offered by FVB/GB theory, (computational effort has power law dependence on the number of bath

degrees of freedom under FVB/GB in contrast to the exponential scaling of traditional basis set methods)[40], the computational demand of simulating the dynamics of such a lattice is quite large. Implementing periodic-boundary conditions is one way to side-step the need to include several thousand atoms in the lattice, however when the phonon modes of the lattice are governed by thawed Gaussian wave packets, as prescribed under FVB/GB theory, a level of complexity is introduced into the theory as the periodic boundary becomes dynamic through its dependence upon bath wave packet centers and widths. Choosing the size of the lattice based on a compromise between reality and practicality, and obviating the need for periodic boundary conditions, we choose clusters of atoms as our model systems.

As clusters, our model systems have an outer surface and the possibility exists that a surface atom could, given enough energy, leave the cluster. In order to prevent this, we make use of a *harmonic net potential*. In the harmonic net, each outer-layer nearest-neighbor krypton-krypton interaction is replaced with a harmonic potential by retaining only quadratic contributions to the full potential function. To facilitate integration over matrix elements of the bath and interaction potentials, all harmonic interactions to a sum of Gaussian functions.

Iodine in Krypton Clusters

With the goal of simulating the dynamics of a small guest molecule in a cryogenic host medium, we've developed several model systems on which to test FVB/GB theory. All systems resemble a chunk of krypton atoms doped with a centrally-located iodine molecule, but range in size from 8 to 184 atoms. All calculations within the main text have been performed on I_2Kr_6, the smallest of

our models. Inspired by the work of Buchholz and co-workers,[42] we've established I_2Kr_{17} comprising a shell of 17 krypton atoms arranged in a double icosahedron geometry around an iodine molecule. Depicting an increasing number of solvation shells around iodine, we've also developed I_2Kr_{18}, I_2Kr_{72}, I_2Kr_{182} which consist of the iodine dimer surrounded by one, two and three solvation layers of krypton atoms respectively. All models are treated as finite molecular clusters; we make no use of periodic boundary conditions in our simulations.

I_2Kr_6

To find the normal coordinates in the ground electronic state of I_2Kr_6, the model must first be equilibrated. The relevant pair potentials during equilibration are the Gaussian fits to the X-state I_2, Kr-Kr and Xe-Kr potentials discussed above. Construction begins by placing the mid-point of the iodine atoms at the origin with the atom centers 1.5 angstroms from the origin along the z-axis. The krypton atoms are placed in the xy-plane in a hexagon geometry centered around the origin. The coordinate vector for each krypton atom has a magnitude of 4.2 Å from the origin. This starting geometry has a total of 4500 cm^{-1} of energy in the atom-atom bonds, 3021 cm^{-1} of which is in the I_2 bond alone.

To equilibrate the model, we make use of a classical velocity-Verlet algorythm.[44] The kinetic energy of all atoms is initially zero—we do not assign initial velocities based a Boltzmann distribution. This choice preserves the symmetry of the complex. Using a fixed time-step of 0.1 fs, a cooling simulation was run where after each time-step the velocity is multiplied by 0.9999. By slowly removing kinetic energy from the cluster in this way, atomic rearrangement is allowed eventually leading to a stable minimum-energy configuration. After

one nanosecond of cooling, the complex contained 1212 cm^{-1} of energy. This corresponds to a loss of 3288 cm^{-1} of energy during equilibration, mostly coming the I_2 bond. The equilibrium coordinates of each atom in the structure are found in Tab. (9.).

TABLE 9. I_2Kr_6 minimum energy configuration $r^{(0)}$

Atom	x (Å)	y (Å)	z (Å)
I	0	0	1.332 468
I	0	0	−1.332 468
Kr	3.971 893	$1.290\,000 \times 10^{-18}$	0
Kr	−3.971 893	$-3.640\,000 \times 10^{-19}$	0
Kr	1.985 947	3.439 761	0
Kr	−1.985 947	3.439 761	0
Kr	1.985 947	−3.439 761	0
Kr	−1.985 947	−3.439 761	0

The initial geometry of I_2Kr_6 had D_{6h} symmetry. With the choice to assign zero velocities to the atoms in the complex, the relaxation procedure preserves the symmetry of the model as any rearrangement of the structure honors the full symmetry of the Hamiltonian. This feature of the equilibration routine allows for the separation between symmetric and non-totally symmetric normal modes of the model facilitating dynamical treatment of a given set of modes. Electronic excitation of the totally symmetric system coordinate—at least initially—only produces motion in the totally symmetric Franck-Condon active bath modes. With the goal of FVB/GB aimed at the simulation of spectroscopic signals from large molecular systems, treating the dynamics of only Franck-Condon active modes serves to reduce the necessary computational effort in the calculations.

After equilibration, the harmonic net potential discussed in section A.1 is implemented. Since all the krypton atoms in I_2Kr_6, are outer layer atoms, every

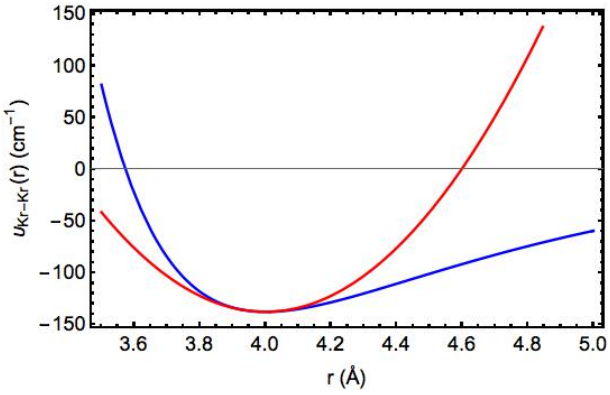

FIGURE 44. Plot of the full Kr-Kr potential (blue) and fit to the quadratic expansion of the full Kr-Kr potential evaluated at $r^{(0)}$ for I_2Kr_6 composed of a sum of five Gaussian functions (red).

nearest-neighbor interaction is replaced by a harmonic interaction by expanding the full Kr-Kr pair potential and truncating at second order in the atomic distance. Due to the symmetry of the structure, the interaction between any two krypton atoms is the same, and therefore a single harmonic potential governs the motion between all nearest-neighbor krypton atoms in I_2Kr_6. To facilitate integration over matrix elements of the system-bath interaction potential that appear in the DFM variational equations, the Kr-Kr harmonic interaction is fit to a sum of five Gaussian functions. This fit is shown in Figure 44., and the fit parameters are shown in Table 10..

With the minimum energy configuration $r^{(0)}$ the normal coordinates in the ground electronic state of the model are found through the recipe described in section 2.2. In Fig. 1. we plot bath mode frequency vs. mode number, for the normal coordinates of I_2Kr_6, in units of the system frequency. The frequency of the totally symmetric bath mode is marked with a red bar. In the main text, we treat the dynamics of the totally symmetric system and bath modes by zeroing out the normal coordinates ξ of the non-totally symmetric bath modes. The the system

TABLE 10. Fit parameters for Kr-Kr harmonic interaction in I_2Kr_6

Parameter	Value
c_1	947.258 cm^{-1}
α_1	0.5217 $Å^{-2}$
c_2	1850.934 cm^{-1}
α_2	0.2203 $Å^{-2}$
c_3	1.4409×10^4 cm^{-1}
α_3	0.04848 $Å^{-2}$
c_4	-1.5110×10^4 cm^{-1}
α_4	0.02809 $Å^{-2}$
c_5	2.09714×10^3 cm^{-1}
α_5	-0.02134 $Å^{-2}$

coordinate has a frequency of 218.104 cm^{-1}, and the totally symmetric bath mode frequency is 27.394 cm^{-1} in the ground electronic state. Pictures of the structure with the these coordinates stretched are shown in Figs. (2.) and (3.) respectively.

I_2Kr_{17}

Inspired by the work of Buchholz and co-workers,[42] we've established I_2Kr_{17} comprising a shell of 17 krypton atoms arranged in a double icosahedron geometry around an iodine molecule.The initial conditions of I_2Kr_{17} have the iodine molecule along the z-axis with the origin halfway between the two atoms; each iodine atom is centered 1.5 Åfrom the origin. An end cap krypton atom is then placed along the z-axis on the outer side of each iodine atom at a distance of 6.0 Åfrom the origin. In the xy - plane, around the waist of the iodine chromophore, is placed a ring of five krypton atoms with each atom centered at the vertex of a pentagon. The magnitude of the vector specifying the position of each krypton atom in this pentagon is chosen as 4.0 Å. Above and below the central krypton ring is placed another pentagon ring of krypton atoms having the same radial distance from the

z-axis. Both rings are spaced 4.0 Åfrom the xy - plane and are rotated with respect to the central ring by $\frac{2\pi}{5}$.

Following the same velocity -Verlet cooling simulation discussed for I_2Kr_6, the equilibrium structure for this model is found after 3 ns of cooling with a time step of 0.1 fs. In the cooling simulation, the structure loses 5858.41 cm^{-1} or energy, 3021.4 cm^{-1} of which is from the iodine molecule alone. The coordinates of each atom in the equilibrium structure are given in Tab. (11.). From the equilibrium structure, the normal coordinates in the electronic ground state of I_2 are found through diagonalization of the Hessian matrix; the system mode is found to have a frequency of 223.073 cm^{-1}. As shown in Fig. (45.) the structure has four totally symmetric bath modes with frequencies of 31.5833 cm^{-1}, 30.1361 cm^{-1}, 26.8931 cm^{-1} and 16.4342 cm^{-1}.

TABLE 11. I_2Kr_{17} minimum energy configuration $r^{(0)}$

Atom	x (Å)	y (Å)	z (Å)
I	0	0	1.329 252
I	$5.090\,000 \times 10^{-13}$	$2.240\,000 \times 10^{-15}$	−1.329 252
Kr	$-8.710\,000 \times 10^{-13}$	$-1.780\,000 \times 10^{-14}$	5.378 050
Kr	$1.290\,000 \times 10^{-12}$	$1.690\,000 \times 10^{-14}$	−5.378 050
Kr	−3.852 718	$-4.200\,000 \times 10^{-14}$	$-7.940\,000 \times 10^{-13}$
Kr	−1.190 555	3.664 152	$-2.610\,000 \times 10^{-13}$
Kr	3.116 914	2.264 571	$6.200\,000 \times 10^{-13}$
Kr	3.116 914	−2.264 571	$6.030\,000 \times 10^{-13}$
Kr	−1.190 555	−3.664 152	$-2.940\,000 \times 10^{-13}$
Kr	3.489 458	$-1.480\,000 \times 10^{-14}$	3.328 376
Kr	1.078 302	−3.318 671	3.328 376
Kr	−2.823 031	−2.051 052	3.328 376
Kr	−2.823 031	2.051 052	3.328 376
Kr	1.078 302	3.318 671	3.328 376
Kr	3.489 458	$1.080\,000 \times 10^{-14}$	−3.328 376
Kr	1.078 302	−3.318 671	−3.328 376
Kr	−2.823 031	−2.051 052	−3.328 376
Kr	−2.823 031	2.051 052	−3.328 376
Kr	1.078 302	3.318 671	−3.328 376

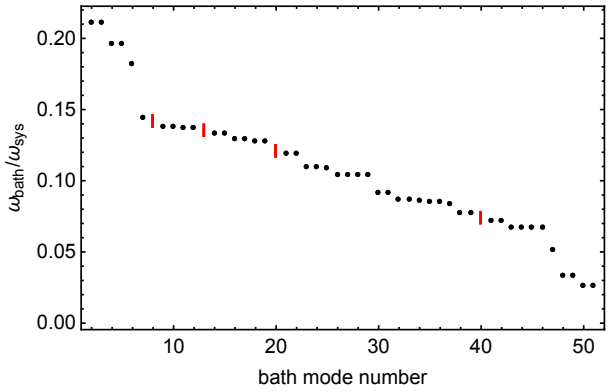

FIGURE 45. Plot of bath frequencies made dimensionless by division with the ground state system frequency of I_2Kr_{17}. The frequencies of the four totally symmetric bath modes in this model are indicated by red bars.

Iodine surrounded by varying number of solvation layers of krypton atoms

The following three model systems are built up from the same 1372 atom fcc crystalline chunk of krypton atoms. The lattice constant for the chunk is assigned the value of $a = 5.554644$ Åwhich was determined through equilibration of the lattice. For each model, in the approximate center of the bulk, in the (111)-plane, two krypton atoms were replaced by iodine atoms, and served as the reference point around which the clusters were constructed. Note that selecting the iodine atoms in this way results in a significantly stretched I_2 bond in the X-state with approximately 11,000 cm$^-$1 of energy initially.

The first solvation layer of krypton atoms around the iodine dimer was identified by locating all krypton atoms within a nearest neighbor distance ($\frac{a}{\sqrt{2}}$) of either iodine atom. Similarly, the second and third solvation layers were found by selecting all krypton atoms within a nearest neighbor distance of any krypton atom in the first or second solvation shell respectively. In order to maintain the symmetry of the clusters during equilibration, the initial cooling simulation for each model— in which most of the energy within the iodine bond is dissipated—

was run with the addition of two static layers of krypton atoms around the mobile atoms in a given cluster. The static layers impose forces on the mobile atoms in the cluster, but do not move from their equilibrated fcc positions. The layers of static atoms serve to mitigate the effect of numerical error in the cooling simulations and also prevent krypton atoms from leaving the clusters while large amounts of energy from the iodine bond radiates into the krypton lattice. At this stage, a time-step of 1.0×10^{-15} s was used in the velocity Verlet algorithm.

After equilibration with static layers, the static layers were removed and the mobile atoms were allowed to equilbrate on their own. The second equilibration for these models was done with a time-step of 1.0×10^{-17} s in order to minimize numerical error in the simulation and resulted in the loss of approximately 200 cm^{-1} more of energy for each cluster. The normal coordinates for clusters were found at this point; Figs(47. -48.) show the dimensionless frequencies of the bath coordinates relative to the system frequency. Tables (13.-14.) provide the equilibrium structures for the three model clusters.

$$I_2Kr_{18}$$

TABLE 12. I_2Kr_{18} equilibrium coordinates

Atom	x (Å)	y (Å)	z (Å)
I	$-8.840\,000\times10^{-15}$	$6.710\,000\times10^{-15}$	1.332 541
I	$8.840\,000\times10^{-15}$	$-6.710\,000\times10^{-15}$	−1.332 541
Kr	−2.172 241	3.197 762	$1.120\,000\times10^{-13}$
Kr	2.172 241	3.197 762	$3.680\,000\times10^{-14}$
Kr	−4.011 108	$-4.440\,000\times10^{-14}$	1.931 442
Kr	4.011 108	$9.160\,000\times10^{-14}$	1.931 442

Kr	$-2.172\,241$	$-3.197\,762$	$7.370\,000 \times 10^{-14}$
Kr	$1.972\,072$	$2.757\,009$	$3.860\,637$
Kr	$2.172\,241$	$-3.197\,762$	$1.390\,000 \times 10^{-13}$
Kr	$-1.972\,072$	$2.757\,009$	$3.860\,637$
Kr	$2.450\,000 \times 10^{-14}$	$3.620\,000 \times 10^{-14}$	$5.790\,742$
Kr	$1.972\,072$	$-2.757\,009$	$3.860\,637$
Kr	$-1.972\,072$	$-2.757\,009$	$3.860\,637$
Kr	$-3.410\,000 \times 10^{-14}$	$-2.200\,000 \times 10^{-14}$	$-5.790\,742$
Kr	$-4.011\,108$	$9.250\,000 \times 10^{-14}$	$-1.931\,442$
Kr	$4.011\,108$	$-8.470\,000 \times 10^{-14}$	$-1.931\,442$
Kr	$1.972\,072$	$2.757\,009$	$-3.860\,637$
Kr	$-1.972\,072$	$2.757\,009$	$-3.860\,637$
Kr	$1.972\,072$	$-2.757\,009$	$-3.860\,637$
Kr	$-1.972\,072$	$-2.757\,009$	$-3.860\,637$

I_2Kr_{72}

TABLE 13. I_2Kr_{72} equilibrium coordinates

Atom	x (Å)	y (Å)	z (Å)
I	$1.190\,000 \times 10^{-13}$	0	$1.334\,119$
I	$-1.210\,000 \times 10^{-13}$	$8.170\,000 \times 10^{-14}$	$-1.334\,119$
Kr	$-2.123\,458$	$3.083\,908$	$3.860\,000 \times 10^{-13}$
Kr	$2.123\,458$	$3.083\,908$	$1.670\,000 \times 10^{-13}$
Kr	$-3.968\,624$	$2.380\,000 \times 10^{-13}$	$1.907\,705$
Kr	$3.968\,624$	$-5.260\,000 \times 10^{-13}$	$1.907\,705$

Kr	$-2.123\,458$	$-3.083\,908$	$-3.670\,000 \times 10^{-13}$
Kr	$1.959\,909$	$2.798\,048$	$3.824\,504$
Kr	$2.123\,458$	$-3.083\,908$	$-2.100\,000 \times 10^{-13}$
Kr	$-1.959\,909$	$2.798\,048$	$3.824\,504$
Kr	$-8.440\,000 \times 10^{-15}$	$-8.530\,000 \times 10^{-13}$	$5.685\,255$
Kr	$1.959\,909$	$-2.798\,048$	$3.824\,504$
Kr	$-1.959\,909$	$-2.798\,048$	$3.824\,504$
Kr	$-2.150\,000 \times 10^{-13}$	$7.570\,000 \times 10^{-13}$	$-5.685\,255$
Kr	$-3.968\,624$	$1.560\,000 \times 10^{-13}$	$-1.907\,705$
Kr	$3.968\,624$	$5.930\,000 \times 10^{-13}$	$-1.907\,705$
Kr	$1.959\,909$	$2.798\,048$	$-3.824\,504$
Kr	$-1.959\,909$	$2.798\,048$	$-3.824\,504$
Kr	$1.959\,909$	$-2.798\,048$	$-3.824\,504$
Kr	$-1.959\,909$	$-2.798\,048$	$-3.824\,504$
Kr	$-4.001\,849$	$5.772\,736$	$-2.008\,715$
Kr	$2.250\,000 \times 10^{-13}$	$5.725\,992$	$1.971\,085$
Kr	$-1.480\,000 \times 10^{-13}$	$5.725\,992$	$-1.971\,085$
Kr	$-4.001\,849$	$5.772\,736$	$2.008\,715$
Kr	$-5.973\,488$	$2.871\,987$	$7.240\,000 \times 10^{-13}$
Kr	$4.001\,849$	$5.772\,736$	$-2.008\,715$
Kr	$4.001\,849$	$5.772\,736$	$2.008\,715$
Kr	$5.973\,488$	$2.871\,987$	$9.280\,000 \times 10^{-13}$
Kr	$-7.891\,411$	$-6.040\,000 \times 10^{-14}$	$1.982\,211$
Kr	$-3.961\,880$	$-1.040\,000 \times 10^{-12}$	$5.822\,591$
Kr	$-5.899\,684$	$2.821\,067$	$3.923\,708$

Kr	−5.899 684	−2.821 067	3.923 708
Kr	−5.973 488	−2.871 987	$-1.760\,000 \times 10^{-13}$
Kr	7.891 411	$-1.240\,000 \times 10^{-13}$	1.982 211
Kr	3.961 880	$-7.570\,000 \times 10^{-13}$	5.822 591
Kr	5.973 488	−2.871 987	$-1.110\,000 \times 10^{-12}$
Kr	5.899 684	2.821 067	3.923 708
Kr	5.899 684	−2.821 067	3.923 708
Kr	−4.001 849	−5.772 736	−2.008 715
Kr	$-2.450\,000 \times 10^{-13}$	−5.725 992	1.971 085
Kr	$-3.350\,000 \times 10^{-13}$	−5.725 992	−1.971 085
Kr	−4.001 849	−5.772 736	2.008 715
Kr	3.940 162	5.588 727	5.932 022
Kr	$-9.150\,000 \times 10^{-14}$	5.573 329	5.868 726
Kr	1.981 296	2.729 189	7.780 293
Kr	4.001 849	−5.772 736	−2.008 715
Kr	4.001 849	−5.772 736	2.008 715
Kr	−3.940 162	5.588 727	5.932 022
Kr	−1.981 296	2.729 189	7.780 293
Kr	$1.620\,000 \times 10^{-13}$	$-1.140\,000 \times 10^{-12}$	9.775 757
Kr	−1.981 296	−2.729 189	7.780 293
Kr	1.981 296	−2.729 189	7.780 293
Kr	3.940 162	−5.588 727	5.932 022
Kr	$-2.680\,000 \times 10^{-13}$	−5.573 329	5.868 726
Kr	−3.940 162	−5.588 727	5.932 022
Kr	$-5.230\,000 \times 10^{-13}$	$1.110\,000 \times 10^{-12}$	−9.775 757

Kr	−3.961 880	$7.670\,000 \times 10^{-13}$	−5.822 591
Kr	3.961 880	$1.130\,000 \times 10^{-12}$	−5.822 591
Kr	−1.981 296	2.729 189	−7.780 293
Kr	−1.981 296	−2.729 189	−7.780 293
Kr	1.981 296	2.729 189	−7.780 293
Kr	1.981 296	−2.729 189	−7.780 293
Kr	−7.891 411	$4.330\,000 \times 10^{-13}$	−1.982 211
Kr	−5.899 684	2.821 067	−3.923 708
Kr	−5.899 684	−2.821 067	−3.923 708
Kr	7.891 411	$-1.240\,000 \times 10^{-13}$	−1.982 211
Kr	5.899 684	2.821 067	−3.923 708
Kr	5.899 684	−2.821 067	−3.923 708
Kr	$-2.400\,000 \times 10^{-13}$	5.573 329	−5.868 726
Kr	3.940 162	5.588 727	−5.932 022
Kr	−3.940 162	5.588 727	−5.932 022
Kr	$-8.040\,000 \times 10^{-14}$	−5.573 329	−5.868 726
Kr	3.940 162	−5.588 727	−5.932 022
Kr	−3.940 162	−5.588 727	−5.932 022

I_2Kr_{182}

TABLE 14. I_2Kr_{182} equilibrium coordinates

Atom	x (Å)	y (Å)	z (Å)
I	$7.540\,000 \times 10^{-14}$	$9.950\,000 \times 10^{-14}$	−1.334 650
I	$-7.290\,000 \times 10^{-14}$	$2.130\,000 \times 10^{-13}$	1.334 650

Kr	$4.400\,000 \times 10^{-14}$	$1.810\,000 \times 10^{-13}$	$-5.722\,345$
Kr	$-3.969\,131$	$2.630\,000 \times 10^{-13}$	$-1.915\,229$
Kr	$3.969\,131$	$1.310\,000 \times 10^{-13}$	$-1.915\,229$
Kr	$-1.960\,725$	$2.791\,034$	$-3.839\,238$
Kr	$-1.960\,725$	$-2.791\,034$	$-3.839\,238$
Kr	$2.118\,206$	$3.054\,473$	$-2.110\,000 \times 10^{-13}$
Kr	$2.118\,206$	$-3.054\,473$	$1.930\,000 \times 10^{-13}$
Kr	$1.960\,725$	$2.791\,034$	$-3.839\,238$
Kr	$1.960\,725$	$-2.791\,034$	$-3.839\,238$
Kr	$-2.118\,206$	$3.054\,473$	$4.950\,000 \times 10^{-13}$
Kr	$-2.118\,206$	$-3.054\,473$	$-2.690\,000 \times 10^{-13}$
Kr	$-3.969\,131$	$2.630\,000 \times 10^{-13}$	$1.915\,229$
Kr	$3.969\,131$	$4.330\,000 \times 10^{-13}$	$1.915\,229$
Kr	$-1.710\,000 \times 10^{-13}$	$-2.420\,000 \times 10^{-13}$	$5.722\,345$
Kr	$-1.960\,725$	$2.791\,034$	$3.839\,238$
Kr	$-1.960\,725$	$-2.791\,034$	$3.839\,238$
Kr	$1.960\,725$	$2.791\,034$	$3.839\,238$
Kr	$1.960\,725$	$-2.791\,034$	$3.839\,238$
Kr	$-2.420\,000 \times 10^{-13}$	$-2.980\,000 \times 10^{-13}$	$-9.708\,622$
Kr	$-3.926\,145$	$-3.300\,000 \times 10^{-13}$	$-5.817\,875$
Kr	$3.926\,145$	$6.430\,000 \times 10^{-13}$	$-5.817\,875$
Kr	$1.961\,158$	$2.765\,131$	$-7.767\,444$
Kr	$1.961\,158$	$-2.765\,131$	$-7.767\,444$
Kr	$-1.961\,158$	$2.765\,131$	$-7.767\,444$
Kr	$-1.961\,158$	$-2.765\,131$	$-7.767\,444$

Kr	$-7.867\,344$	$-1.850\,000 \times 10^{-13}$	$-1.950\,151$
Kr	$-5.951\,720$	$2.840\,207$	$-2.960\,000 \times 10^{-13}$
Kr	$-5.951\,720$	$-2.840\,207$	$-8.930\,000 \times 10^{-14}$
Kr	$-5.886\,717$	$2.806\,659$	$-3.893\,211$
Kr	$-5.886\,717$	$-2.806\,659$	$-3.893\,211$
Kr	$7.867\,344$	$3.060\,000 \times 10^{-13}$	$-1.950\,151$
Kr	$5.886\,717$	$2.806\,659$	$-3.893\,211$
Kr	$5.886\,717$	$-2.806\,659$	$-3.893\,211$
Kr	$5.951\,720$	$2.840\,207$	$5.660\,000 \times 10^{-13}$
Kr	$5.951\,720$	$-2.840\,207$	$-2.460\,000 \times 10^{-13}$
Kr	$-3.917\,722$	$5.576\,120$	$-5.865\,675$
Kr	$-2.390\,000 \times 10^{-13}$	$5.652\,517$	$-1.965\,985$
Kr	$2.980\,000 \times 10^{-13}$	$5.572\,670$	$-5.847\,315$
Kr	$-3.988\,470$	$5.684\,939$	$-1.986\,816$
Kr	$-3.917\,722$	$-5.576\,120$	$-5.865\,675$
Kr	$1.960\,000 \times 10^{-13}$	$-5.652\,517$	$-1.965\,985$
Kr	$-3.120\,000 \times 10^{-13}$	$-5.572\,670$	$-5.847\,315$
Kr	$-3.988\,470$	$-5.684\,939$	$-1.986\,816$
Kr	$3.988\,470$	$5.684\,939$	$1.986\,816$
Kr	$3.988\,470$	$5.684\,939$	$-1.986\,816$
Kr	$-2.790\,000 \times 10^{-13}$	$5.652\,517$	$1.965\,985$
Kr	$3.988\,470$	$-5.684\,939$	$1.986\,816$
Kr	$3.988\,470$	$-5.684\,939$	$-1.986\,816$
Kr	$-2.010\,000 \times 10^{-14}$	$-5.652\,517$	$1.965\,985$
Kr	$3.917\,722$	$5.576\,120$	$-5.865\,675$

Kr	3.917 722	−5.576 120	−5.865 675
Kr	−3.988 470	5.684 939	1.986 816
Kr	−3.988 470	−5.684 939	1.986 816
Kr	−7.867 344	$1.140\,000 \times 10^{-13}$	1.950 151
Kr	−3.926 145	$2.030\,000 \times 10^{-13}$	5.817 875
Kr	−5.886 717	2.806 659	3.893 211
Kr	−5.886 717	−2.806 659	3.893 211
Kr	7.867 344	$-2.840\,000 \times 10^{-14}$	1.950 151
Kr	3.926 145	$2.880\,000 \times 10^{-13}$	5.817 875
Kr	5.886 717	2.806 659	3.893 211
Kr	5.886 717	−2.806 659	3.893 211
Kr	$1.150\,000 \times 10^{-13}$	$-3.340\,000 \times 10^{-13}$	9.708 622
Kr	1.961 158	2.765 131	7.767 444
Kr	1.961 158	−2.765 131	7.767 444
Kr	−1.961 158	2.765 131	7.767 444
Kr	−1.961 158	−2.765 131	7.767 444
Kr	$2.260\,000 \times 10^{-14}$	5.572 670	5.847 315
Kr	−3.917 722	5.576 120	5.865 675
Kr	$-1.960\,000 \times 10^{-13}$	−5.572 670	5.847 315
Kr	−3.917 722	−5.576 120	5.865 675
Kr	3.917 722	5.576 120	5.865 675
Kr	3.917 722	−5.576 120	5.865 675
Kr	$-5.140\,000 \times 10^{-13}$	$1.170\,000 \times 10^{-12}$	−13.742 770
Kr	−3.963 596	$4.800\,000 \times 10^{-13}$	−9.772 121
Kr	3.963 596	$1.600\,000 \times 10^{-13}$	−9.772 121

Kr	−1.988 431	2.740 892	−11.741 899
Kr	−1.988 431	−2.740 892	−11.741 899
Kr	1.988 431	2.740 892	−11.741 899
Kr	1.988 431	−2.740 892	−11.741 899
Kr	−7.869 874	$8.530\,000 \times 10^{-14}$	−5.888 487
Kr	−5.916 970	2.777 049	−7.837 175
Kr	−5.916 970	−2.777 049	−7.837 175
Kr	7.869 874	$6.680\,000 \times 10^{-13}$	−5.888 487
Kr	5.916 970	2.777 049	−7.837 175
Kr	5.916 970	−2.777 049	−7.837 175
Kr	$-5.730\,000 \times 10^{-13}$	5.533 719	−9.778 217
Kr	3.955 404	5.535 620	−9.807 699
Kr	$4.260\,000 \times 10^{-14}$	−5.533 719	−9.778 217
Kr	3.955 404	−5.535 620	−9.807 699
Kr	−3.955 404	5.535 620	−9.807 699
Kr	−3.955 404	−5.535 620	−9.807 699
Kr	−11.826 190	$-5.150\,000 \times 10^{-13}$	−1.986 931
Kr	−9.837 050	2.788 928	−3.957 481
Kr	−9.837 050	−2.788 928	−3.957 481
Kr	−9.862 536	2.808 873	$2.270\,000 \times 10^{-13}$
Kr	−9.862 536	−2.808 873	$-4.110\,000 \times 10^{-13}$
Kr	−7.905 164	5.635 955	−1.975 832
Kr	−7.905 164	5.635 955	1.975 832
Kr	−7.905 164	−5.635 955	−1.975 832
Kr	−7.905 164	−5.635 955	1.975 832

Kr	−7.864 959	5.585 233	−5.921 954
Kr	−7.864 959	−5.585 233	−5.921 954
Kr	11.826 190	$4.550\,000 \times 10^{-13}$	−1.986 931
Kr	9.862 536	2.808 873	$5.680\,000 \times 10^{-13}$
Kr	9.862 536	−2.808 873	$-7.940\,000 \times 10^{-13}$
Kr	9.837 050	2.788 928	−3.957 481
Kr	9.837 050	−2.788 928	−3.957 481
Kr	7.905 164	5.635 955	−1.975 832
Kr	7.864 959	5.585 233	−5.921 954
Kr	7.905 164	−5.635 955	−1.975 832
Kr	7.864 959	−5.585 233	−5.921 954
Kr	7.905 164	5.635 955	1.975 832
Kr	7.905 164	−5.635 955	1.975 832
Kr	−5.912 559	8.379 871	−7.907 628
Kr	−1.967 960	8.450 325	−3.937 798
Kr	−1.968 137	8.375 478	−7.854 865
Kr	−5.913 842	8.456 395	−3.967 901
Kr	1.977 450	8.450 707	$1.480\,000 \times 10^{-13}$
Kr	1.967 960	8.450 325	−3.937 798
Kr	−1.977 450	8.450 707	$1.780\,000 \times 10^{-13}$
Kr	1.968 137	8.375 478	−7.854 865
Kr	−5.931 965	8.478 443	$2.840\,000 \times 10^{-13}$
Kr	−5.912 559	−8.379 871	−7.907 628
Kr	−1.967 960	−8.450 325	−3.937 798
Kr	−1.968 137	−8.375 478	−7.854 865

Kr	−5.913 842	−8.456 395	−3.967 901
Kr	1.977 450	−8.450 707	$-3.670\,000 \times 10^{-13}$
Kr	1.967 960	−8.450 325	−3.937 798
Kr	−1.977 450	−8.450 707	$-7.410\,000 \times 10^{-13}$
Kr	1.968 137	−8.375 478	−7.854 865
Kr	−5.931 965	−8.478 443	$1.860\,000 \times 10^{-13}$
Kr	5.913 842	8.456 395	3.967 901
Kr	5.931 965	8.478 443	$3.780\,000 \times 10^{-13}$
Kr	1.967 960	8.450 325	3.937 798
Kr	5.913 842	8.456 395	−3.967 901
Kr	−1.967 960	8.450 325	3.937 798
Kr	5.913 842	−8.456 395	3.967 901
Kr	5.931 965	−8.478 443	$-4.100\,000 \times 10^{-13}$
Kr	1.967 960	−8.450 325	3.937 798
Kr	5.913 842	−8.456 395	−3.967 901
Kr	−1.967 960	−8.450 325	3.937 798
Kr	5.912 559	8.379 871	−7.907 628
Kr	5.912 559	−8.379 871	−7.907 628
Kr	−5.913 842	8.456 395	3.967 901
Kr	−5.913 842	−8.456 395	3.967 901
Kr	−11.826 190	$-7.460\,000 \times 10^{-14}$	1.986 931
Kr	−7.869 874	$-5.080\,000 \times 10^{-13}$	5.888 487
Kr	−9.837 050	2.788 928	3.957 481
Kr	−9.837 050	−2.788 928	3.957 481
Kr	−3.963 596	$-4.580\,000 \times 10^{-13}$	9.772 121

Kr	−5.916 970	2.777 049	7.837 175
Kr	−5.916 970	−2.777 049	7.837 175
Kr	−7.864 959	5.585 233	5.921 954
Kr	−7.864 959	−5.585 233	5.921 954
Kr	11.826 190	$2.840\,000 \times 10^{-14}$	1.986 931
Kr	7.869 874	$1.390\,000 \times 10^{-13}$	5.888 487
Kr	9.837 050	2.788 928	3.957 481
Kr	9.837 050	−2.788 928	3.957 481
Kr	3.963 596	$-2.060\,000 \times 10^{-13}$	9.772 121
Kr	5.916 970	2.777 049	7.837 175
Kr	5.916 970	−2.777 049	7.837 175
Kr	7.864 959	5.585 233	5.921 954
Kr	7.864 959	−5.585 233	5.921 954
Kr	$-3.750\,000 \times 10^{-13}$	$-4.480\,000 \times 10^{-13}$	13.742 770
Kr	−1.988 431	2.740 892	11.741 899
Kr	−1.988 431	−2.740 892	11.741 899
Kr	1.988 431	2.740 892	11.741 899
Kr	1.988 431	−2.740 892	11.741 899
Kr	3.955 404	5.535 620	9.807 699
Kr	$1.030\,000 \times 10^{-13}$	5.533 719	9.778 217
Kr	3.955 404	−5.535 620	9.807 699
Kr	$-1.380\,000 \times 10^{-13}$	−5.533 719	9.778 217
Kr	−3.955 404	5.535 620	9.807 699
Kr	−3.955 404	−5.535 620	9.807 699
Kr	1.968 137	8.375 478	7.854 865

Kr	−1.968 137	8.375 478	7.854 865
Kr	−5.912 559	8.379 871	7.907 628
Kr	1.968 137	−8.375 478	7.854 865
Kr	−1.968 137	−8.375 478	7.854 865
Kr	−5.912 559	−8.379 871	7.907 628
Kr	5.912 559	8.379 871	7.907 628
Kr	5.912 559	−8.379 871	7.907 628

Multidimensional Gaussian Wave Packet

A strong motivation for developing FVB/GB is improving upon purely semiclassical Gaussian wave packet methods. Originally proposed by Heller [31] as a route to simulation of dynamics during photodissociation processes, these methods are optimal for short-time and purely dissociative wave packet motion. To gauge the utility of the FVB/GB ansatz over a standard Gaussian wave packet form, we preform calculations for I_2Kr_6 where both totally symmetric modes in the model are assumed to have a Gaussian form. In these calculations, the bound two-dimensional potential energy surface on which the dynamics take place is highly anharmonic. We'll see that this anharmonicity leads to rapid failure of standard Gaussian wave packet methods while FVB/GB continues to accurately track the dynamics of the system. Below are the DFM variational equations resulting from a general multidimensional Gaussian ansatz for the wave function of the total system.

The nuclear Hamiltonian for the total system in a given electronic state has the form

$$H = \frac{P \cdot P}{2} + V(Q), \tag{A.6}$$

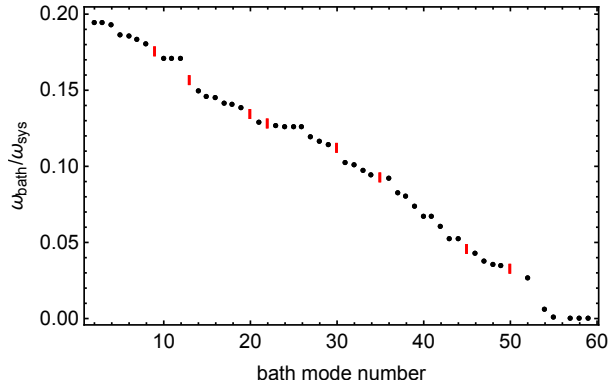

FIGURE 46. Frame shows dimensionless bath frequencies of I_2Kr_{18} in terms of the ground state system frequency. The frequencies of the 8 totally symmetric bath modes in this model are identified by red bars.

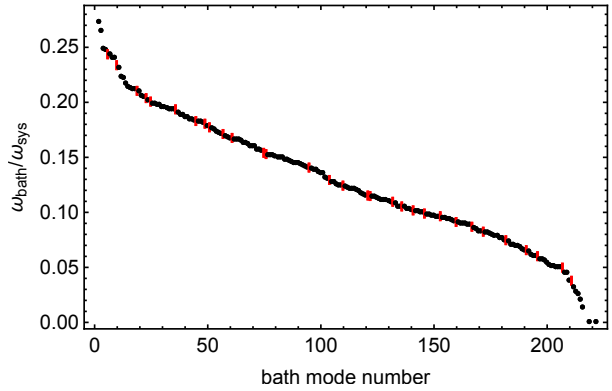

FIGURE 47. Frame shows dimensionless bath frequencies of I_2Kr_{72} in terms of the ground state system frequency. The frequencies of the 31 totally symmetric bath modes in this model are identified by red bars.

where both P and Q are N-dimensional vectors. The Gaussian ansatz for the multidimensional wave packet is chosen to be

$$\langle Q|\Psi\rangle = a\exp\{Q\cdot\alpha\cdot Q+\beta\cdot Q+i\gamma\}. \tag{A.7}$$

In Eq. (A.7), a and γ are real-valued scalars, β is an N-dimensional complex vector with $\beta = \beta' + i\beta''$ and α is an $N\times N$ dimensional complex symmetric matrix

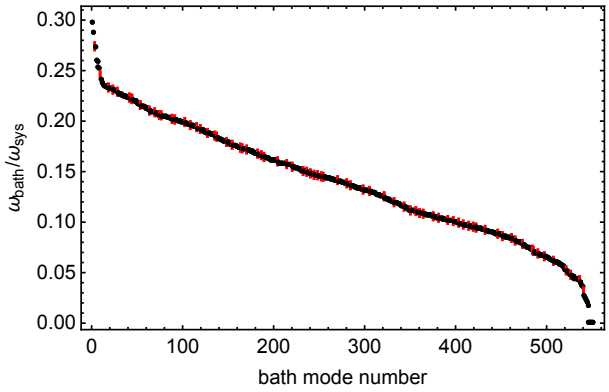

FIGURE 48. Plot of bath frequencies of the model I_2Kr_{182} made dimensionless by division with the ground state system frequency. The 76 red bars indicate the frequencies of the totally symmetric bath modes in this model.

where $\alpha = \alpha' + i\alpha''$. Note that the coupling between different coordinates lies in the off-diagonal elements of α.

Following the derivation in the main text, we first find an expression for the matrix M. As found from the DFM variational principle, the mn^{th} element of this matrix is $M_{mn} = \text{Re}\langle\Psi_m|\Psi_n\rangle$. Given that there are six wave packet parameters (albeit with different dimensions) that specify the state, we can represent M as a 6×6 matrix. Note well however that this is just a representation, M is truly a tensor whose whose elements range in size from scalars to fourth-rank-tensors. Proceeding in this way,

$$M = \begin{bmatrix} \langle\Psi_a|\Psi_a\rangle & 0 & \langle\Psi_a|\Psi_{\beta'}\rangle & 0 & \langle\Psi_a|\Psi_{\alpha'}\rangle & 0 \\ 0 & \langle\Psi_\gamma|\Psi_\gamma\rangle & 0 & \langle\Psi_\gamma|\Psi_{\beta''}\rangle & 0 & \langle\Psi_\gamma|\Psi_{\alpha''}\rangle \\ \langle\Psi_{\beta'}|\Psi_a\rangle & 0 & \langle\Psi_{\beta'}|\Psi_{\beta'}\rangle & 0 & \langle\Psi_{\beta'}|\Psi_{\alpha'}\rangle & 0 \\ 0 & \langle\Psi_{\beta''}|\Psi_\gamma\rangle & 0 & \langle\Psi_{\beta''}|\Psi_{\beta''}\rangle & 0 & \langle\Psi_{\beta''}|\Psi_{\alpha''}\rangle \\ \langle\Psi_{\alpha'}|\Psi_a\rangle & 0 & \langle\Psi_{\alpha'}|\Psi_{\beta'}\rangle & 0 & \langle\Psi_{\alpha'}|\Psi_{\alpha'}\rangle & 0 \\ 0 & \langle\Psi_{\alpha''}|\Psi_\gamma\rangle & 0 & \langle\Psi_{\alpha''}|\Psi_{\beta''}\rangle & 0 & \langle\Psi_{\alpha''}|\Psi_{\alpha''}\rangle \end{bmatrix}. \quad \text{(A.8)}$$

To simplify this expression, we evaluate derivatives of the multidimensional wave packet with respect to the six wave packet parameters. We have

$$\langle Q|\Psi_a\rangle = \frac{\partial}{\partial a}\langle Q|\Psi\rangle = \frac{\langle Q|\Psi\rangle}{a}, \tag{A.9}$$

$$\langle Q|\Psi_\gamma\rangle = i\langle Q|\Psi\rangle, \tag{A.10}$$

$$\langle Q|\Psi_{\beta'_j}\rangle = \frac{\partial}{\partial \beta'_j}\langle Q|\Psi\rangle = Q_j\langle Q|\Psi\rangle \implies \langle Q|\Psi_{\beta'}\rangle = Q\langle Q|\Psi\rangle, \tag{A.11}$$

$$\langle Q|\Psi_{\beta''}\rangle = iQ\langle Q|\Psi\rangle, \tag{A.12}$$

$$\langle Q|\Psi_{\alpha'_{jk}}\rangle = \frac{\partial}{\partial \alpha'_{jk}}\langle Q|\Psi\rangle = Q_jQ_k\langle Q|\Psi\rangle \implies \langle Q|\Psi_{\alpha'}\rangle = QQ\langle Q|\Psi\rangle, \tag{A.13}$$

$$\langle Q|\Psi_{\alpha''}\rangle = iQQ\langle Q|\Psi\rangle, \tag{A.14}$$

With these terms at hand, M now has the form

$$M = \begin{bmatrix} \frac{1}{a^2}\langle\Psi|\Psi\rangle & 0 & \frac{1}{a}\langle\Psi|Q|\Psi\rangle & 0 & \frac{1}{a}\langle\Psi|QQ|\Psi\rangle & 0 \\ 0 & \langle\Psi|\Psi\rangle & 0 & \langle\Psi|Q|\Psi\rangle & 0 & \langle\Psi|QQ|\Psi\rangle \\ \frac{1}{a}\langle\Psi|Q|\Psi\rangle & 0 & \langle\Psi|QQ|\Psi\rangle & 0 & \langle\Psi|QQQ|\Psi\rangle & 0 \\ 0 & \langle\Psi|Q|\Psi\rangle & 0 & \langle\Psi|QQ|\Psi\rangle & 0 & \langle\Psi|QQQ|\Psi\rangle \\ \frac{1}{a}\langle\Psi|QQ|\Psi\rangle & 0 & \langle\Psi|QQQ|\Psi\rangle & 0 & \langle\Psi|QQQQ|\Psi\rangle & 0 \\ 0 & \langle\Psi|QQ|\Psi\rangle & 0 & \langle\Psi|QQQ|\Psi\rangle & 0 & \langle\Psi|QQQQ|\Psi\rangle \end{bmatrix}, \tag{A.15}$$

with

$$\langle\Psi|\Psi\rangle \equiv I_0 = \int dQ\ \langle\Psi|Q\rangle\langle Q|\Psi\rangle = a^2 \exp\Big\{-\tfrac{1}{2}(\beta'\cdot(\alpha')^{-1}\cdot\beta')\Big\}\sqrt{\frac{\pi^N}{(-2)^N\det(\alpha')}}, \tag{A.16}$$

$$\langle\Psi|Q_j|\Psi\rangle \equiv I_1 = -\frac{1}{2}\Big[\beta'\cdot(\alpha')^{-1}\Big]_j I_0, \tag{A.17}$$

$$\langle\Psi|Q_jQ_k|\Psi\rangle \equiv I_2 = -\frac{1}{4}\Big\{\Big[(\alpha')^{-1}\Big]_{jk} - \Big[(\alpha')^{-1}\cdot\beta'\Big]_j\Big[\beta'\cdot(\alpha')^{-1}\Big]_k\Big\}I_0, \tag{A.18}$$

$$\begin{aligned}\langle\Psi|Q_jQ_kQ_l|\Psi\rangle \equiv I_3 = \frac{1}{8}\Big\{&\Big[(\alpha')^{-1}\Big]_{jl}\Big[(\alpha')^{-1}\cdot\beta'\Big]_k + \Big[(\alpha')^{-1}\Big]_{kl}\Big[(\alpha')^{-1}\cdot\beta'\Big]_j \\ &+ \Big[(\alpha')^{-1}\Big]_{jk}\Big[(\alpha')^{-1}\cdot\beta'\Big]_l - \Big[(\alpha')^{-1}\cdot\beta'\Big]_j\Big[(\alpha')^{-1}\cdot\beta'\Big]_k\Big[(\alpha')^{-1}\cdot\beta'\Big]_l\Big\}I_0,\end{aligned} \tag{A.19}$$

$$\begin{aligned}\langle\Psi|Q_iQ_jQ_kQ_l|\Psi\rangle \equiv I_4 = \frac{1}{16}\Big\{&\Big[(\alpha')^{-1}\Big]_{ij}\Big[(\alpha')^{-1}\Big]_{kl} + \Big[(\alpha')^{-1}\Big]_{kj}\Big[(\alpha')^{-1}\Big]_{il} + \Big[(\alpha')^{-1}\Big]_{jl}\Big[(\alpha')^{-1}\Big]_{ik} \\ &- \Big[(\alpha')^{-1}\Big]_{ij}\Big[\beta'\cdot(\alpha')^{-1}\Big]_k\Big[\beta'\cdot(\alpha')^{-1}\Big]_l - \Big[(\alpha')^{-1}\Big]_{ik}\Big[\beta'\cdot(\alpha')^{-1}\Big]_j\Big[\beta'\cdot(\alpha')^{-1}\Big]_l \\ &- \Big[(\alpha')^{-1}\Big]_{il}\Big[\beta'\cdot(\alpha')^{-1}\Big]_j\Big[\beta'\cdot(\alpha')^{-1}\Big]_k - \Big[(\alpha')^{-1}\Big]_{kl}\Big[\beta'\cdot(\alpha')^{-1}\Big]_i\Big[\beta'\cdot(\alpha')^{-1}\Big]_j \\ &- \Big[(\alpha')^{-1}\Big]_{jk}\Big[\beta'\cdot(\alpha')^{-1}\Big]_i\Big[\beta'\cdot(\alpha')^{-1}\Big]_l - \Big[(\alpha')^{-1}\Big]_{jl}\Big[\beta'\cdot(\alpha')^{-1}\Big]_i\Big[\beta'\cdot(\alpha')^{-1}\Big]_k \\ &+ \Big[\beta'\cdot(\alpha')^{-1}\Big]_i\Big[\beta'\cdot(\alpha')^{-1}\Big]_j\Big[\beta'\cdot(\alpha')^{-1}\Big]_k\Big[\beta'\cdot(\alpha')^{-1}\Big]_l\Big\}I_0.\end{aligned} \tag{A.20}$$

Moving onto the tensor χ, recalling from the main text that $\chi_m = \mathrm{Im}\langle\Psi_m|H|\Psi\rangle$, we represent χ as a 6×1 vector:

$$\chi = \begin{bmatrix}\chi_a \\ \chi_\gamma \\ \chi_{\beta'} \\ \chi_{\beta''} \\ \chi_{\alpha'} \\ \chi_{\alpha''}\end{bmatrix}, \tag{A.21}$$

with

$$\chi_a = 0, \tag{A.22}$$

$$\chi_\gamma = \Big\{\frac{1}{2}\,\mathrm{Tr}\left[\alpha' + \alpha''\cdot(\alpha')^{-1}\cdot\alpha''\right] + \beta''\cdot\alpha''\cdot(\alpha')^{-1}\cdot\beta' - \frac{1}{2}\beta''\cdot\beta'' \\ - \frac{1}{2}\beta'\cdot(\alpha')^{-1}\cdot\alpha''\cdot\alpha''\cdot(\alpha')^{-1}\cdot\beta'\Big\}I_0 - \langle\Psi|U(Q)|\Psi\rangle, \quad \text{(A.23)}$$

$$\chi_{\beta'_j} = \frac{1}{2}\Big\{\beta''_j - \left[\beta'\cdot(\alpha')^{-1}\cdot\alpha''\right]_j\Big\}I_0, \quad \text{(A.24)}$$

$$\chi_{\beta''_j} = \Big\{\Big(- \frac{1}{4}\,\mathrm{Tr}\left[\alpha' + \alpha''\cdot(\alpha')^{-1}\cdot\alpha''\right] + \frac{1}{4}\beta''\cdot\beta'' - \frac{1}{2}\beta'\cdot(\alpha')^{-1}\cdot\alpha''\cdot\beta'' \\ + \frac{1}{4}\beta'\cdot(\alpha')^{-1}\cdot\alpha''\cdot\alpha''\cdot(\alpha')^{-1}\cdot\beta'\Big)\left[\beta'\cdot(\alpha')^{-1}\right]_j \\ + \frac{1}{2}\left[(\alpha')^{-1}\cdot\alpha''\cdot\beta''\right]_j - \frac{1}{2}\left[\beta'\cdot(\alpha')^{-1}\cdot\alpha''\cdot\alpha''\cdot(\alpha')^{-1}\right]_j\Big\}I_0 - \langle\Psi|Q_jU(Q)|\Psi\rangle, \quad \text{(A.25)}$$

$$\chi_{\alpha'_{jk}} = \frac{1}{4}\Big\{\left[(\alpha')^{-1}\cdot\beta'\right]_j\left[\beta'\cdot(\alpha')^{-1}\cdot\alpha''\right]_k - \left[(\alpha')^{-1}\cdot\beta'\right]_j\left[\beta''\right]_k + \left[\alpha''\cdot(\alpha')^{-1}\cdot\beta'\right]_j\left[\beta'\cdot(\alpha')^{-1}\right]_k \\ - \left[\beta''\right]_j\left[\beta'\cdot(\alpha')^{-1}\right]_k - \left[(\alpha')^{-1}\cdot\alpha''\right]_{jk} - \left[\alpha''\cdot(\alpha')^{-1}\right]_{jk}\Big\}I_0, \quad \text{(A.26)}$$

$$\chi_{\alpha''_{jk}} = \frac{1}{4}\Big\{\Big(\left[(\alpha')^{-1}\cdot\beta'\right]_j\left[\beta'\cdot(\alpha')^{-1}\right]_k - \left[(\alpha')^{-1}\right]_{jk}\Big)\Big(-\frac{1}{2}\beta''\cdot\beta'' + \frac{1}{2}\,\mathrm{Tr}\left[\alpha' + \alpha''\cdot(\alpha')^{-1}\cdot\alpha''\right] \\ + \beta'\cdot(\alpha')^{-1}\cdot\alpha''\cdot\beta'' - \frac{1}{2}\beta'\cdot(\alpha')^{-1}\cdot\alpha''\cdot\alpha''\cdot(\alpha')^{-1}\cdot\beta'\Big) \\ - \left[(\alpha')^{-1}\cdot\beta'\right]_j\left[(\alpha')^{-1}\cdot\alpha''\cdot\beta''\right]_k - \left[(\alpha')^{-1}\cdot\alpha''\cdot\beta''\right]_j\left[\beta'\cdot(\alpha')^{-1}\right]_k \\ + \left[(\alpha')^{-1}\cdot\beta'\right]_j\left[(\alpha')^{-1}\cdot\alpha''\cdot\alpha''\cdot(\alpha')^{-1}\cdot\beta'\right]_k + \left[(\alpha')^{-1}\cdot\alpha''\cdot\alpha''\cdot(\alpha')^{-1}\cdot\beta'\right]_j\left[\beta'\cdot(\alpha')^{-1}\right]_k \\ + \left[\mathbb{1} - (\alpha')^{-1}\cdot\alpha''\cdot\alpha''\cdot(\alpha')^{-1}\right]_{jk}\Big\}I_0 - \langle\Psi|Q_jQ_kU(Q)|\Psi\rangle. \quad \text{(A.27)}$$

Implementing the expressions for M and χ in the equation:

$$\dot{\lambda} = M^{-1} \cdot \chi, \tag{A.28}$$

we numerically propagated the parameters through time using a fourth-order Runge-Kutta integration algorithm. The successful propagation of the two dimensional Gaussian wave packet for approximately 60 fs required the use of a 10 zeptosecond time-step as compared with the 100 femtosecond time-step used in FVB/GB calculations out to 2320 fs. Results from these calculations are shown below. Figures (49.), (51.) and (52.) clearly show the stability of the FVB/GB ansatz over Gaussian wave packet methods for this model system.

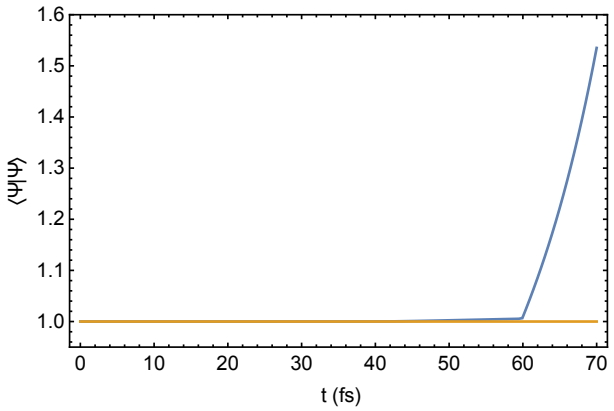

FIGURE 49. Plot of the norm for the two dimensional Gaussian wave packet (blue) and FVB/GB wave packet (orange). The abrupt onset of norm non-conservation at 60 fs in the GWP calculation indicates inaccurate integration of the DFM equations. The FVB/GB norm trace has a value of one out to 700 fs before showing slight variations in the norm for this system.

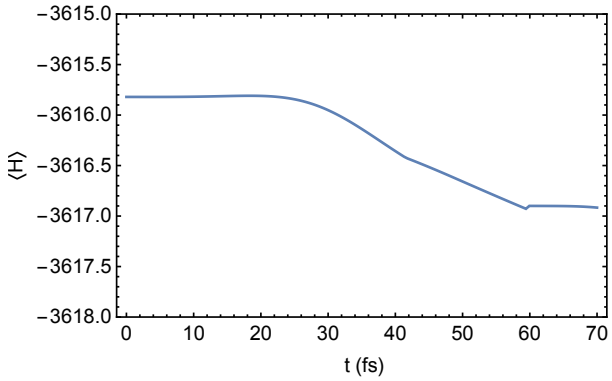

FIGURE 50. Frame shows the energy of the model during propagation of the two-dimensional wave packet. At 20 fs the energy ceases to be conserved indicating a failure of the ansatz. Twenty femtoseconds later the energy appears to begin changing at a near constant rate before an abrupt shift at 60 fs.

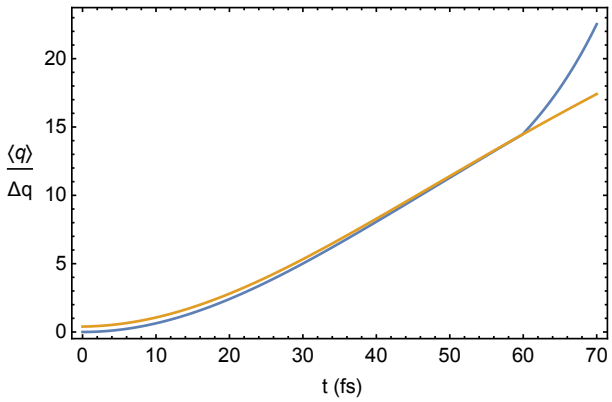

FIGURE 51. Comparison between the two-dimensional Gaussian ansatz and FVB/GB in the calculation of the expectation value of the system coordinate. The FVB/GB result is shifted slightly up from zero initially due to truncation of system levels in the calculation.

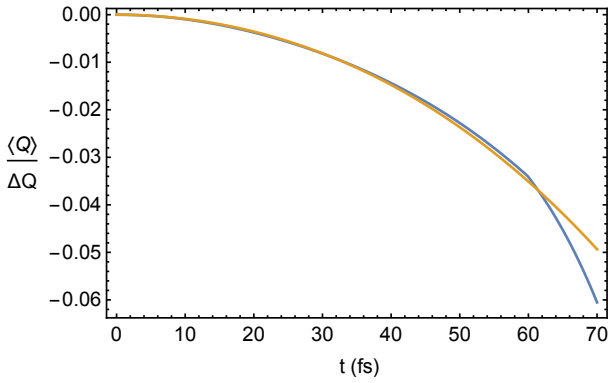

FIGURE 52. Comparison between the two-dimensional Gaussian ansatz and FVB/GB in the calculation of the expectation value of the bath coordinate. The divergence between the two trajectories occurs at approximately 60 fs.

APPENDIX B

TA APPENDIX

Surviving Dipole Elements

Here are formulas for the four dipole matrix elements among those listed in Eqs. (3.7) and (3.8) that contribute to the transient-transmission signal. For GSB, we find

$$\langle 0|\hat{m}|\uparrow_u\downarrow_u\uparrow_r\rangle = -imF_u^2F_re^{-i\varphi_r}e^{i\epsilon_0 t} \times\left\langle\psi_0|e^{-iH_e(t-t_d)}p^{(eg)}(t-t_d;\tau)e^{-iH_gt_d}p^{(ge)}(\tau+t_d;\bar{\tau})p^{(eg)}(\bar{\tau};\bar{\bar{\tau}})|\psi_0\right\rangle\,; \tag{B.1}$$

for SE,

$$\langle\uparrow_u|\hat{m}|\uparrow_u\downarrow_r\rangle = imF_u^2F_re^{i\varphi_r} \times\left\langle\psi_0|p^{(ge)}(t;\tau')e^{iH_et}e^{-iH_g(t-t_d)}p^{(ge)}(t-t_d;\tau)e^{-iH_et_d}p^{(eg)}(\tau+t_d;\bar{\tau})|\psi_0\right\rangle\,; \tag{B.2}$$

for GSB′,

$$\langle 0|\hat{m}|\uparrow_r\downarrow_u\uparrow_u\rangle = -imF_u^2F_re^{-i\varphi_r}e^{i\epsilon_0(t-t_d)} \times\left\langle\psi_0|e^{-iH_et}p^{(eg)}(t;\tau)p^{(ge)}(\tau;\bar{\tau})e^{iH_et_d}p^{(eg)}(\bar{\tau}-t_d;\bar{\bar{\tau}})|\psi_0\right\rangle\,; \tag{B.3}$$

and for SE′,

$$\langle\uparrow_r|\hat{m}|\uparrow_u\downarrow_u\rangle = imF_u^2F_re^{i\varphi_r}e^{i\epsilon_0t_d} \times\langle\psi_0|p^{(ge)}(t-t_d;\tau')e^{iH_e(t-t_d)}e^{-iH_gt}p^{(ge)}(t;\tau)p^{(eg)}(\tau;\bar{\tau})|\psi_0\rangle\,. \tag{B.4}$$

$\Delta U(\bar{\omega})$ as a Time Integral

Letting $m(t)$ stand for $m_{u^2 r}(t)$ in this appendix, we may write Eq. (3.5) as

$$\Delta U(\bar{\omega}) = -\frac{1}{4\pi^2 c^2} \int_{\bar{\omega}-\frac{\delta\omega}{2}}^{\bar{\omega}+\frac{\delta\omega}{2}} \mathrm{d}\omega \, e^{-i\omega t} \tilde{E}_r(\omega) J \, + \, \text{c.c.} \,, \tag{B.5}$$

where the

$$\tilde{E}_r(\omega) = \int_{-\infty}^{\infty} \mathrm{d}t \, e^{i\omega t} E_r(t) \,, \tag{B.6}$$

are Fourier components of the probe electric field, and

$$\begin{aligned} J &= \int \frac{\mathrm{d}^3 R}{R} \, e^{i\omega Z/c} \, \ddot{m}\left(t - \frac{R}{c}\right) \\ &= \frac{2\pi c}{i\omega} \int_0^{\infty} \mathrm{d}R \, \ddot{m}\left(t - \frac{R}{c}\right) \left(e^{i\omega R/c} - e^{-i\omega R/c}\right) \,. \end{aligned} \tag{B.7}$$

Upon substitution, we get

$$\begin{aligned} \Delta U(\bar{\omega}) = \frac{i}{2\pi c} &\int_0^{\infty} \mathrm{d}R \, \ddot{m}\left(t - \frac{R}{c}\right) \\ &\times \int_{\bar{\omega}-\frac{\delta\omega}{2}}^{\bar{\omega}+\frac{\delta\omega}{2}} \frac{\mathrm{d}\omega}{\omega} \, \tilde{E}_r(\omega) \left\{ e^{-i\omega\left(t-\frac{R}{c}\right)} - e^{-i\omega\left(t+\frac{R}{c}\right)} \right\} + \text{c.c.} \,. \end{aligned} \tag{B.8}$$

As the spectrally filtered probe is to lie entirely in the far-field region, the observation time must obey $t > \delta\omega/2$. Since $t\,\delta\omega$ is therefore much greater than unity, the second term inside curly brackets in Eq. (B.8) makes no contribution to the integral. Letting $\bar{t} = t - R/c$, whence $dR = -c\,d\bar{t}$, we find

$$\begin{aligned} \Delta U(\bar{\omega}) = \, &- \frac{1}{2\pi} \int_{-\infty}^{\infty} \mathrm{d}\bar{t} \, \ddot{m}(\bar{t}) \\ &\times \int_{\bar{\omega}-\frac{\delta\omega}{2}}^{\bar{\omega}+\frac{\delta\omega}{2}} \mathrm{d}\omega \left\{ \tilde{E}_r(\omega) \frac{e^{-i\omega\bar{t}}}{i\omega} + \text{c.c.} \right\} \,. \end{aligned} \tag{B.9}$$

The upper limit of $\bar{t}$-integration has been extended to plus infinity, because the inner, frequency integral vanishes for $\bar{t}$ in excess of t, irrespective of whether $m(\bar{t})$ persists this long. Integrating twice by parts leads to

$$\begin{aligned} \Delta U(\bar{\omega}) = & -\int_{-\infty}^{\infty} \mathrm{d}t\, \dot{m}(t) E_r'(t) \\ = & \int_{-\infty}^{\infty} \mathrm{d}t\, m(t) \dot{E}_r'(t)\,, \end{aligned} \tag{B.10}$$

which, using the form (3.25) for the filtered probe field (at $\mathbf{R} = \mathbf{0}$), whose carrier wave oscillates rapidly compared to the rise and fall of its envelope, leads directly to Eq. (3.28) in the main text.

REFERENCES CITED

[1] S. D. McClure, D. B. Turner, P. C. Arpin, T. Mirkovic, and G. D. Scholes. Coherent oscillations in the PC577 cryptophyte antenna occur in the excited electronic state. J. Phys. Chem. B, **118**:1296, (2014).

[2] M. Karavitis and V. A. Apkarian. Vibrational coherence of I_2 in solid Kr. J. Chem. Phys., **120**:292, (2004).

[3] R. Zadoyan, J. Almy, and V. A. Apkarian. Lattice dynamics from the "eyes" of the chromophore real-time studies of I_2 isolated in rare gas matrices. Faraday Discuss., **108**:255, (1997).

[4] D. Segale and V. A. Apkarian. Dissipative quantum coherent dynamics probed in phase-space: Electronically resonant 5-color 4-wave mixing on I_2(B) in solid Kr. J. Chem. Phys., **135**:024203, (2011).

[5] T. Kilijunen, M. Bargheer, M. Gühr, and N. Schwentner. A potential energy surface and a trajectory study of photodynamics and strong-field alignment of a ClF molecule in rare gas (Ar,Kr) solids. Phys. Chem. Chem. Phys, **6**:2185, (2004).

[6] R. Zadoyan, Z. Li, C. C. Martens, and V. A. Apkarian. The breaking and remaking of a bond: Caging of I_2 in solid Kr. J. Chem. Phys., **101**:6648, (1994).

[7] E. J. Heller, R. Sundberg, and D. Tannor. Simple aspects of Raman scattering. J. Chem. Phys., **86**:1822, (1982).

[8] W. T. Pollard, S. L. Dexheimer, Q. Wang, L. A. Peteanu, C. V. Shank, and R. A. Mathies. Theory of dynamic absorption spectroscopy of nonstationary states. 4. Application to 12-fs resonant impulsive Raman spectroscopy of bacteriorhodopsin. J. Phys. Chem., **96**:6147, (1992).

[9] E. J. Heller. The semiclassical way to molecular spectroscopy. Acc. Chem. Res., **14**:368, (1981).

[10] N. E. Henriksen and V. Engel. Femtosecond pump-probe spectroscopy: A theoretical analysis of transient signals and their relation to nuclear wave-packet motion. Int. Rev. Phys. Chem., **20**:93, (2001).

[11] D. M. Jonas, S. E. Bradforth, S. A. Passino, and G. R. Fleming. Femtosecond wavepacket spectroscopy: Influence of temperature, wavelength, and pulse duration. J. Phys. Chem., **99**:2594, (1995).

[12] Y.-J. Yan and S. Mukamel. Femtosecond pump-probe spectroscopy of polyatomic molecules in condensed phases. Phys. Rev. A, **41**:6920, (1990).

[13] W. B. Bosma, Y.-J. Yan, and S. Mukamel. Impulsive pump-probe and photon-echo spectroscopies of dye molecules in condensed phases. Phys. Rev. A, **42**:6485, (1990).

[14] M. Yoshizawa and M. Kurosawa. Femtosecond time-resolved Raman spectroscopy using stimulated Raman scattering. Phys. Rev. A, **61**:0138081, (1999).

[15] P. Kukura, D. W. McCamant, and R. A. Mathies. Femtosecond time-resolved stimulated raman spectroscopy of the S_2 ($1B_u^+$) excited state of β-carotene. J. Phys. Chem. A, **108**:5921, (2004).

[16] P. R. Poulin and K. A. Nelson. Irreversible organic crystalline chemistry monitiored in real time. Science, **313**:1756, (2006).

[17] E. T. Branigan, M. N. van Staveren, and V. A. Apkarian. Solidlike coherent vibronic dynamics in a room temperature liquid: Resonant Raman and absorption spectroscopy of liquid bromine. J. Chem. Phys., **132**:044504, (2010).

[18] F. Königsmann, M. Fushitani, N. Owschimikow, D. T. Anderson, and N. Schwentner. Femtosecond pump-probe 2d optical Kerr effect spectroscopy of molecular hydrogen crystals. Chem. Phys. Lett., **458**:303, (2008).

[19] I. U. Goldschleger, M. N. van Staveren, and V. A. Apkarian. Quantum tomography of a molecular bond in ice. J. Chem. Phys., **139**:034201, (2013).

[20] V. Senekerimyan, I. U. Goldschleger, and V. A. Apkarian. Vibronic dynamics of I_2 trapped in amorphous ice: Coherent following of cage relaxtion. J. Chem. Phys., **127**:214511, (2007).

[21] M. Gühr, M. Bargheer, M. Fushitani, T. Kiljunen, and N. Schwentner. Ultrafast dynamics of halogens in rare gas solids. Phys. Chem. Chem. Phys., **9**:779, (2007).

[22] Z. Bihary, R. Zadoyan, M. Karavitis, and V. A. Apkarian. Dynamics and the breaking of a driven cage: I_2 in solid Ar. J. Chem. Phys. , **120**:7576, (2004).

[23] Z. Li, R. Zadoyan, V. A. Apkarian, and C. C. Martens. Femtosecond many-body dynamics of caging:Experiment and simulation of I_2 photodissociation-recombination in solid Ar. J. Phys. Chem., **99**:7453, (1995).

[24] M. Gühr, M. Bargheer, and N. Schwentner. Generation of coherent zone boundary phonons by impulsive excitation of molecules. Phys. Rev. Lett., **91**: 085504, (2003).

[25] J. Lindgren, E. Hulkko, T. Kiviniemi, M. Pettersson, V. A. Apkarian, and T. Kiljunen. Dynamics behind the long-lived coherences of I_2 in solid Xe. J. Phys. Chem. A., **117**:4884, (2013).

[26] M. Karavitis, T. Kumada, I. U. Goldschleger, and V. A. Apkarian. Vibrational dissipation and dephasing of I_2 ($\nu = 1 - 19$) in solid Kr. Phys. Chem. Chem. Phys., **7**:791, (2005).

[27] T. Kiviniemi, J. Aumanen, P. Myllyperkiö, V. A. Apkarian, and M. Pettersson. Time-resolved coherent anti-Stokes Raman-scattering measurements of I_2 in solid Kr: Vibrational dephasing on the ground electronic state at 2.6-32 K. J. Chem. Phys., **123**:064509, (2005).

[28] H. Ibrahim, M. Héjjas, M. Fushitani, and N. Schwentner. Phase sensitive control of vibronic guest-host interaction: Br_2 in Ar matrix. J. Phys. Chem. A. , **113**:7439, (2009).

[29] I. Burghardt, M. Nest, and G. Worth. Multiconfigurational system-bath dynamics using Gaussian wave packets: Energy relaxation and decoherence induced by a finite-dimensional bath. J. Chem. Phys., **119**:5364, (2003).

[30] I. Burghardt, K. Giri, and G. A. Worth. Multimode quantum dynamics using Gaussian wavepackets: The Gaussian-based multiconfiguration time-dependent Hartree method applied to the absorption spectrum of pyrazine. J. Chem. Phys., **129**:174104, (2008).

[31] E. J. Heller. Time-dependent approach to semiclassical dynamics. J. Chem. Phys., **62**:1544, (1975).

[32] E. J. Heller. Time dependent variational approach to semiclassical dynamics. J. Chem. Phys., **64**:63, (1976).

[33] S. Sawada, R. Heather, B. Jackson, and H. Metiu. A strategy for time dependent quantum mechanical calculations using a gaussian wave packet representation of the wave function. J. Chem. Phys., **83**:3009, (1985).

[34] R. D. Coalson and M. Karplus. Multidimensional variational gaussian wave packet dynamics with application to photodissociation spectroscopy. J. Chem. Phys., **93**:3919, (1990).

[35] M. A. Rohrdanz and J. A. Cina. Probing intermolecular communication via lattice phonons with time-resolved coherent anti-stokes raman scattering. Molec. Phys., **104**:1161, (2006).

[36] C. T. Chapman and J. A. Cina. Semiclassical treatments for small-molecule dynamics in low-temperature crystals using fixed and adiabatic vibrational bases. J. Chem. Phys., **127**:114502, (2007).

[37] C. T. Chapman, X. Cheng, and J. A. Cina. Numerical tests of a fixed vibrational basis/gaussian bath theory for small molecule dynamics in low-temperature media. J. Phys. Chem. A, **115**:3980, (2011).

[38] J. Frenkel. *Wave Mechanics*. Clarendon, Oxford, 1934.

[39] A. D. McLachlan. A variational solution of the time-dependent schrodinger equation. Mol. Phys., **8**:, (1964).

[40] X. Cheng and J. A. Cina. Variational mixed quantum/semiclassical simulation of dihalogen guest and rare-gas solid host dynamics. J. Chem. Phys., **141**: 034113, (2014).

[41] G. Herzberg. *Spectra of Diatomic Molecules*. D. Van Nostrand Company, Inc., Princeton, 1950.

[42] M. Buchholz, C.-M. Goletz, F. Grossmann, B. Schmidt, J. Heyda, and P. Jungwirth. Semiclassical hybrid approach to condensed phase molecular dynamics: Application to the I_2Kr_{17} cluster. J. Phys. Chem. A, **116**:11199, (2012).

[43] P. A. Frantsuzov and V. A. Mandelshtam. Quantum statistical mechanics with gaussians: Equilibrium properties of van der waals clusters. J. Chem. Phys., **121**:9247, (2004).

[44] D. Frenkel and B. Smit. *Understanding Molecular Simulation*. Academic Press, San Diego, 1996.

[45] W. H. Press, B. P. Flannery, S. A. Teukolsky, and W. T. Vetterling. *Numerical Recipes*. Cambridge University Press, Cambridge, 1986.

[46] S. Y. Lee and E. J. Heller. Exact time-dependent wave packet propagation: Application to the photodissociation of methyl iodide. J. Chem. Phys., **76**: 3035, (1982).

[47] M. Liebel, C. Schnedermann, T. Wende, and P. Kukura. Principles and applications of broadband impulsive vibrational spectroscopy. J. Phys. Chem. A, **119**:9506, (2015).

[48] J. Brazard, L. A. Bizimana, T. Gellen, W. P. Carbery, and D. B. Turner. Experimental detection of branching at a conical intersection in a highly fluorescent molecule. J. Phys. Chem. Lett., **7**:14, (2016).

[49] C. N. Lincoln, J. Hayden, A. Galestian Pour, V. Perlfk, F. Sanda, and J. Hauer. A quantitative study of coherent vibrational dynamics probed by heterodyned transient grating spectroscopy. Vib. Spectrosc., **85**:167, (2016).

[50] T. J. Smith, L. W. Ungar, and J. A. Cina. Resonant short-pulse effects on nuclear motion in the electronic ground state. J. Lumin., **58**:66, (1994).

[51] M. Braun, C. Sobotta, R. Dürr, H. Pulvermacher, and S. Malkmus. Analysis of wave packet motion in frequency and time domain: Oxazine 1. J. Phys. Chem. A, **110**:9793, (2006).

[52] A. S. Johnson, J. Yuen-Zhou, A. Aspuru-Guzik, and J. J. Krich. Practical witness for electronic coherences. J. Chem. Phys., **141**:244109, (2014).

[53] C. J. Bardeen, Q. Wang, and C. V. Shank. Selective excitation of vibrational wave packet motion using chirped pulses. Phys. Rev. Lett., **75**:3410, (1995).

[54] L. E. Fried and S. Mukamel. Simulation of nonlinear electronic spectroscopy in the condensed phase. Adv. Chem. Phys., **84**:435, (1993). see Fig. 11 therein.

[55] Y. Tanimura and S. Mukamel. Femtosecond pump-probe spectroscopy of intermolecular vibrations in molecular dimers. J. Chem. Phys., **103**:1981, (1995).

[56] L. D. Landau and E. M. Lifshitz. *The Classical Theory of Fields*. Pergamon Press, Oxford, U.K., 1975. section 67.

[57] R. Zadoyan and V.A. Apkarian. Imaging the molecular rovibrational coherence through time-gated, frequency-resolved coherent anti-Stokes Raman scattering. Chem. Phys. Lett., **326**:1, (2000).

[58] Y.-C. Shen and J. A. Cina. What can short-pulse pump-probe spectroscopy tell us about Franck-Condon dynamics? J. Chem. Phys., **110**:9793, (1999). This work investigates the next level of approximation, in which pulse propagators are described using the semiclassical Franck-Condon approximation.

[59] I. V. Schweigert and S. Mukamel. Simulating multidimensional optical wave-mixing signals with finite-pulse envelopes. Phys. Rev. A, **77**:033802, (2008).

[60] D. J. Tannor. *Introduction to Quantum Mechanics: A Time-Dependent Perspective*. University Science Books, Sausalito, 2007.

[61] A. S. Petit and J. E. Subotnik. Appraisal of surface hopping as a tool for modeling condensed phase linear absorption spectra. J. Chem. Theory Comput., **11**:4328, (2015).

[62] J. A. Cina and P. A. Kovac. How fissors works: Observing vibrationally adiabatic conformational change through femtosecond stimulated raman spectroscopy. J. Phys. Chem. A, **117**:6084, (2013).

[63] L. W. Ungar and J. A. Cina. Short-time fluorescence Stokes shift dynamics. Adv. Chem. Phys., **100**:171, (1997).

[64] E. J. Heller. Quantum corrections to classical photodissociation models. J. Chem. Phys., **68**:2066, (1978).

[65] E. J. Heller. Photofragmentation of symmetric triatomic molecules: Time dependent picture. J. Chem. Phys., **68**:3891, (1978).

[66] C. Fang, R. R. Frontiera, R. Tran, and R. A. Mathies. Mapping GFP structure evolution during proton transfer with femtosecond raman spectroscopy. Nature, **462**:200, (2009).

[67] S. Mukamel and J. D. Biggs. Comment on the effective temporal and spectral resolution of impulsive stimulated Raman signals. J. Chem. Phys., **134**: 161101, (2011).

[68] M. H. Vos, F. Rappaport, J.-C. Lambry, J. Breton, and J.-L. Martin. Visualization of coherent nuclear motion in a membrane protein by femtosecond spectroscopy. Nature, **363**:320, (1993).

[69] A. T. N. Kumar, F. Rosca, A. Widom, and P. M. Champion. Investigations of amplitude and phase excitation profiles in femtosecond coherence spectroscopy. J. Chem. Phys., **114**:701, (2001).

[70] J. C. Dean, S. Rafiq, D. G. Oblinsky, E. Cassette, C. C. Jumper, and G. D. Scholes. Broadband transient absorption and two-dimensional electronic spectroscopy of methylene blue. J. Phys. Chem. A, **119**:9098, (2015).

[71] See supplementary material at http://dx.doi.org/10.1063/1.4947568 for a treatment of the fast-mode factor in the SE overlap in terms of vibrational eigenstates and eigenenergies.

[72] S. Mukamel. *Principles of nonlinear optical spectroscopy*. Oxford University Press, New York, 1995. For an elegant derivation of a related expression for the dispersed probe absorption signal in the limit of infinite spectral resolution from that for the frequency-integrated pump-probe signal, see Eqs. (4.89)-(4.92). The derivation presented in the present work is more closely akin to one "obtained by solving the Maxwell equations using the polarization $P^{(3)}$ as a source," but considers the perturbative response of an individual chromophore to the external laser fields, rather than a local, macroscopic polarization *per se*.

[73] M. Cho. *Two-dimensional optical spectroscopy.* CRC Press, Boca Raton, 2009.

[74] P. Hamm and M. Zanni. *Concepts and methods of 2D infrared spectroscopy.* Cambridge University Press, New York, 2011.

[75] U. Megerle, I. Pugliesi, C. Schriever, C.F. Sailer, and E. Riedle. Sub-50 fs broadband absorption spectroscopy with tunable excitation: putting the analysis of ultrafast molecular dynamics on solid ground. Appl. Phys. B, **96**: 215, (2009).

[76] J. Du, T. Teramoto, K. Nakata, E. Tokunaga, and T. Kobayashi. Real-time vibrational dynamics in chlorophyll *a* studied with a few-cycle pulse laser. Biophys. J., **101**:995, (2011).

[77] E. A. Carson, W. M. Diffey, K. R. Shelly, S. Lampa-Pastirk, K. L. Dillman, J. M. Schleicher, and W. F. Beck. Dynamic-absorption spectral contours: Vibrational phase-dependent resolution of low-frequency coherent wave-packet motion of IR144 on the ground-state and excited-state $\pi \rightarrow \pi^*$ surfaces. J. Phys. Chem. A, **108**:1489, (2004).

[78] M. Son, K. H. Park, M.-C. Yoon, P. Kim, and D. Kim. Excited-state vibrational coherence in perylene bisimide probed by femtosecond broadband pump-probe spectroscopy. J. Phys. Chem. A, **119**:6275, (2015).

[79] S. Ruetzel, M. Diekmann, P. Nuernberger, C. Walter, B. Engels, and T. Brixner. Photoisomerization among ring-open merocyanines. I. reaction dynamics and wave-packet oscillations induced by tunable femtosecond pulses. J. Chem. Phys., **140**:224310, (2014).

[80] D. Madsen, J. Stenger, J. Dreyer, E. T. J. Nibbering, P. Hamm, and T. Elsaesser. Coherent vibrational ground-state dynamics of an intramolecular hydrogen bond. Chem. Phys. Lett., **341**:56, (2001).

[81] T. J. Smith and J. A. Cina. Toward preresonant impulsive Raman preparation of large amplitude vibrational motion. J. Chem. Phys., **104**:1272, (1996).

[82] J. D. Biggs and J. A. Cina. Studies of impulsive vibrational influence on ultrafast electronic excitation transfer. J. Phys. Chem. A, **116**:1683, (2012).

[83] A. G. Dijkstra, C. Wang, J. Cao, and G. R. Fleming. Coherent exciton dynamics in the presence of underdamped vibrations. J. Phys. Chem. Lett., **6**:627, (2015).

[84] C. Y. Wong, B. D. Folie, B. L. Cotts, and N. S. Ginsberg. Discerning variable extents of interdomain orientational and structural heterogeneity in solution-cast polycrystalline organic semiconducting thin films. J. Phys. Chem. Lett., **6**:3155, (2015).

[85] A. S. Rury, S. Sorenson, E. Driscoll, and J. M. Dawlaty. Electronic state-resolved electron-phonon coupling in an organic charge transfer material from broadband quantum beat spectroscopy. J. Phys. Chem. Lett., **6**:3560, (2015).

[86] P. C. Arpin, D. B. Turner, S. D. McClure, C. C. Jumper, T. Mirkovic, J. R. Challa, J. Lee, C. Y. Teng, B. R. Green, K. E. Wilk, P. M. G. Curmi, K. Hoef-Emden, D. W. McCamant, and G. D. Scholes. Spectroscopic studies of cryptophyte light harvesting proteins: Vibrations and coherent oscillations. J. Phys. Chem. B, **119**:10025, (2015).

[87] S. Popescu, A. J. Short, and A. Winter. Entanglement and the foundations of statistical mechanics. Nat. Phys., **2**:754, (2006).

[88] P. Kukura, D. W. McCamant, and R. A. Mathies. Femtosecond Stimulated Raman Spectroscopy. Annu. Rev. Phys. Chem., **58**:461, (2007).

[89] S. Yoon, P. Kukura, C. M. Stuart, and R. A. Mathies. Direct observation of the ultrafast intersystem crossing in tris(2,2′-bipyridine)ruthenium(ii) using femtosecond stimulated Raman spectroscopy. Mol. Phys., **104**:1275, (2006).

[90] P. Kukura, R. Frontiera, and Mathies. Direct observation of anharmonic coupling in the time domain with femtosecond stimulated Raman scattering. Phys. Rev. Lett., **96**:2383031, (2006).

[91] P. Kukura, D. W. McCamant, S. Yoon, D. B. Wandschneider, and R. A. Mathies. Structural observation of the primary isomerization in vision with femtosecond-stimulated Raman. Science, **310**:1006, (2005).

[92] A. Weigel and N. P. Ernsting. Excited stilbene: Intramolecular vibrational redistribution and solvation studied by femtosecond stimulated Raman spectroscopy. J. Phys. Chem. B, **114**:7879, (2010).

[93] H. Kuramochi, S. Takeuchi, and T. Tahara. Ultrafast structural evolution of photoactive yellow protein chromophore revealed by ultraviolet resonance femtosecond stimulated Raman spectroscopy. J. Phys. Chem. Lett., **3**:2025, (2012).

[94] D. P. Hoffman and R. A. Mathies. Photoexcited structural dynamics of an azobenzene analog 4-nitro-4′-dimethylamino-azobenzene from femtosecond stimulated Raman. Phys. Chem. Chem. Phys., **14**:6298, (2012).

[95] J. M. Rhinehart, J. R. Challa, and D. W. McCamant. Multimode charge-transfer dynamics of 4-(dimethylamino)benzonitrile probed with ultraviolet femtosecond stimulated Raman spectroscopy. J. Phys. Chem. B, **116**:10522, (2012).

[96] W. Liu, F. Han, C. Smith, and C. Fang. Ultrafast conformational dynamics of pyranine during excited state proton transfer in aqueous solution revealed by femtosecond stimulated Raman spectroscopy. J. Phys. Chem. B, **116**:10535, (2012).

[97] W. Yu, J. Zhou, and A. E. Bragg. Exciton conformational dynamics of poly(3-hexylthiophene) (p3ht) in solution from time-resolved resonant-Raman spectroscopy. J. Phys. Chem. Lett., **3**:1321, (2012).

[98] R. Nakamura, N. Hamada, K. Abe, and M. Yoshizawa. Ultrafast hydrogen-bonding dynamics in the electronic excited state of photoactive yellow protein revealed by femtosecond stimulated Raman spectroscopy. J. Phys. Chem. B, **116**:14768, (2012).

[99] S.-Y. Lee, D. Zhang, D. W. McCamant, P. Kukura, and R. A. Mathies. Theory of femtosecond stimulated Raman spectroscopy. J. Chem. Phys., **121**:3632, (2004).

[100] Y. R. Shen and N. Bloembergen. Theory of stimulated Brillouin and Raman scattering. Phys. Rev., **137**:1787, (1965).

[101] Z. Sun, J. Lu, D. H. Zhang, and S.-Y. Lee. Quantum theory of (femtosecond) time-resolved stimulated Raman scattering. J. Chem. Phys., **128**:1441141, (2008).

[102] R. D. Mehlenbacher, B. Lyons, K. C. Wilson, Y. Du, and D. W. McCamant. Theoretical analysis of anharmonic coupling and cascading Raman signals observed with femtosecond stimulated Raman spectroscopy. J. Chem. Phys., **131**:2445121, (2009).

[103] B. Zhao, Z. Sun, and S.-Y. Lee. Quantum theory of time-resolved femtosecond stimulated Raman spectroscopy: Direct versus cascade processes and application to $CDCl_3$. J. Chem. Phys., **134**:0243071, (2011).

[104] Mukamel S. and J. D. Biggs. Comment on the effective temporal and spectral resolution of impulsive stimulated Raman signals. J. Chem. Phys., **134**: 1611011, (2011).

[105] K. Niu, S. Cong, and S.-Y. Lee. Femtosecond stimulated Raman scattering for polyatomics with harmonic potentials: Application to rhodamine 6G. J. Chem. Phys., **131**:0543111, (2009).

[106] A. Mandal and K. L. C. Hunt. Adiabatic and nonadiabatic contributions to the energy of a system subject to a time-dependent perturbation: Complete separation and physical interpretation. J. Chem. Phys., **137**:1641091, (2012).

[107] R. J. LeRoy. Molecular constants and internuclear potential of ground-state molecular iodine. J. Chem. Phys., **52**:2683, (1970).

[108] R. F. Barrow and K. K. Yee. $B^3\pi_{0_u^+}$–$X^1\sigma_g^+$ system of I_2: Rotational analysis and long-range potential in the $b^3\pi_{0_u^+}$ state. J. Chem. Soc., Faraday Trans., **69**:684, (1973).